Temperature effects on material properties and structural response of polymer matrix composites

PAR

Wei SUN

EPFL

ÉCOLE POLYTECHNIQUE
FÉDÉRALE DE LAUSANNE

Suisse
2015

To Hui and Audrey

Preface

Polymer matrix composite materials are increasingly used in civil infrastructure, such as bridge and building construction, by virtue of their advantageous mechanical properties. One drawback of these materials that needs to be dealt with at the structural design stage, however, is the sensitivity of the matrix to elevated temperatures, i.e. temperatures in the glass transition range of around 100°C. At this point, the matrix starts losing its stiffness and can thus no longer provide lateral support to fibers that are under compression. This may lead to instability phenomena such as fiber microbuckling or kinking.

To enable these effects to be addressed at the design level, the material and structural behaviors at elevated temperatures need to be understood and characterized. In this context, the PhD thesis of Wei Sun focuses on some significant aspects on the material and structural levels in cases of components subjected to compression loading.

Prof. Dr. Thomas Keller
EPFL-CCLab

Résumé

Les éléments structurels utilisés dans le génie civil sont souvent sollicités en compression. La résistance à la compression des matériaux composites à base de polymères renforcés par des fibres (FRP) est dominée par la résine, contrairement à leur résistance à la traction, et présente des valeurs plus faibles et plus de dispersion due aux défauts dans la résine et les fibres suite au processus de fabrication. La rupture en compression des matériaux en FRP, résultant de la synergie de mécanismes de rupture tels que le microflambage des fibres (kinking) et le flambage de l'élément, est plus complexe que celle en traction. De plus, les propriétés des matériaux composites constituant les éléments structurels comprimés sont sensibles aux augmentations de température pouvant se produire dans les applications d'ingénierie. Cette thèse comprend une étude expérimentale et analytique permettant d'approfondir les connaissances et d'améliorer la compréhension de l'effet de la température sur les propriétés des polymères et des matériaux en FRP ainsi que de la réponse structurelle de ces derniers sous une charge thermomécanique en compression.

Le premier chapitre de la thèse, l'introduction, résume l'état des connaissances, tandis que le deuxième chapitre présente un nouveau modèle physique pour la simulation de la partie imaginaire de la courbe du module du cisaillement en fonction de la température (G''-T) des matériaux thermodurcissables. Le modèle est basé sur la modification de l'équation G''-T utilisée pour les polymères thermoplastiques par l'introduction de deux nouvelles formulations concernant le calcul de la probabilité de la configuration et de la matrice de vitesse des matières thermodurcissables examinées. En outre, une fonction arctangente est proposée pour considérer l'effet de la température sur le carré moyen de séparation des extrémités des sous-molécules. Le modèle présenté a une base physique et peut être utilisé pour étudier l'effet de la structure moléculaire des résines thermodurcissables sur leur module G'' et leur température de transition vitreuse (T_g).

Dans le troisième chapitre, l'influence du déphasage thermique sur la T_g des polymères est analysée à l'aide des mesures effectuées sous différentes vitesses de réchauffement par analyse mécanique dynamique (DMA). Les résultats du déphasage thermique ont été quantifiés expérimentalement et simulés par un modèle de volumes finis. Une procédure numérique a été adoptée pour calculer l'influence des déphasages thermiques sur la courbe température-module de conservation. Lorsque les effets du déphasage thermique sont négligés, le module de conservation et la T_g d'un échantillon diminuent avec l'augmentation de la vitesse de réchauffement.

Le quatrième chapitre est consacré à l'étude des mécanismes de rupture de kinking d'échantillons prismatiques non-élancés de FRP à base de résine époxyde sollicités en compression axiale. La corrélation d'images numériques est utilisée pour cartographier les champs de déformation de surface et identifier les modes de rupture. Le mécanisme d'initiation de kink et la formation de bandes peuvent être clairement observés.

Dans le cinquième chapitre est étudié le comportement d'échantillons prismatiques non-élancés de FRP-époxyde sous températures élevées. Différentes longueurs et fractions volumiques de fibres ont

été testées. Trois modes de rupture différents sont observés et attribués à différentes plages de température et aux états de la matière correspondants. Différents mécanismes d'initiation et de formation de bandes de kink sont observés à la transition vitreuse et à l'état caoutchouteux du matériau examiné, cependant, l'élancement et la fraction volumique de fibres n'ont pas montré d'influence sur les dits mécanismes.

Abstract

Structural components used in civil engineering applications are often subjected to compressive loads. Unlike the tensile strength of fiber-reinforced polymer (FRP) materials, their compressive strength is resin-dominated, exhibiting lower values and more scatter due to initial imperfections in the resin and fibers caused during fabrication. The failure of FRP materials under compression resulting from the synergistic effect of failure mechanisms such as kinking and buckling is more complicated than that under tension. Furthermore, the material properties of composite structural components under compression are sensitive to temperature elevations occurring in engineering applications. This thesis includes experimental and analytical investigations in order to deepen the knowledge and enhance the understanding of the effect of temperature on the polymer and FRP material properties and the structural response of FRP composites in thermomechanical compression loading conditions.

An introduction including a literature review on the topic is presented in chapter 1, while in the second chapter of the thesis a new physically-based model for the simulation of the imaginary part of the shear modulus-temperature (G''-T) curve of thermosets is introduced. The model is based on the modification of the G''-T equation used for thermoplastic polymers through the introduction of two new formulations regarding the calculation of the configuration probability and the velocity matrix of the examined thermosets. In addition, an arctangent function is proposed to consider the effect of temperature on the mean square separation of the ends of the sub-molecules. The introduced model is based on a sound physical background, and can be used for the investigation of the effect of the molecular structure of thermosets on their G'' modulus and their glass transition temperature (T_g).

In the third chapter the influence of thermal lag on the T_g of polymers as measured under different heating rates during dynamic mechanical analysis (DMA) is investigated. The observed thermal lag results were experimentally quantified and numerically simulated by a developed finite volume model. A numerical procedure was adopted to calculate the influence of the thermal lags on the storage modulus-temperature curve. It was found that when the thermal lag effects are excluded, the storage modulus of a specimen and T_g decreases with increasing heating rates.

The fourth chapter focuses on the investigation of the kinking failure mechanisms of non-slender glass fiber-reinforced epoxy prismatic specimens subjected to axial compression loadings. Digital image correlation is used to map the surface strain fields in order to identify the failure modes. The kink initiation mechanism and the kink band formation can be clearly observed.

In the fifth chapter the kink behavior of non-slender glass fiber-reinforced epoxy prismatic specimens of variable length and fiber volume fraction at elevated temperatures is investigated. Three different failure modes are observed and attributed to different temperature ranges and the corresponding material states. Different kink initiation and the kink band formation mechanisms are observed at the glass transition and the rubbery states of the examined material, however, the different specimen slenderness and fiber volume fractions does not influence these mechanisms.

Keywords : FRP, compression, cross-linking, thermal lag, heating rate, kinking intiation, kink band formation, temperature, failure mechanism.

Table of contents

1 Introduction

1.1 Motivation

Structural components used in civil engineering applications, such as bridges and buildings, are often subjected to compressive loads. Characteristic examples of fiber-reinforced polymer (FRP) engineering applications are presented in Fig. 1.1 and 1.2 [1-2]. The bridge [1] located above the Avançon river in Bex Switzerland is comprised of a sandwich deck with two 22-mm-thick glass fiber reinforced-polymer (GFRP) face sheets and a 241-mm-thick balsa wood core adhesively bonded to steel girders. The top GFRP face sheet was designed to resist the compressive stress under real traffic conditions. The load-bearing structure of the 15-m-tall Eyecatcher Building, located in Basel Switzerland, shown in Fig. 1.2, consists of three parallel trapezoidal frames and the GFRP pultruded profiles in these frames are bolted on site after pre-assembly in the workshop. I-elements have been inserted along the height direction of the GFRP columns in the load-bearing structure to prevent buckling under compression.

Unlike the tensile strength of FRP materials, their compressive strength is resin-dominated, exhibiting lower values and more scatter due to initial imperfections in the resin and fibers caused during fabrication. The failure of FRP materials under compression resulting from the synergistic effect of failure mechanisms such as splitting, kinking, buckling and fiber failure is more complicated than that under tension. Furthermore, the material properties of composite structural components under compression are sensitive to temperature elevations occurring in engineering applications, as for example below the asphalt layer of FRP composite bridge decks during summer time [3], or when incidents such as fire occur [4]. Temperatures in such cases can exceed the glass transition or rubbery state temperatures of the resin, above which the material properties, such as the storage modulus, usually change considerably as shown in Fig. 1.3. The softening of the resin significantly weakens its fiber buckling resistance, resulting in reduction of the compressive strength and a change in the failure modes of the FRP materials during temperature elevation, e.g. a shift from splitting to kinking

failure [5-8] and from buckling to kinking [9] at elevated temperatures.
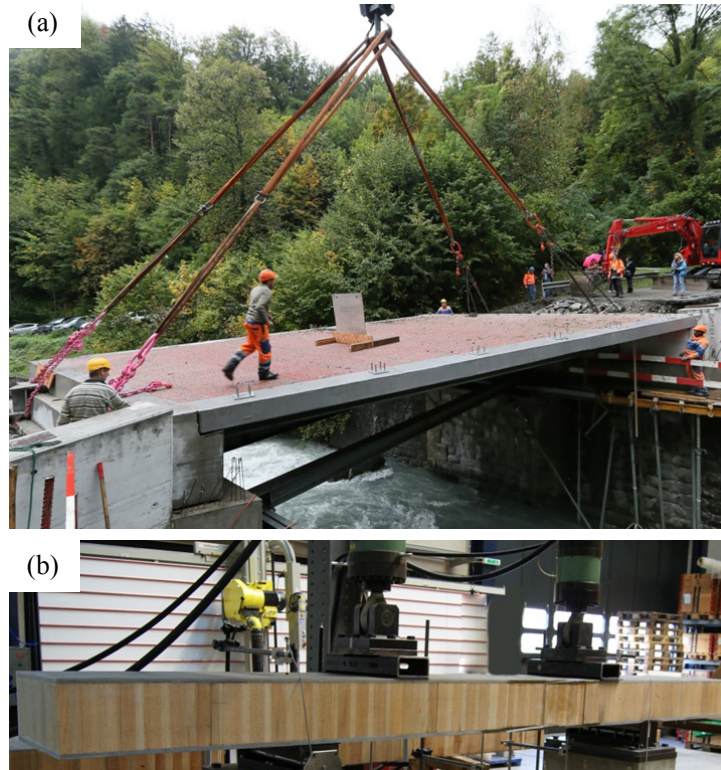
Fig. 1.1: *(a) Avançon Bridge in Bex, Switzerland, 2012 (b) Sandwich deck in four-point bending experiments*
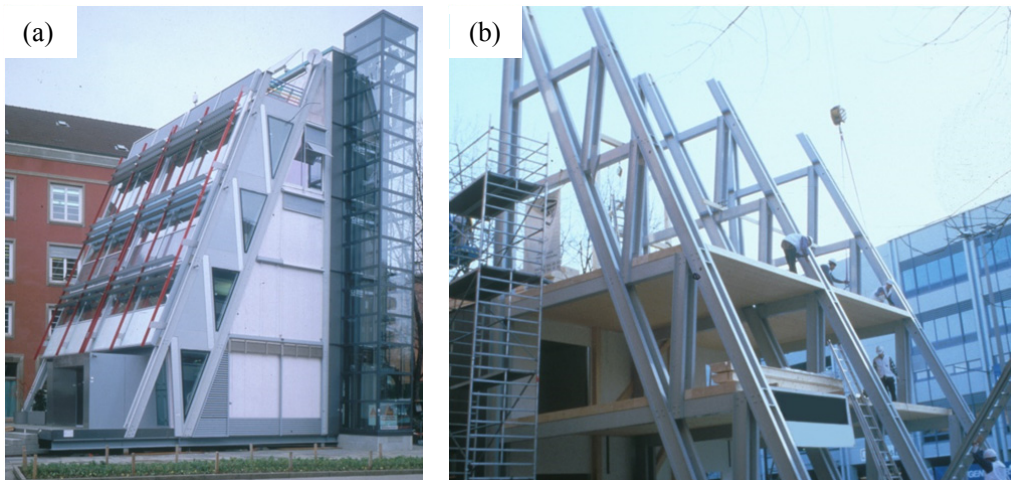
Fig. 1.2: *(a) GFRP Eyecatcher Building Basel, Switzerland, 1998 (b) Load-bearing structure of Eyecatcher Building*
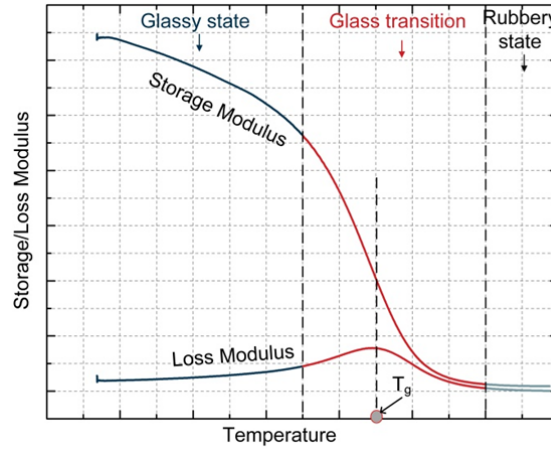
Fig. 1.3: *Different stages of the resin during temperature elevation*

Different methods, including the thermodynamic method, the free volume theory and the imaginary part of the *G*-modulus-temperature (G''-*T*) method, have been proposed to estimate the T_g of polymers. G'' is the ratio of the shear stress 90° out of phase with the strain to the strain during periodic experiments [10]. The thermodynamic method assumed that the T_g of dilute polymer solutions or thermoplastics is the temperature at which the molecular entropy decreases to zero [11-12]. The entropy is a function of the Boltzmann constant, the temperature and the total number of configuration states of the molecular chains. This method was then extended for the estimation of the T_g of lightly cross-linked rubbers [13], while the accuracy of this method is not satisfactory for thermosets since the high cross-linking density and entanglements between different polymer chains in the structure of thermosets do not allow the derivation of the configuration partition function of such materials.

The free volume theory introduced by Fox and Flory [14] assumes that the volume of a material can be divided into the molecular volume and the free volume, and a significant increase of the free volume of thermoplastics occurrs at temperatures around their T_g [15-16]. However, few theoretical models based on the free volume theory, except some semi-empirical equations, have been proposed to estimate the T_g of thermosets and it has been suggested that this theory has its limits due to its lack of physical reality [17]. Another method, based on the relationship between the imaginary part of the *G*-modulus, G'', and the temperature *T*, was proposed for thermoplastics with few interactions between their polymer chains [18-20]. The G'' in the G''-*T* equation suggested by Rouse [18] is a function of the viscosity that can be estimated by the entropy of the material and the mobility of the

3

molecular chains. The equation for the calculation of entropy was extended to lightly cross-linked thermosets (rubbers) by Mooney [20]. However, the accuracy of the G''-T equation is not satisfactory for thermosets since the method as proposed in [20] does not take into account the effect of the cross-linking and entanglements.

Experimental evidence has shown that heating or cooling rates influence the material properties and their variation during glass transition and thus the estimated T_g of the samples. The results obtained from measurements by instruments such as the dynamic mechanical analysis (DMA) machine that are commonly used for the estimation of the T_g of composites are reliable at heating rates lower than 1˚C/min, but can provide erroneous storage modulus and glass transition temperature values at higher heating rates, since in such conditions the thermal gradient inside the chamber of the DMA machine is ignored. Nevertheless, thermal lags between the specimen and the machine chamber as well as along the length of the specimen have been observed and recorded [21-24]. These thermal lags contradict the two assumptions adopted by the DMA in order to derive the storage modulus-temperature curves, i.e. i) the temperature measured by the DMA thermocouple is the same as the specimen temperature, and ii) the rate of decrease of the storage modulus with temperature is the same along the specimen length. The experimentally derived T_g at different heating rates thus has to be revised by excluding the effect of thermal lags.

Elevated temperatures also affect the mechanisms causing failure of FRPs under compressive loading. Although other failure mechanisms such as fiber failure, splitting, and buckling have been sufficiently investigated, adequate experimental evidence for the appropriate description of kinking initiation and kinking development is still lacking. Experimental studies of the kinking failure in fiber-reinforced composites date back to 1964 when the microbuckling of fibers was observed by Rosen during the shrinkage of the resin as the GFRP specimen was cooled from its curing temperature to room temperature [25]. Kinking under compression was therefore associated with microbuckling since shrinkage is followed by an increase of the compressive stress in the resin. Later studies reported the coexistence of microbuckling and kinking in CFRP laminates and assumed that kinking was a result of the microbuckling [26-28]. Kinking resulting from the compression fatigue loading of notched specimens was also attributed to microbuckling induced by crack propagation near the notch tip [29], however no experimental proof was reported to validate this assumption. Compressive experiments on CFRP specimens [30-32] focused on the kinking band propagation and broadening without providing any information to identify the factors leading to kinking. However, the validity of the causality between microbuckling and kinking was doubted by some researchers since they did not observe any significant microbuckling before or after the kinking failure of the examined specimens [33-34].

1.2 Objectives

The aim of this research is to investigate the temperature effects on the material properties and the structural response of polymer matrix composites. To achieve this goal, the research focuses on the following objectives:

1. The investigation of the $G''\text{-}T$ relationship and the glass transition temperature of thermosets.
2. The investigation of the thermal lag effect on the glass transition temperature of thermosets.
3. The investigation of the kinking failure mechanisms of GFRP specimens under compression at low temperatures.
4. The investigation of the effect of temperature on the kinking failure mode of non-slender glass fiber-reinforced polymers.

1.3 Methodology

The following methods are applied to achieve the objectives:

For objective 1,

1) Theoretical analysis of the mobility of the representative points on the molecular chain based on the proposed simplified cross-linking model.
2) Experimental measurement of the viscosity-temperature curve by low-frequency dynamic mechanical analysis.

For objective 2,

1) Experimental measurement of the thermal gradients at different heating rates during dynamic mechanical analysis.
2) Thermal environment simulation of the DMA chamber by a finite volume model.
3) Numerical analysis for the estimation of the effect of thermal lag on the storage modulus and T_g at different heating rates.

For objectives 3 and 4,

1) Optical microscopy scanning to obtain the microstructure of the GFRP specimen.
2) Compression experiments on specimens of different lengths and fiber volumes at tempera-

tures between 25 and 125°C.

3) Analysis of the strain field and lateral displacement data from digital image correlation system.

1.4 Thesis organization

The thesis is composed of four research papers that have been published or submitted for publication. The structure of the thesis is shown in Fig. 1.4.

In Chapter 2, a physically-based $G''\text{-}T$ relationship for thermosets is presented. A simplified cross-linking structure of the examined adhesive was proposed based on the chemical reaction between the resin and the hardener in Section 2.2. The mobility of the representative points on the proposed cross-linking structure was estimated and new formulations for the probability of configuration and the velocity matrix were obtained. From all these parameters, a physically-based $G''\text{-}T$ equation was derived. In Section 2.3, the $G''\text{-}T$ equation was calibrated by the viscosity-temperature curve and the assumed mean square separation of the ends of the sub-molecule-temperature relationship. The $G''\text{-}T$ curve of the examined adhesive obtained from the introduced $G''\text{-}T$ equation was then compared with the curve experimentally derived from DMA and the divergence between these two curves was discussed.

In Chapter 3, the effect of thermal lag on the glass transition temperature of polymers measured by DMA is studied. Experiments were performed to measure the temperature gradient during dynamic mechanical analysis at different heating rates. The specimen preparation from two materials, including an epoxy and a pultruded glass fiber-reinforced epoxy, and the experimental set-ups are introduced in Section 3.2. The thermal lags observed at different heating rates of the epoxy and the pultruded glass fiber-reinforced epoxy are presented in Section 3.2. In Section 3.3, a finite volume model is established to simulate the thermal environment inside the chamber of the dynamic mechanical analysis machine and the thermal lags measured on the specimens. The fact that the thermal radiation was shielded by the loading driveshaft of the three-point bending fixture was the origin of the thermal lag measured along the specimen length. In Section 3.4, the variation of the storage modulus of the examined epoxy specimen with temperature at different heating rates was evaluated based on a proposed equation. The storage modulus of the specimen without thermal lag and the T_g, defined as the average temperature between the onset of the glass transition temperature and the onset of the rubbery state of the examined adhesive, were found to decrease with heating rates.
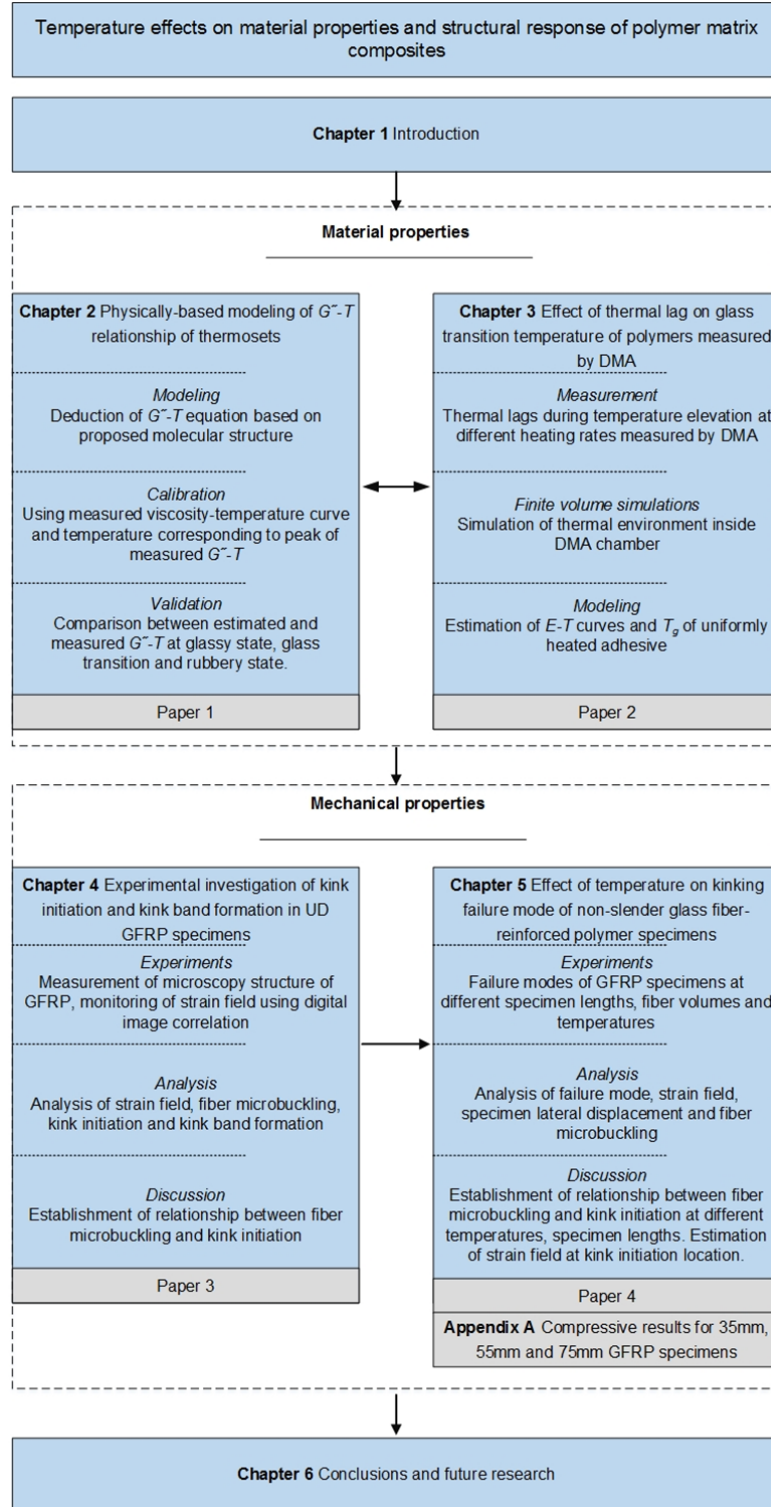
Fig. 1.4: *Thesis structure*

The kink initiation and kink band formation in unidirectional glass fiber-reinforced epoxy specimens under compression at different temperatures are investigated in Chapter 4. In Section 4.2, material properties, including the storage modulus-temperature relationship of the resin and the microstructure of the unidirectional glass fiber-reinforced epoxy specimens, were experimentally measured by DMA and optically scanned. The strain field and lateral displacement of the examined specimens at 25°C and 90°C measured by the digital image correlation system are presented in Section 4.3. In Section 4.4, the initiation of kinking failure due to the development of fiber microbuckling is explained and the kink band formation that comprised horizontal and inclined segments is visualized.

The effect of temperature on the kinking failure mode of non-slender glass fiber-reinforced polymers is shown in Chapter 5. In Section 5.2, specimens with two fiber volumes and three different lengths were prepared. The experimental results, including the load-axial displacement curves, compressive and shear strain fields at different temperatures, specimen lateral displacement and fiber microbuckling at temperatures up to 125°C, are introduced in Section 5.3. The relationship between kink initiation and fiber microbuckling at different temperatures, the compressive-shear strain interaction at the kink initiation location and kink band formation at elevated temperatures are discussed in Section 5.4.

Chapter 6 summarizes the experimental and analytical results of the thesis and proposes topics for future research.

1.5 List of publications

Paper 1: Sun, W., Vassilopoulos, A.P., and Keller T., Effect of thermal lag on glass transition temperature of polymers measured by DMA, International Journal of Adhesion and Adhesives, Volume 52, 2014, pp. 31-39.

Paper 2: Sun, W., Vassilopoulos, A.P., and Keller T., Physically based modeling of G''-T relationship of thermosets, submitted in March, 2015.

Paper 3: Sun, W., Vassilopoulos, A.P., and Keller T., Experimental investigation on kink initiation and kink band formation in unidirectional glass fiber-reinforced polymer specimens, Composite Structures, 2015, DOI:10.1016/j.compstruct.2015.04.028.

Paper 4: Sun, W., Vassilopoulos, A.P., and Keller T., Effect of temperature on kinking failure mode of non-slender glass fiber-reinforced polymer specimens, submitted in April, 2015.

References

1. Keller, T., Rothe, J., de Castro, J., and Osei-Antwi, M. (2014). GFRP-Balsa Sandwich Bridge Deck: Concept, Design, and Experimental Validation. Journal of Composites for Construction, Volume 18, 2014, pp. 04013043.

2. Keller, T., Towards structural forms for composite fibre materials, Structural Engineering International, Volume 9, 1999, pp. 297-300.

3. Harvey, A. O. J., Analysis of 30 years of pavement temperatures using the enhanced integrated climate model (EICM), Report for the California Department of transportation, 2004.

4. Feih, S. Mathys, Z., Gibson, A.G., and Mouritz, A.P., Modelling the tension and compression strengths of polymers laminates in fire, Composite Science and Technology, Volume 67, 2007, pp. 551-564.

5. Grape, J.A., and Gupta, V., The effect of temperature on the strength and failure mechanisms of a woven carbon/polyimide laminate under compression, Mechanics of Materials, Volume 30, 1998, pp. 165-180.

6. Bazhenov, S.L., and Kozey, V.V., Compression fracture of unidirectional carbon fibre-reinforced plastics, Journal of materials science, Volume 26, 1991, pp. 6764-6776.

7. Sun, W., Vassilopoulos, A.P., and Keller T., Experimental investigation on kink initiation and kink band formation in unidirectional glass fiber-reinforced polymer specimens, submitted to Composite Structures.

8. Sun, W., Vassilopoulos, A.P., and Keller T., Effect of temperature on kinking failure mode of non-slender glass fiber-reinforced polymer specimens, submitted to Composite Structures

9. Yu, B., and Keller, T., Delamination and kink-band failure of pultruded GFRP laminates under elevated temperatures and compression, Composite Structures, Volume 93, 2011, pp. 843-849.

10. Ferry, J.D., Viscoelastic properties of polymers, John Wiley & Sons, 1980.

11. Dimarzio, E.A., Gibbs, J.H., Chain stiffness and the lattice theory of polymer phase, The Journal of Chemical Physics, 1958; 28: 807-813.

12. Gibbs, J.H., Dimarzio, E.A., Nature of the glass transition and the glassy state, The Journal of Chemical Physics, 1958; 28: 373-383.

13. Dimarzio, E.A., On the second-order transition of a rubber, Journal of Research of the National Bureau of Standards-A. Physics and Chemistry, 1964; 68A: 611-617.

14. Fox, T.G.J., Flory, P.J., Second-order transition temperatures and related properties of polystyrene. I. Influence of molecular weight, Journal of Applied Physics, 1950; 21: 581-591.

15. Rogers, S.S., Mandelkern, L., Glass formation in polymers, I. The glass transition of the poly-(n-alkyl methacrylates), Glass Formation in Polymers, 1957; 61: 985-990.

16. Grest, G.S., Cohen, M.H., Liquid-glass transition: Dependence of the glass transition on

heating and cooling rates, Physical Review B, 1980; 21: 4113-4117.

17. Yonezawa, F., Glass transition and relaxation of disordered structures, Solid state physics, 1991; 45: 179-195.

18. Rouse, P.E., A theory of the linear viscoelastic properties of dilute solutions of coiling polymers, Journal of Chemical Physics, 1953; 21: 1272-1280.

19. Zimm, B.H., Dynamics of polymer molecules in dilute solution: viscoelasticity, flow birefringence and dielectric loss, Journal of Chemical Physics, 1956; 24: 269-278.

20. Mooney, M., A diffusion theory of the visco-elasticity of rubbery polymers in finite elastic strain, Journal of Polymer Science, 1959; XXXIV: 599-626.

21. Sućeska, M., Liu, Z.-Y. , Mušanić, S.M. , and Fiamengo, I., Numerical modelling of sample-furnace thermal lag in dynamic mechanical analyser, Journal of Thermal Analysis and Calorimetry, Volume 100, 2010, pp. 337-345.

22. Roura, P., and Farjas, J., Analysis of the sensitivity and sample-furnace thermal-lag of a different thermal analyzer, Thermochimica Acta, Volume 430, 2005, pp. 115-122.

23. Zhang, Y., Adams, R.D., and da Silva, L.F.M., A rapid method of measuring the glass transition temperature using a novel dynamic mechanical analysis method, The Journal of Adhesion, Volume 89, 2013, pp.785-806.

24. Sun, W., Vassilopoulos, A.P., and Keller T., Effect of thermal lag on glass transition temperature of polymers measured by DMA, International Journal of Adhesion and Adhesives, Volume 52, 2014, pp. 31-39.

25. Rosen, B.W., Mechanics of composite strengthening, Fiber composite materials, American society for metals, Ohio, 1964.

26. Evans, A.G., and Adler, W.F., Kinking as a mode of structural degradation in carbon fiber composites, Acta Metallurgica, Volume 26, 1978, pp. 725-738.

27. Lankford, J., Compressive failure of fiber-reinforced composites: buckling, kinking and the role of interphase, Journal of material science, Volume 30, 1995, pp. 4343-4348.

28. Dobb, M.G., Johnson, D.J., and Park, C.R., Compressional behavior of carbon fibres, Journal of materials science, Volume 25, 1990, pp. 829-834.

29. Berg, C.A., and Salama, M., Fatigue of graphite fiber-reinforced epoxy in compression, Fiber Science and Technology, Volume 6, 1973, pp. 79-118.

30. Moran, P.M., Liu X.H., and Shih, C.F., Kink band formation and band broadening in fiber compression under compressive loading, Acta Metallurgica et Materialia, Volume 43, 1995, pp.2943-2958.

31. Volger, T.J., and Kyriakides, S. On the initiation and growth of kink bands in fiber composites: Part I. experiments, International Journal of Solids and Structures, Volume 38, 2001,

pp. 2639-2651.

32. Gutkin, R., Pinho, S.T., Robinson, P. and Curtis, P.T., On the transition from shear-driven fibre compressive failure to fibre kinking in notched CFRP laminates under longitudinal compression, Composites Science and Technology, Volume 70, 2010, pp. 1223-1231.

33. Weaver, C.W., and Williams, J.G., Deformation of a carbon-epoxy composite under hydro-static pressure, Journal of material science, Volume 10, 1975, pp. 1323-1333.

34. Wronski, A.S., and Parry, T.V., Compressive failure and kinking in uniaxially aligned glass-resin composite under superposed hydrostatic pressure, Journal of material science, Volume 17, 1982, pp. 3656-3662

2 Physically-based modeling of G''-T relationship of thermosets

Reference Detail

Sun, W., Vassilopoulos, A.P., and Keller T., Physically based modeling of G''-T relationship of thermosets, submitted in March, 2015.

2.1 Introduction

The material properties of polymers, such as the storage modulus, decrease with the temperature rise caused by the increasing mobility of polymer chains induced by the absorbed thermal energy. This decrease is more pronounced when the temperature reaches the glass transition temperature (T_g). Several methods have been proposed for the estimation of the T_g of thermoplastic polymers.

Dimarizo and Gibbs [1] and Gibbs and Dimarizo [2] introduced the thermodynamic method and assumed that the T_g of polymers with simple molecular structures (dilute polymer solutions and thermoplastics) is the temperature at which the molecular entropy decreases to zero. The entropy is a derivation of the free energy of the system, and the latter is the product of the Boltzmann constant, the temperature and the configuration partition function. The configuration partition function is a function of the total number of configuration states of the molecular chains, which is counted by a permutation and combination method known as the Flory-Huggins counting process [1, 2]. A simplification of the Flory-Huggins counting process was proposed for counting the configuration of the polymer chains of dilute polymer solutions by Fowler and Rushbrooke [3] and Guggenhein [4]. However, the divergence between the calculated results and the experimental data was observed to increase with the increase of the percentage of the cross-linking parts. The method in [1, 2] was

extended for the estimation of the T_g of lightly cross-linked rubbers by modifying the Flory-Huggins counting process and introducing several rubber-characterized equations [5]. This method was not applied for the estimation of the T_g of thermosets since the high cross-linking density and entanglements between different polymer chains in the structure of thermosets do not allow the derivation of the configuration partition function of such materials.

The free volume theory introduced by Fox and Flory [6] assumes that the volume of a material can be divided into the molecular volume and the free volume, the volume around each molecule. The free volume theory was proposed for studying the liquid-glass transition of dilute polymer solutions and thermoplastics that are softened at temperatures around their glass transition temperature. The T_g of such polymers could be estimated by the free volume method due to the significant increase of their free volume at temperatures around their T_g [7-8]. The T_g in this case can be effectively estimated by measuring the thermal expansion coefficient of the material [6-8]. Few theoretical models based on the free volume theory have been proposed to estimate the T_g of polymers. A semi-empirical equation was proposed by Rogers and Mandelkern [7] to estimate the T_g of polymers with similar molecular structures. According to this equation, the difference between the T_g of two polymers with the same molecular structure is proportional to the volume difference of these two materials at the liquid state. If the T_g and the free volume in the liquid state of one reference polymer is known, the T_g of all polymers with the same molecular structure could be determined. In addition, the classification of polymers according to their molecular structure is not self-evident, leading to errors as shown in [7]. However, the application of the free volume theory in thermosets is still limited and it is suggested that there is a lack of physical reality of the free volume theory [9].

Another method, based on the relationship between the imaginary part of the G-modulus, G'', and the temperature T, was proposed in [10-13], again for thermoplastics. According to this method, the T_g of a thermoplastic polymer is defined as the temperature corresponding to the peak of G'' under dynamic loading. A G''-T equation was suggested by Rouse [10] to estimate the shear modulus of dilute polymer solutions exhibiting few interactions between their polymer chains. The G'' in this equation was a function of the viscosity that could be estimated by the entropy of the material, and the mobility of the molecular chains. It was pointed out by Rouse [10] that the disagreement between the G'' (G_2 in the paper) deduced from this equation and the experimental value was due to the length of the molecular chains of the actual polymers and the inter- and intra-molecular interface. The expression of a critical parameter in the deduction of the G''-T equation (entropy) was extended to lightly cross-linked thermosets (rubber) by Mooney [12] under the assumption that the strands of rubbers (molecules between the cross-linking points) are equivalent to the single molecule of thermoplastics. However, the accuracy of the G''-T equation for thermosets is not satisfactory since the method as

14

proposed in [12] does not take into account the effect of the cross-linking and entanglements on the expression of the equation parameters.

A modified *G″-T* equation is proposed in this work for the modeling of the loss modulus of thermosets during temperature elevation. The method introduces two new formulations regarding the calculation of the configuration probability and the velocity matrix. Appropriate formulations for the investigation of the influence of these three parameters on the loss modulus are developed, taking into account the cross-linking effects. The experimentally derived steady-flow viscosity vs. temperature relationship and an assumed sub-molecular mean square separation vs. temperature equation are necessary for the model calibration. The derived new *G″-T* equation is validated by modeling the behavior of a commercial structural epoxy adhesive (Sikadur-330, Sika AG).

2.2 *G″-T* model for thermosets

The development of the formulations describing the influence of the configuration probability and the velocity matrix is presented in this section.

2.2.1 Probability of configuration

A schematic representation of the molecular structure of thermosets is shown in Fig. 2.1. Each sub-molecule in a molecular structure is linked with two others in a certain geometrical configuration. The probability (P_i) that the end-to-end distances of the three sub-molecules (i-1~i, i~i+1 and i~$N/2$+i) located around the representative point, i, on the molecular chain are $d_{i-1,i}$, $d_{i,\,i+1}$ and $d_{i,\,N/2+i}$ respectively , see Fig. 2.2, is given by:
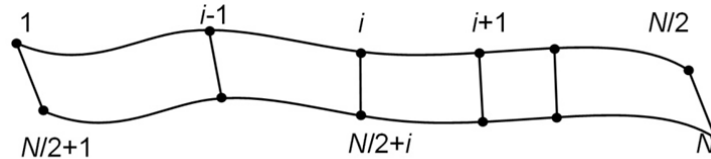
Fig. 2.1: *Molecular structure of thermosets*
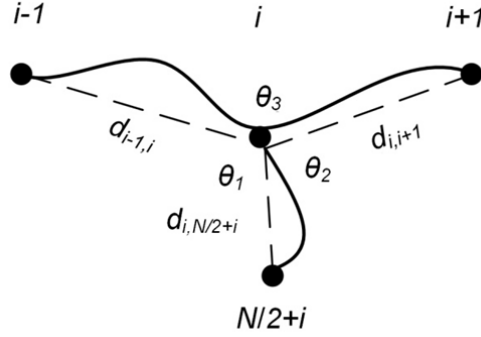
Fig. 2.2: *Molecular structure near representative point i*

$$P_i = P_{i-1,i} \cdot P_{i,i+1} \cdot P_{i,N/2+i}, \tag{2.1}$$

as a product of the individual probabilities $P_{i-1,i}$, $P_{i,i+1}$ and $P_{i,N/2+i}$ of the end-to-end distance of each sub-molecule having the value $d_{i-1,i}$, $d_{i,\,i+1}$ and $d_{i,\,N/2+i}$ respectively.

It is assumed that the sub-molecules (i-1~i, i~i+1, i~$N/2$+i) are Gaussian chains [10]. In addition, for simplification, all the angles between the end-to-end directions of adjunct polymer sub-molecules are equal to θ, see Fig. 2.3, the probability P that the end-to-end distance is d is [10]:

$$P = \left(\frac{b}{\pi}\right)^{3/2} \exp\left(-bd^2\right) \tag{2.2}$$

where b is equal to $3/(2\sigma^2)$ and σ^2 is the mean square distance (separation) of the ends of sub-molecules. [10]

After the movement of a representative point, i, from (0, 0, d) to (x, y, z), see Fig. 2.3, the end-to-end distance of each sub-molecule is given by:

$$\begin{aligned}
d^2_{i-1,i} &= x^2 + y^2 + z^2 \\
d^2_{i,i+1} &= x^2 + \left(y - d\sin\theta\right)^2 + \left(z - d - d\cos\theta\right)^2 \\
d^2_{i,N/2+i} &= x^2 + \left(y + d\sin\theta\right)^2 + \left(z - d - d\cos\theta\right)^2
\end{aligned} \tag{2.3}$$
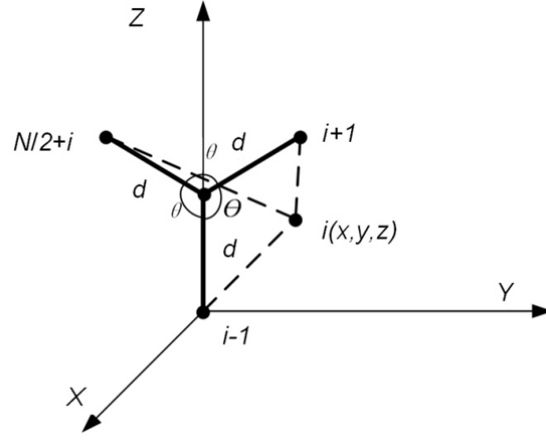
Fig. 2.3: *Coordinate system for molecular structure near representative point i*

The P_i of thermosets is obtained after discarding the first order expression of x, y and z,

$$P_i = P_{i-1,i} \cdot P_{i,i+1} \cdot P_{i,N/2+i} = (b/\pi)^{3/2 \times 3} \exp\left(-bd^2_{i-1,i}\right)\exp\left(-bd^2_{i,i+1}\right)\exp\left(-bd^2_{i,N/2+i}\right)$$
$$= (b/\pi)^{9/2} \exp\left(-b\left(3x^2 + 3y^2 + 3z^2\right)\right)$$

(2.4)

And therefore, the probability of configuration of a molecular structure, like the one shown in Fig. 2.1, can be calculated by:

$$P_N = \prod_{i=1}^{N} P_i\left(x_i, y_i, z_i\right) = (b/\pi)^{9N/2} \exp\left(-3b\sum_{i=1}^{N}\left(x_i^2 + y_i^2 + z_i^2\right)\right)$$

(2.5)

2.2.2 Velocity Matrix

The velocity vector of thermosets is also different from that of thermoplastics. The velocity of the representative point, *i*, is affected by the cross-linking and can be calculated if the velocity of the adjacent points is also considered.

The velocity of the representative point on the molecular chain of thermosets under dynamic loading is proportional to the applied driving force that can be estimated from the gradient of the free energy (the free energy is the product of the temperature (*T*) and the system entropy (*S*), -*TS*) along the cor-

responding coordinate direction [12]. The relative velocity of the representative point i with respect to the adjacent points is given by:

$$\left(\frac{\partial x_i}{\partial t}\right)_{i-1} = BT\left(\frac{\partial S}{\partial x_i} - \frac{\partial S}{\partial x_{i-1}}\right) \tag{2.6}$$

$$\left(\frac{\partial x_i}{\partial t}\right)_{i+1} = BT\left(\frac{\partial S}{\partial x_i} - \frac{\partial S}{\partial x_{i+1}}\right) \tag{2.7}$$

$$\left(\frac{\partial x_i}{\partial t}\right)_{i+N/2} = BT\left(\frac{\partial S}{\partial x_i} - \frac{\partial S}{\partial x_{i+N/2}}\right) \tag{2.8}$$

where x_i is the displacement of the ith representative point, t is the time, and B is a parameter representing the mobility of a sub-molecule.

The total velocity of the representative point i, is given as the sum of the relative velocities calculated above:

$$\left(\frac{\partial x_i}{\partial t}\right) = BT\left(-\frac{\partial S}{\partial x_{i-1}} + 3\frac{\partial S}{\partial x_i} - \frac{\partial S}{\partial x_{i+1}} - \frac{\partial S}{\partial x_{i+N/2}}\right) \tag{2.9}$$

The velocity matrix (V), showing the velocity of all representative points on the molecular chain, can then be estimated by Eq. (2.10) [10].

$$V = \begin{bmatrix} \dfrac{\partial x_1}{\partial t} \\ \dfrac{\partial x_2}{\partial t} \\ \vdots \\ \dfrac{\partial x_N}{\partial t} \end{bmatrix} = BTA_0 \begin{bmatrix} \dfrac{\partial S}{\partial x_1} \\ \dfrac{\partial S}{\partial x_2} \\ \vdots \\ \dfrac{\partial S}{\partial x_N} \end{bmatrix} \tag{2.10}$$

where A_0 is the coefficient matrix for thermosets, introduced in this work,

$$A_0 = \begin{bmatrix} 3 & -1 & 0 & \cdots & 0 & -1 & 0 & 0 & \cdots & 0 \\ & 3 & -1 & \cdots & 0 & 0 & -1 & 0 & \cdots & 0 \\ & & 3 & \cdots & 0 & 0 & 0 & -1 & \cdots & 0 \\ & & & \ddots & \vdots & \vdots & \vdots & \vdots & \ddots & \vdots \\ & & & & 3 & 0 & 0 & 0 & \cdots & -1 \\ & & & & & 3 & -1 & 0 & \cdots & 0 \\ & & & & & & 3 & -1 & \cdots & 0 \\ & \text{Symmetric} & & & & & & 3 & \cdots & 0 \\ & & & & & & & & \ddots & \vdots \\ & & & & & & & & & 3 \end{bmatrix}_{N \times N} \tag{2.11}$$

that is different from the coefficient matrix of thermoplastics, see [10]. The eigenvalues of matrix A_0 are:

$$\lambda_{1p} = 4\sin^2 \frac{p\pi}{2(N/2+1)} \qquad p = 1,2\ldots\ldots\frac{N}{2} \tag{2.12}$$

$$\lambda_{2p} = 2 + 4\sin^2 \frac{(p-N/2)\pi}{2(N/2+1)} \quad p = \frac{N}{2}+1, \frac{N}{2}+2\ldots\ldots N \tag{2.13}$$

2.2.3 Modified *G″-T* equation

Based on Eq. (2.5) and Eqs. (2.12-2.13) and the continuity equation, [10], the imaginary part of the *G*-modulus of thermosets is,

$$G^{"} = (\frac{\sqrt{3}}{2\sigma^2\pi})^{3N} \frac{nkT}{3} \sum_{p=1}^{N} \frac{\omega\tau_p}{1+\omega^2\tau_p^2} \tag{2.14}$$

$$\tau_p = \frac{72\eta_T}{nkT\lambda_{1p}\frac{N}{2}\left(\frac{N}{2}+3\right)} (\frac{2\sigma^2\pi}{\sqrt{3}})^{3N}, \quad p = 1,2\ldots\ldots\frac{N}{2} \tag{2.15}$$

$$\tau_p = \frac{72\eta_T}{nkT\lambda_{2p}\frac{N}{2}\left(\frac{N}{2}+3\right)} (\frac{2\sigma^2\pi}{\sqrt{3}})^{3N}, \quad p = \frac{N}{2}+1, \frac{N}{2}+2\ldots\ldots N \tag{2.16}$$

$$n = \frac{\rho_0}{M} N_A \tag{2.17}$$

where τ_p is the relaxation time of the molecule, ω is the loading frequency, k is the Boltzmann constant, n is the number of molecules per unit volume, η_T is the steady-flow viscosity at temperature T, ρ_0 is the density of the material, and M is the molecular weight that can be estimated by: $M=(N-2)\cdot M_{resin}+(N/2)\cdot M_{hardener}$, and N_A is the Avogadro constant.

The parameters in Eq. (2.14), except η_T and σ^2, can be estimated according to the cross-linked molecular structure of thermosets consisting of molecules of the resin and the hardener. The chemical formulations of the molecules of these ingredients and the corresponding reactions can be found in technical data documents. The steady-flow viscosity, η_T, should be obtained by low-frequency dynamic mechanical analysis. The parameter σ^2, the mean square separation of the ends of sub-molecules, varies with temperature due to the different end-to-end distances of the sub-molecules that change because the molecular mobility increases with temperature elevation. In previous works, e.g. [17], σ was assumed to be proportional to $N_0^{0.5}$, where N_0 is the number of half of the sub-molecules along the length direction of the molecular chain of thermosets. An arctangent function was introduced here to simulate the effect of temperature on the variation of σ, which was assumed to be significant during the glass transition and the rubbery state and negligible in the glassy state of the thermoset, see Eq. (2.18) and Fig. 2.4:

$$\sigma = q[N_0^{0.5} + \arctan(-(T-T_0))] \tag{2.18}$$

where q is a fitting parameter, T_0 is the reference temperature at the rubbery state, and N_0 is equal to $N/2$-1 according to the molecular structure shown in Fig. 2.1.
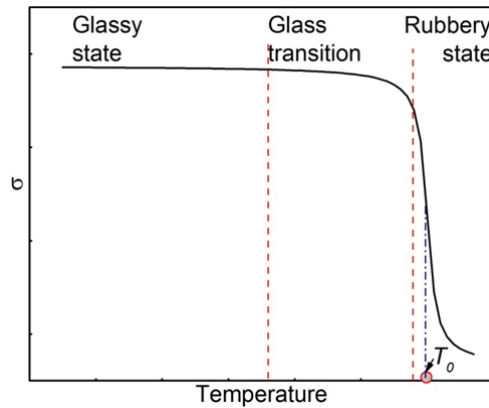

Fig. 2.4: *Assumed σ-T curve based on Eq. (2.18)*

2.3 Model parameter estimation and validation

2.3.1 Estimation of viscosity and q parameter

Sikadur-330 is a thixotropic bi-component commercial structural adhesive produced by Sika Schweiz AG. The base resin is a bisphenol-A-based epoxy and the main hardener is trimethylhexane-1,6-diamine, as shown in Table 1. This adhesive contains a small quantity of inert inorganic silica-based fillers (<20% by weight). The mixing ratio is 4:1 resin to hardener [14]. Specimens with dimensions 53mm×10mm×3mm were fabricated and used for the experimental investigation according to ASTM E1640-09 [16]. In order to exclude the effect of post-curing during the experiment, the epoxy specimens were cured at ambient temperature for 48 hours and then post-cured at 63˚C for 144 hours to approach a curing degree of 100% (according to [15]). The T_g of fully cured Sikadur-330 was measured by DMA experiments at 1Hz and 1 ˚C/min. The value corresponding to the loss modulus curve is equal to 64°C. The specimen configuration and the fixture of the Q800 are shown in Fig. 2.5.

The low-frequency dynamic experiment was performed using a Q800 DMA machine and a three-point bending fixture to estimate the viscosity η_T. The low-frequency dynamic experiment was performed using the multi-frequency model of the Q800 at a loading frequency of 0.02Hz. A reversed cyclic displacement with amplitude of 15μm was applied and the corresponding load was measured to calculate the loss modulus of the material. The specimen was heated up to 90°C at 0.2°C/min to minimize the thermal lag between the specimen and the surrounding environment inside the Q800 chamber.
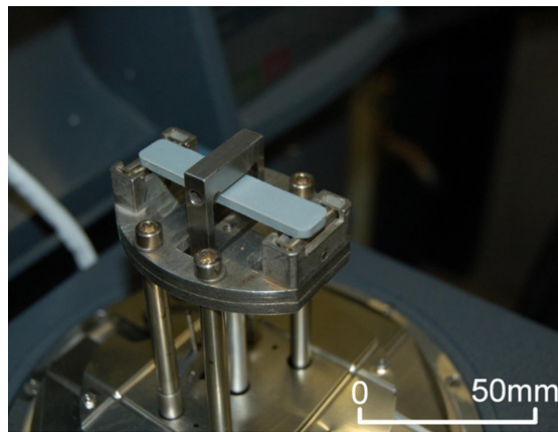

Fig. 2.5: *Specimens mounted on three-point-bending fixture of Q800*

The viscosity (η_T) deduced from the low-frequency dynamic experiment can be estimated by the experimentally obtained loss modulus (E'') of the specimen during DMA via the following equation:

$$\eta_T = \frac{E''}{2(1+\nu)\omega} \tag{2.19}$$

where ν=0.44 is the Poisson's ratio of the examined epoxy resin. The viscosity derived from the low frequency dynamic analysis as a function of temperature is shown by a solid line in Fig. 2.6. The viscosity initially increases with temperature, reaches a peak near the glass transition temperature and then decreases. The maximum estimated value of viscosity was 1250 MPa·s.

The molecular weight of the resin and the hardener can be calculated based on the chemical names of their components and the corresponding chemical structure. The concentration and the density were obtained from [14] and their values are shown in Table 2.1..An iterative process was used to estimate the value of the q parameter based on the above-mentioned determined parameters. According to this process, the appropriate q value (q=13.3%, see Fig. 2.7) is the one that results in a σ value (from Eq. 2.18) which, when substituted in Eq. (2.14), provides a G''-T curve with a maximum at a similar temperature to that of the curve experimentally derived by a DMA experiment at 1Hz and a rate of 1˚C/min, see the dashed line in Fig. 2.6.

Table 2.1: *Material parameters of Sikadur-330*

	Ingredients*	Concentration* (%)	Molecular weight (g/mol)**	Density ρ_0 (g/cm^3)*	N**
Part A (Resin)	Bisphenol A-(epichlorhydrin) epoxy resin	70	356		
	1,4-bis (2,3 epoxypropoxy) butane	20	202	289.6 (M_{resin})	
	Other solvent	10			1.3	10
Part B (Harde-ner)	Trimethylhexane-1,6-diamine	75	158	118.5 ($M_{hardener}$)	
	Other solvent	25			

*: Data from [14]

**: Calculated data
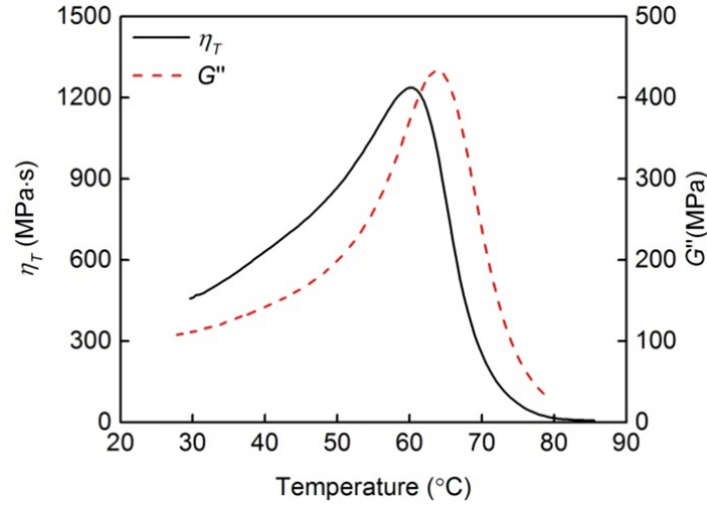
Fig. 2.6: *Steady-flow viscosity, η_T, of Sikadur-330 measured by DMA at 0.02Hz and G''-T curve measured by DMA at 1 Hz*
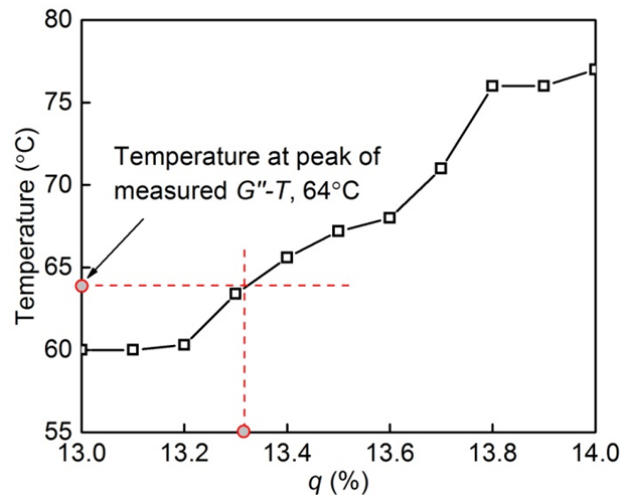
Fig. 2.7: *Estimation of q*

2.3.2 *G''-T* model validation

The comparison between the *G''-T* curve obtained by Eq. (2.14) and the experimentally derived one is shown in Fig. 2.8. The two curves coincide at the range of temperatures above T_g, while the modeled *G''* is higher than the experimental value for temperatures below T_g, reaching a maximum diffe-

rence of approximately 70% at 35°C in the glassy state of the examined thermoset. The cross-linked molecular chains of thermosets are further linked to each other by entanglements and strong secondary bonds especially at temperatures below T_g. The proposed molecular structure, shown in Fig. 2.1, and the assumed σ-T equation were incapable of accurately simulating the behavior of the material at this stage, leading to the observed diversion between the two curves. During temperature elevation, the secondary bonds break and the entanglements between polymer chains loosen, so that the cross-linking molecular structure can be well described by the G''-T model provided by Eq. (2.14).
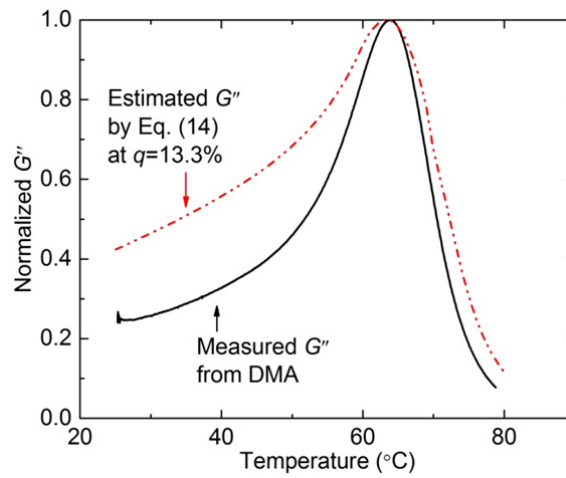
Fig. 2.8: *Comparison of G''-T curves derived by different methods*

2.4 Conclusions

In this work, the G''-T relationship for thermoplastics has been modified to provide a physically-based G''-T model for thermosets. All the necessary parameters for the model derivation, except one fitting parameter for the description of the mean square separation of the ends of the sub-molecules with temperature, were estimated based on the molecular structure of thermosets and low-frequency dynamic experiments. The fitting parameter was calibrated based on the experimentally derived G''-T curve of the examined thermoset. The following conclusions can be drawn:

- New physically-based formulations for the calculation of the configuration probability and the derivation of the velocity matrix of thermosets have been introduced. The formulations were derived based on the molecular structure of thermoset resins taking into account the cross-linking and entanglements that such materials present.

24

- An arctangent function between σ and T was found to be appropriate to consider the different effects of temperature on the end-to-end distances of the polymer chains at the glassy state, the glass transition and the rubbery state of the thermosets.
- The G''-T curve obtained from the introduced model corresponded well with the G''-T curve experimentally derived by a dynamic mechanical analysis, especially for temperatures above the glass transition. The divergence between the G''-T curve derived from the model and the experimentally derived one below T_g is attributed to the strong link between the polymer chains at the glassy state that cannot be precisely described by the model.

A more complex cross-linking model is necessary in order to accurately simulate the G''-T curve at the glassy state comprising additional parameters for the description of the entanglement variation and the effect of the secondary bonds on the mobility of the polymer chains for temperatures below the glass transition temperature.

References

1. Dimarzio, E.A., Gibbs, J.H., Chain stiffness and the lattice theory of polymer phase, The Journal of Chemical Physics, 1958; 28: 807-813.

2. Gibbs, J.H., Dimarzio, E.A., Nature of the glass transition and the glassy state, The Journal of Chemical Physics, 1958; 28: 373-383.

3. Fowler, R.H., Rushbrooke, G.S., An attempt to extend the statistical theory of perfect solutions, Transactions of the Faraday Society, 1937; 33: 1272-1294.

4. Guggenheim, E.A., Statistical thermodynamics of mixtures with zero energies of mixing, Proceedings of the Royal Society of London. Series A, Mathematical and Physical Sciences, 1944; 183: 203-212.

5. Dimarzio, E.A., On the second-order transition of a rubber, Journal of Research of the National Bureau of Standards-A. Physics and Chemistry, 1964; 68A: 611-617.

6. Fox, T.G.J., Flory, P.J., Second-order transition temperatures and related properties of polystyrene. I. Influence of molecular weight, Journal of Applied Physics, 1950; 21: 581-591.

7. Rogers, S.S., Mandelkern, L., Glass formation in polymers, I. The glass transition of the poly-(n-alkyl methacrylates), Glass Formation in Polymers, 1957; 61: 985-990.

8. Grest, G.S., Cohen, M.H., Liquid-glass transition: Dependence of the glass transition on heating and cooling rates, Physical Review B, 1980; 21: 4113-4117.

9. Yonezawa, F., Glass transition and relaxation of disordered structures, Solid state physics, 1991; 45: 179-195.

10. Rouse, P.E., A theory of the linear viscoelastic properties of dilute solutions of coiling polymers, Journal of Chemical Physics, 1953; 21: 1272-1280.

11. Zimm, B.H., Dynamics of polymer molecules in dilute solution: viscoelasticity, flow birefringence and dielectric loss, Journal of Chemical Physics, 1956; 24: 269-278.

12. Mooney, M., A diffusion theory of the visco-elasticity of rubbery polymers in finite elastic strain, Journal of Polymer Science, 1959; XXXIV: 599-626.

13. Ferry, J.D., Viscoelastic properties of polymers, John Wiley & Sons, 1980.

14. Sika AG, Product data sheet, Sikadur-330, Edition 2010-10, Zurich, Sika Schweiz AG.

15. Moussa O., Vassilopoulos, A. P., Keller, T., Experimental DSC-based method to determine glass transition temperature during curing of structural adhesives, Construction and building materials, 2012; 28: 263-268.

16. ASTM Standard E1640-09, Standard test method for assignment of the glass transition temperature by dynamic mechanical analysis. American Society for Testing Materials, 2009.

17. Kawakatsu, T., Statistical physics of polymers: An Introduction, Saiensu-Sha Co., Ltd, Tokyo, Japan, 2001.

3 Effect of thermal lag on glass transition temperature of polymers measured by DMA

Reference Detail

3.1 Introduction

The material properties of polymers, such as the storage modulus, usually change considerably during temperature elevation since the mobility of the molecular chains is increased by the absorbed thermal energy and the entangled or cross-linked structure is loosened. The most significant part of this change takes part when the temperature reaches the glass transition temperature (T_g) of the examined material. The T_g can be defined as the heat capacity-related T_g or the modulus-related T_g [1, 2]. Techniques such as differential scanning calorimetry (DSC) and dynamic mechanical analysis (DMA) have been developed in order to experimentally derive the T_g of polymers. Experimental evidence showed that heating or cooling rates influence the material properties and their variation during glass transition and thus the estimated T_g of the samples [3-5]. Both theoretical and experimental studies have been performed to explain this influence.

A linear relationship between heating rates and the heat capacity-related T_g was established in order to simulate the experimentally observed behavior by Avramov et al. [1]. This relationship assumes that the ratio of the heating rate over the T_g is a function of the activation enthalpy. Crichton and Moynihan [6], however, proved that this latter relationship does not give accurate results for

27

estimation of the T_g of materials with a previous heating or cooling history. Another model describing the effect of heating rates on the heat capacity-related T_g was established by Grest and Cohen [7] and Cohen and Grest [8] using the free volume theory. The free volume was calculated based on the division of the molecules into solid-like cells and liquid-like cells. The T_g was a function of the heat capacity of the material, the entropy and the liquid-like cell fraction and depended linearly on the logarithm of the heating rates. This linear dependence was confirmed by their measurements.

Barton [2] studied the relationship between heating rates and the modulus-defined T_g, i.e. the temperature corresponding to the 50% transition degree during glass transition. He assumed that the heating rate vs. T_g relationship followed the Arrhenius law and validated his assumption by his own experimental results for estimation of the T_g. The Williams-Landel-Ferry (WLF) equation was initially proposed by Ferry [9] and Williams et al. [10] to describe the change of the polymer relaxation processes under isothermal conditions. This equation was also applied to evaluate the influence of cooling rates on the T_g, however without giving accurate results. The T_g of thermoplastics calculated by the WLF equation under cooling conditions showed an error of 20% [11]. The WLF equation was not used however for calculation of the effect of heating rates on the T_g of the examined thermoplastics.

It is today well documented that a thermal lag exists between the temperature measured by the thermometer of the DMA machine and the actual temperature inside the sample. This thermal lag depends on the heating rate, the sample mass and the thermal conductivity of both the sample and the equipment [1, 12-14]. Lacík et al. [14] observed that the storage modulus continued to decrease after the temperature increase in the chamber of the machine ceased, and thus concluded that the specimen temperature continued to increase. Sućeska et al. [15] and Roura and Farjas [16] established models to calculate the value of the thermal lag that they observed by means of DMA and differential thermal analysis (DTA) experiments. According to their findings the thermal lag depends on the heating rates and the thermal resistance of the different parts of the machine. Zhang et al. [17] proposed a heating equipment to reduce to the thermal lag along the specimen during temperature elevation. However, the application of that method resulted in a noticeable temperature gradient through the thickness of the specimen under the heating rate applied during the experiment.

The above-mentioned thermal lag was generally deduced from the change of certain material properties (e.g. storage modulus or heat capacity) with temperature and referred to the temperature difference between the thermocouple of DMA and the specimen. However, the values of this thermal lag were never measured. Another thermal lag may also exist along the length of the specimen during temperature elevation. These two thermal lags invalidate the two assumptions adopted by DMA to derive the storage modulus-temperature curves, i.e. i) the temperature measured by the thermo-

couple of DMA is the same as the specimen temperature, and ii) the rate of decrease of the storage modulus with temperature is the same along the length of the specimen.

Thermal lag experiments using a DMA Q800 (TA Instruments) machine have been conducted on an epoxy and a glass fiber reinforced polyester (GFRP) in this work. During each experiment, the specimen temperature (at two positions) and the air temperature near the thermocouple of the Q800 were measured by thermoresistances (Pt100), in addition to the temperature measurements performed by the Q800, in order to establish the actual thermal lag for different heating rates. A finite volume model has been developed for the simulation of the temperature field inside the furnace of the Q800 instrument during the epoxy experiments. Based on the experimental data and numerical simulation results, the effect of the thermal lag on the storage modulus and *E-T* curves of the epoxy specimen under different heating rates were calculated by a three-state numerical method.

3.2 Experimental work

3.2.1 Material and experimental fixtures

A commercial structural adhesive (Sikadur-330 epoxy) and a pultruded glass fiber-reinforced polyester (GFRP) composite material, both typical materials of civil engineering applications, were examined in this work [18, 19]. The Sikadur-330 is a thixotropic bi-component adhesive from Sika Schweiz AG. The base resin is a bisphenol-A-based epoxy and the main hardener is trimethylhexane-1,6-diamine. This adhesive contains a small quantity of inert inorganic silica-based fillers (<20% by weight). The mixing ratio is 4:1 resin to hardener [20]. The GFRP material (supplied by Fiberline A/S, Denmark) consisted of E-glass fibers embedded in an isophthalic polyester resin [21]. The physical and mechanical properties at ambient temperature (fiber fraction, specific heat capacity and storage modulus) are reported in [5]. The thermal conductivity of the epoxy and the GFRP are 0.29W/(m K) and 0.34W/(m K) respectively [5,22].

Specimens with dimensions 53mm×10mm×3mm were fabricated according to ASTM E1640-09 [23]. In order to exclude the effect of post-curing during the experiment, the epoxy specimens were cured under ambient temperature for 48 hours and then post-cured under 63˚C for 144 hours to approach 100% curing degree (according to [20]). The pultruded GFRP specimens were cut from the Fiberline structural profiles and post-cured under 150˚C for 168 hours to approach 100% curing degree. The T_g of fully cured Sikadur-330 was around 74°C [20] and that of the GFRP material around 162˚C [5].

The three-point-bending fixture of the Q800 machine was employed. The specimen temperature at Positions 1 and 2 (at L/2 and L/6 respectively), denoted as T_1 and T_2 respectively, was measured by

two Pt100 thermoresistances, as shown in Fig. 3.1. They were calibrated before being embedded into the epoxy specimen during its fabrication; their positions are shown in Fig. 3.1. Since the GFRP specimens were not fabricated but cut from structural profiles, two holes had to be drilled in order to insert the Pt100 resistances; the holes were then sealed with epoxy. The encircled numbers in Fig. 3.1 were defined in section 3.3.1.

A third Pt100 thermoresistance was fastened at the same height as the Q800 thermocouple, with an offset distance of 2mm (see Fig. 3.2). The temperatures measured by the third Pt100 and the Q800 thermocouple are denoted T_3 and T_Q respectively. The temperature differences between the two sensors (T_Q-T_3), the Q800 thermocouple and the specimen (T_Q-T_1 or T_Q-T_2) and along the length of the specimen (T_2-T_1) were measured.

3.2.2 T_g of epoxy and GFRP under different heating rates

3.2.2.1! T_Q-T_3 differences under isothermal and temperature elevation conditions

Experiments were conducted to measure the temperature difference between T_Q and T_3 under isothermal and temperature elevation conditions. In the first case an epoxy and in the second case a GFRP specimen was used. Under isothermal conditions, the furnace temperature was increased to 40, 50, 60, 70, 75 and 80°C under 0.5˚C/min and was then kept stable for 40 min. at each temperature. During this process, T_3 and T_Q were continuously measured. The experiments were repeated three times, each time using a new Pt100. The differences between the two measured end-temperatures were always between 1.6 and 2.1˚C, as shown in Table 3.1.

Table 3.1: *Temperature difference T_Q-T_3 under isothermal conditions measured using three Pt100s I-III*

Isothermal condition		40˚C	50˚C	60˚C	70˚C	75˚C	80˚C
	Pt100 I	-1.6	-1.8	-1.8	-2.0	-1.6	-1.7
T_Q-T_3 (°C)	Pt100 II	-1.7	-1.7	-1.8	-2.0	-2.1	-2.1
	Pt100 III	-1.5	-1.5	-1.7	-1.9	-2.0	-2.1

To measure the temperature difference between T_Q and T_3 under temperature elevation conditions, the furnace temperature was first set at 35˚C for 40 min (after a ramp under 0.5˚C/min from ambient temperature, Step 1) to unify the initial temperature. The temperature was then increased from 35˚C to 220˚C under different heating rates ranging from 0.5˚C/min to 10˚C/min (Step 2). After the
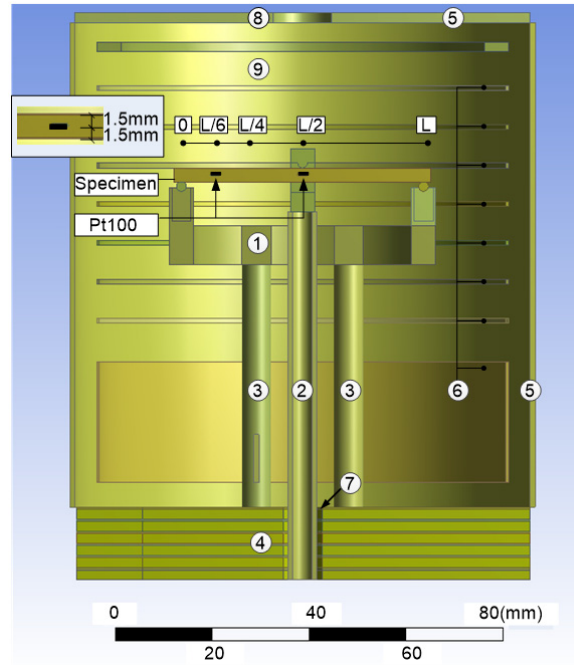
Fig. 3.1: *Positions of Pt100 inside specimen (specimen length L=50 mm, width W=10 mm, positions at W/2)*
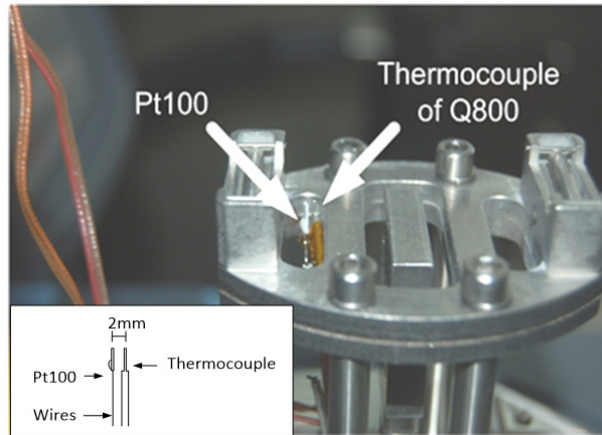

Fig. 3.2: *Pt100 placed near position of Q800 thermocouple*

completion of the temperature elevation process, the specimens were left at ambient temperature for at least two hours in order to cool down naturally. The T_3 and T_Q measured during these two steps are shown in Figs. 3.3-3.4 for 0.5 and 10˚C/min. Under the isothermal conditions of Step 1, T_Q-T_3

was around -1.4˚C, similar to the isothermal results shown above (-1.6 to -2.1˚C). During Step 2, T_Q-T_3increased with time and heating rates from -1.2˚C to a maximum of -1.8˚C for 0.5˚C/min, while the corresponding values under 10˚C/min were -1.6˚C and -9.0˚C respectively.

A consistent difference of approximately 2°C was observed between the thermocouple of the Q800 machine and the Pt100 thermoresistance. Although, since the analysis of this work focuses on trends, this doesn't affect the conclusions.
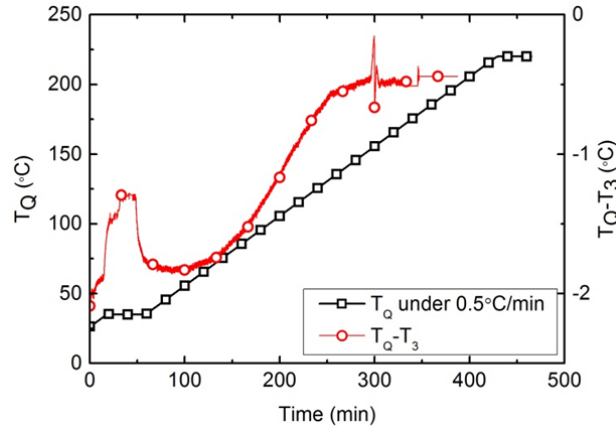
Fig. 3.3: *Comparison between T_3 and T_Q under 0.5˚C/min*
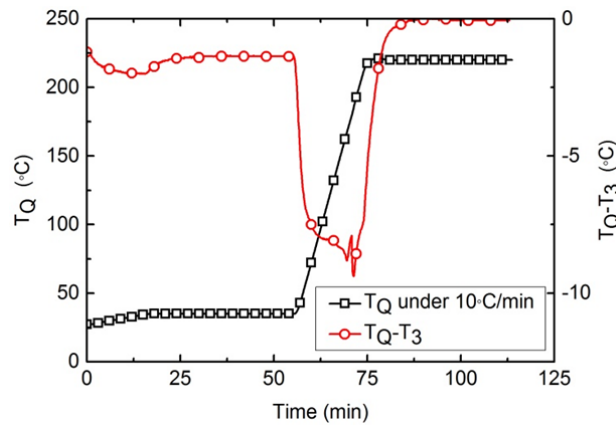
Fig. 3.4: *Comparison between T_3 and T_Q under 10˚C/min*

3.2.3 T_g and thermal lag under different heating rates

The modulus-related T_g used in this work is defined as the average value between $T_{g,onset}$ (the tangent line intersection of the glassy state and glass transition, see Fig. 3.5) and $T_{g,rubber}$ (the tangent line

intersection of glass transition and the rubbery state, see Fig. 3.5). The T_g of the epoxy and the GFRP derived by the Q800 (T_g) under different heating rates are presented in Figs. 3.6-3.7 (standard deviations obtained from three specimen measurements are also shown). The temperatures monitored by the Pt100 thermoresistance at Positions 1-3 when the T_g was reached (denoted as T_{g1}, etc.) are also shown.

In the epoxy case (Fig. 3.6), T_g and the corresponding T_{g3} increased with heating rates, with a maximum difference of 10˚C recorded at 10˚C/min. During the increase in heating rates two thermal lags developed: one between the Q800 thermocouple and Position 2 of the epoxy specimen and one between Positions 1 and 2 inside the epoxy specimen. The value of the first thermal lag (T_g-T_{g2}) reached 3.6˚C at 10˚C/min while that of the second (T_{g2}-T_{g1}) increased to 10˚C at 10˚C/min. The maximum standard deviation of ±2˚C was measured at Position 2 for 10˚C/min and was caused by the airflow inside the furnace. The air speed inside the furnace was accelerated by the increase in heating rates and led to movement of the connecting wires between the Pt100 and the temperature monitor (a Spider 8 measuring device from HBM), which slightly affected the temperature measurement results under high heating rates.
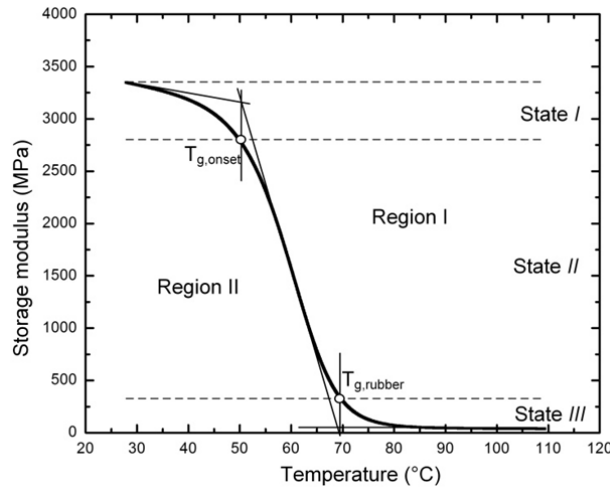
Fig. 3.5: *Three states and two regions used in numerical simulation*

In the GFRP case (Fig. 3.7), all temperatures increased with heating rates with a maximum difference of 17.9˚C recorded from T_{g3} from 0.5 to 10˚C/min. The differences between T_g-T_{g2} and T_{g2}-T_{g1} increased to around 3.3˚C and 7.2˚C respectively at 10°C/min. These values were different from those of the epoxy specimen due to the different temperature elevation range (66.6˚C of epoxy vs.

173.3˚C of GFRP) and the different thermal conductivity of the examined materials. The maximum standard deviation measured by Pt100 was ±1.7˚C and could be attributed to the same reason as mentioned above for the epoxy specimen.
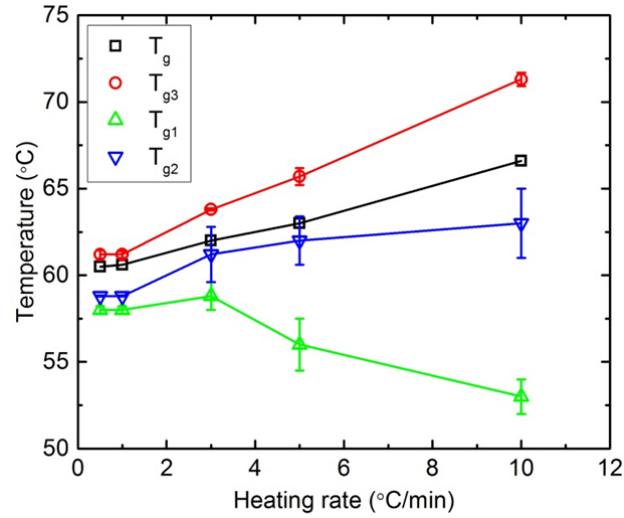
Fig. 3.6: *Effect of heating rate on T_g of epoxy*
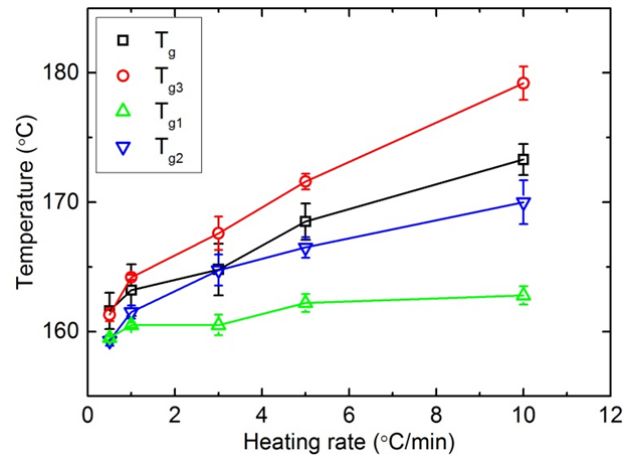
Fig. 3.7: *Effect of heating rate on T_g of GFRP*

The temperature difference between the surface and the center of the specimen was estimated, based on data from Bai [24] and the thermal diffusivity of the epoxy (1.3×10-6 m^2/s from Ciecierska et al. [25]. Difference less than 1°C was estimated under the heating rate of 10°C/min, while lower values resulted for lower heating rates. Therefore this difference was not considered in this investigation.

DMA experiments involving polymers with and without fibers were performed to demonstrate that thermal lags exist in both cases during temperature elevation. However, only the behavior of polymers with isotropic properties, i.e. the aforementioned epoxy resin, is analyzed in the following.

3.3 Finite volume analysis

3.3.1 Finite volume model description

A finite volume model (FVM) was established by ANSYS Workbench Version 13 to simulate the thermal environment inside the furnace and the temperature distribution inside the epoxy specimen during temperature elevation.

Seven critical parts of the Q800 furnace are included in the finite volume model as shown in Fig. 3.1 and as follows:

1) The clamp composed of a frame to support the specimen,

2) The driveshaft to apply the load,

3) The cylindrical columns installed to support the clamps,

4) Six steel layers with air in between to prevent heat transfer between the lower part of the machine and the furnace,

5) The insulating layer to prevent heat dissipation from the furnace to the atmosphere,

6) 28 wire loops that release the required amount of heat to maintain the desired heating rates,

7) The inlet in the steel layers (Part 4) through which the driveshaft is connected with the base and the air from the base can flow into the furnace,

8) The opening at the top of the furnace, which is an outlet for the airflow inside the furnace during temperature elevation,

9) The air inside the furnace.

The material properties (including density, specific heat capacity, thermal conductivity and thermal emissivity coefficient) of all furnace parts are given in Table 3.2.

Table 3.2: *Material properties used in finite volume analysis*

Part	Material	Density	Specific Heat Capacity	Thermal Conductivity	Thermal Emissivity Coefficient [29]
		(kg/m^3)	(J/(kg·K))[26-28]	(W/(m·K))[22, 28]	
Specimen	Epoxy	1300	1000	0.29	0.91
Clamps	Sanded Stainless Steel	7750	502	16.3	0.42
Steel sheet	Stainless steel	7750	502	16.3	0.16
Wires	Nickel	8885	456	67	0.90
Furnace	Copper	8941	385	391	0.02

Three boundary conditions were introduced in the model: adiabatic boundaries for the outer faces of the furnace and the steel layers (Parts 4 and 5 in Fig. 3.1); the inlet (Part 7) with an estimated air speed of approximately 0.01m/s and an air temperature of 20˚C; the opening (Part 8) with an air pressure of 1 atm.

The power generated by the wires (Part 6 in Fig. 3.1) is a necessary input for the FVM and was assumed as being proportional to the heating rates. The power-time curve under the reference heating rate (5˚C/min in this work, see Fig. 3.8) was obtained by an iterative process aiming to reproduce the measured temperature-time (T-t) curve under this heating rate. As shown in Fig. 3.9, the reproduced T_2-t curve based on the assumed energy-time curve fits the corresponding measured curve. A slight underestimation and overestimation before and after 60˚C were observed. An acceptable fitting was also obtained for the T_3-t curve for the temperature range above 70˚C, with a maximum overestimation of 5˚C of the experimental curve for temperatures lower than 70˚C.

3.3.2 FV modeling of heat transfer

The computation of heat transfer in FVM is based on seven basic parameters: the temperature (T), the energy source (S_E) and the enthalpy (h) of the solid and fluid parts (referring to Parts 1-6 and the air respectively); the density (ρ), the pressure (p), the velocity (U), and the stress during the air-flow (τ) of the fluid part in the FVM. These parameters can be calculated by two sets of equations. The first set consists of six basic equations: the thermal energy equation expressing the interrelationship between h, S_E, p, T, U and τ: $f_l(h, S_E, p, T, U, \tau)$=0); the continuity equation expressing the
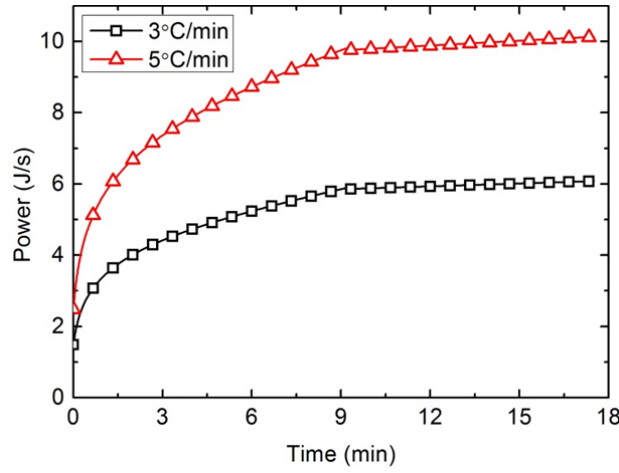
Fig. 3.8: *Power-time curve for FV simulation*
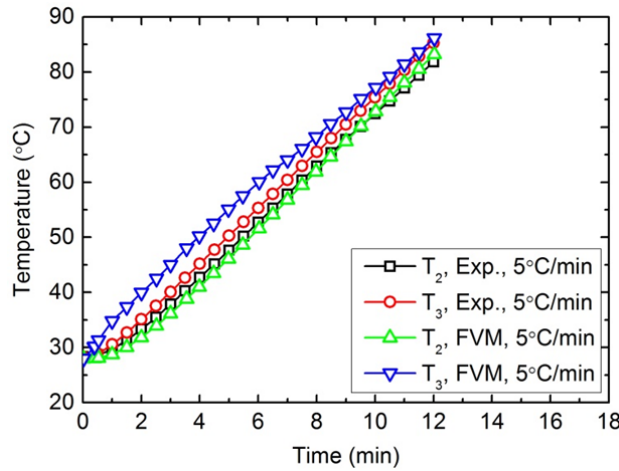
Fig. 3.9: *Comparison between FVM results and experimental data at Positions 2 and 3 under 5˚C/min*

interrelationship between ρ and U: $f_2(\rho,\ U)=0$; the momentum equation expressing the interrelationship between U, ρ, p and τ: $f_3(\rho,\ p,\ U,\ \tau)=0$; the equations of states expressing the interrelationship between T, ρ, p and h: $f_4(\rho,\ p,\ T)=0$ and $f_5(h,\ T)=0$; and the conjugate heat transfer equation for solid parts expressing the interrelationship between T, h and S_E: $f_6(h,\ S_E,\ T)=0$. The second set consists of equations considering special boundary conditions or energy release conditions. The heat generated by the wires is transferred inside the furnace along two paths: a) wires→air→(clamps /

supports / specimen / steel layers / insulating layer) (Parts 1-5 in Fig. 3.1), by thermal conduction and thermal convection; b) wires→(clamps / supports / specimen / steel layers / insulating layer) →air, by thermal radiation, thermal conduction and thermal convection. The sequence of Parts 1-4 and the air is reversed in the second case since the thermal radiation energy is directly absorbed by Parts 1-4 with negligible absorption by the air. The thermal conduction in these two paths is analyzed by the first set of equations and the analysis of the thermal convection and the thermal radiation is based on both sets of equations. For thermal convection, the required second set of equations is a τ-U equation (denominated as the wall function), which is employed to estimate the stress of the airflow at the air-solid interface. For thermal radiation, the required second set of equations comprises the spectral radiative transfer equation (a radiation intensity-emissivity relationship taking into account the thermal radiation energy released by the wires) and equations from the surface-to-surface model to estimate the received thermal energy by Parts 1-4 [30].

Initially, the temperature field of one solid or fluid part of the FVM can be obtained since the number of unknown parameters is the same as the number of equations for this part. In Part 6, for example, S_E is provided by the energy-time curve and the remaining unknown parameters of this part, T and h, can be solved by the equation of states and the conjugate heat transfer equation. These calculated values of the selected parts become the initial values of the adjacent parts and the same calculation process can be repeated until the basic parameters of all the solid and fluid parts in the model have been obtained. The temperature field of the model is then obtained by extracting the basic parameter, T, from all the modeled parts by Ansys Workbench.

3.3.3 FV model validation and results

In order to validate the assumption that the energy released by the wires is proportional to the heating rates, the energy-time curve of 3˚C/min was deduced from the curve under the reference heating rate (5˚C/min), see Fig. 3.8. The corresponding T_2-t and T_3-t curves were calculated by FVM and compared with the measured curves in Fig. 3.10.

As shown in Fig. 3.10, the calculated T_2-t curve was able to simulate the measured values up to 80˚C with a maximum underestimation of 1.7˚C. The calculated T_3-t curve deviated from the experimental value within a range of 3˚C for temperatures lower than 55˚C. The slope of the calculated T_3-t curve above 55˚C slightly changed and stabilized at 2.7˚C/min, 0.3˚C/min lower than the experimental value. The difference between the experimentally observed thermal lag between T_{g3} and T_{g2} and that obtained by FVM was 3.7˚C, overestimating the measured value by 1.9˚C. The FV model is thus able to predict the temperature field inside the furnace up to the T_g of the epoxy and can therefore be

used to study the temperature distribution of the epoxy during temperature elevation during glass transition.
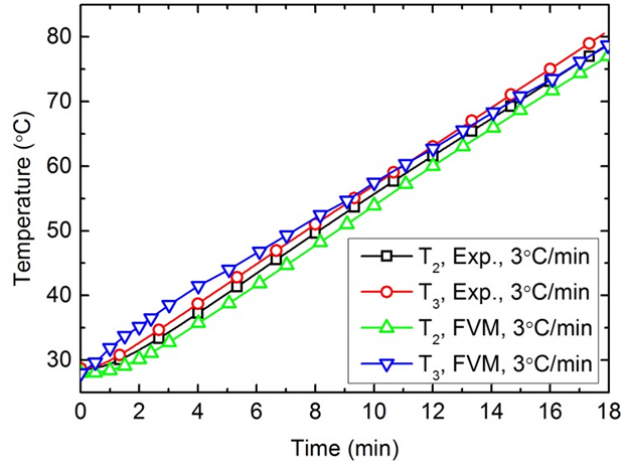
Fig. 3.10: *Comparison between FVM results and experimental data at Positions 2 and 3 under 3˚C/min*
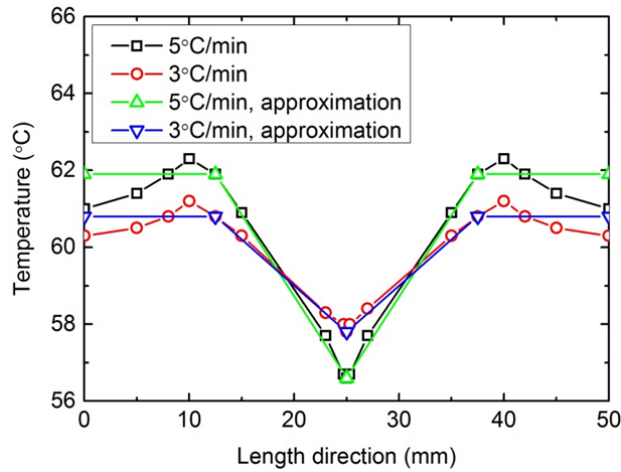
Fig. 3.11: *FVM temperature distribution along length of specimen under 3˚C/min and 5˚C/min*

A symmetrical temperature distribution along the length of the specimen resulted from FVM, as shown in Fig. 3.11, with a small temperature increase between 0 and $L/4$ (0.5˚C and 1˚C for 3˚C/min and 5˚C/min) and then a significant decrease towards the minimum temperature from $L/4$ to $L/2$ (3˚C and 5.3˚C for 3˚C/min and 5˚C/min). The thermal lag between T_2-T_1 captured by FVM was 3˚C and

5.3°C under 3°C/min and 5°C/min, which represented a 0.6 overestimation and 0.7°C underestimation of the measured values (2.4°C and 6°C under 3°C/min and 5°C/min respectively). The temperature at mid-span ($L/2$) was lower than in the other parts since the thermal radiation energy was blocked by the driveshaft (Part 2 in Fig. 3.1). This effect diminished and finally almost vanished at $L/4$. The blocking effect increased with increasing heating rate and led to a much more obvious thermal lag under high heating rates. Considering the small temperature difference between 0 and L/4, a plateau was assumed, as shown in Fig. 3.11, to simplify the calculation process in the following.

3.4 Numerical model

3.4.1 Basic assumptions

The storage modulus of the epoxy is estimated by the Q800 instrument software by Eq. (3.1) based on the assumption that the beam specimen is heated uniformly and therefore the storage modulus of each part of the specimen decreased at the same rate.

$$d = \frac{FL^3}{48E(T_c)I} + \frac{F(1+v)t^2L}{20E(T_c)I} \Rightarrow E(T_c) = \frac{FL^3}{48dI} + \frac{F(1+v)t^2L}{20dI} \tag{3.1}$$

where d is the specimen displacement at mid-span ($L/2$ in Fig. 3.1), F is the measured force at the mid-span loading point, I is the moment of inertia, L is the length, t is the thickness of the specimen, T_c is the constant temperature of the sample, $E(T_c)$ is the corresponding storage modulus, and v is the Poisson ratio. The temperature effect on Poisson ratio was not modeled in this work due to the insiginificant contribution of the shear stress to the deflection of the beam.

However, as described above, thermal lags have been observed between the specimen and the thermocouple of the Q800 instrument as well as along the length of the specimen under heating rates higher than 0.5°C/min (see Figs. 3.6 and 3.7). The effective storage modulus of the specimen is therefore lower than $E(T_c)$ obtained from Eq. (3.1). A modified equation, based on the principle of virtual work, is therefore proposed in this work for the estimation of the displacement, d, along the sample length x, taking into account the non-constant storage modulus caused by the temperature differences along the sample length:

$$d = \frac{F}{2I}\int_{L/4}^{L/2}\frac{x^2}{E(\beta,T)}dx + \frac{Ft^2}{20I}\int_{L/4}^{L/2}\frac{1}{G(\beta,T)}dx + \frac{FL^3}{384IE(\beta_c,T_c)} + \frac{Ft^2L}{80IG(\beta_c,T_c)} \Rightarrow$$

$$d = \frac{F}{2I}\int_{L/4}^{L/2}\frac{x^2}{E(\beta,T)}dx + \frac{Ft^2(1+v)}{10I}\int_{L/4}^{L/2}\frac{1}{E(\beta,T)}dx + \frac{FL^3}{384IE(\beta_c,T_c)} + \frac{F(1+v)t^2L}{40IE(\beta_c,T_c)}$$

(3.2)

$$G(\beta,T) = \frac{E(\beta,T)}{2(1+v)}$$

(3.3)

$$G(\beta_c,T_c) = \frac{E(\beta_c,T_c)}{2(1+v)}$$

(3.4)

where T, β, $E(\beta,T)$, $G(\beta,T)$ are the temperature, the heating rate, the storage modulus and the G-modulus of the specimen of the $L/4$ to $L/2$ part (see Figs. 3.1 and 3.11), T_c, β_c are the constant temperature and the heating rate of the sample between 0 and $L/4$ and $E(\beta_c,T_c)$, $G(\beta_c,T_c)$ the corresponding E- and G-moduli.

A three-state fitting method has been used in order to define the temperature- and heating rate-dependent storage modulus ($E(\beta, T)$) of the epoxy based on the following two assumptions:

1) The E-T response at 0.5°C/min, estimated by the Q800, can be considered as being not affected by thermal lags because T_g-T_{g2} and T_{g2}-T_{g1} are small and limited to 2°C and 0.16°C respectively (see Fig. 3.6).

2) The E-T curve can be divided into three states, as shown in Fig. 3.5. The two common temperatures between the three states are $T_{g,onset}$ and $T_{g,rubber}$ respectively. The storage modulus at the end of each state is the same for different heating rates; however, the common temperature is different (i.e. the horizontal dashed lines in Fig. 3.5 do not change).

The reason the E-T curve was divided into three states is that a fitting function without any division would comprise six fitting parameters, as shown in Eq. (3.5):

$$E(\beta,T) = E_0\frac{(T\times 20 + a_1)^{a_2(a_3+a_4\times\tanh(\frac{T}{a_5}-a_6))}}{(T_0\times 20 + a_1)^{a_2(a_3+a_4\times\tanh(\frac{T_0}{a_5}-a_6))}}$$

(3.5)

where $E(\beta,T)$ is the storage modulus during glass transition, E_0 is the storage modulus at the initial temperature T_0, T is the temperature measured by the Q800 thermocouple, and a_1, a_2, a_3, a_4, a_5, and a_6 are heating rate-dependent fitting parameters. The solution of such a multiparametric optimization problem does not usually lead to unique solutions. In the proposed three-state method the number of fitting parameters can be reduced to one per state: s_I, s_{II}, s_{III} for States I, II and III respectively, as shown below in Eqs. (3.6-3.8).

41

3.4.2 Computation procedure

The decrease of the storage modulus of polymers during temperature elevation is commonly approximated by the Arrhenius law [5, 9]. Accordingly, three exponential functions were employed to model the *E-T* behavior of the epoxy at the three states as follows:

$$E_I(\beta,T) = E_{Ii} - 10^6 \times 70 \times (e^{\frac{T-T_{Ii}}{s_I}} - 1)$$ (3.6)

$$E_{II}(\beta,T) = E_{If} - 10^6 \times 2250 \times (e^{\frac{T-T_{If}}{s_{II}}} - 1)$$ (3.7)

$$E_{III}(\beta,T) = E_{IIIf} + (E_{IIf} - E_{IIIf}) \times e^{-\frac{T-T_{IIf}}{s_{III}}}$$ (3.8)

where $E_I(\beta,T)$, $E_{II}(\beta,T)$ and $E_{III}(\beta,T)$ are the storage moduli of States *I*, *II* and *III* respectively, T_{Ii} is the initial temperature of State *I* and E_{Ii} is the corresponding storage modulus, T_{If} and T_{IIf} are the temperatures at the end of States *I* and *II*, E_{If}, E_{IIf} and E_{IIIf} are the *E*-moduli at the end of States *I*, *II* and *III* respectively, 70 and 2250 are the fitting coefficients which do not vary with heating rates and can be obtained by fitting the *E-T* curve under 0.5°C/min, and s_I, s_{II}, s_{III} are the fitting parameters for States *I*, *II* and *III* respectively. The *E-T* curve of a uniformly heated specimen under heating rates higher than 0.5°C/min can be located in Region *I* (the storage modulus increases with increasing heating rates) or Region *II* (the storage modulus decreases with increasing heating rates), see Fig. 3.5. For each state, the corresponding equations Eqs. (3.6-3.8) are capable of reproducing *E-T* curves in both the regions, depending on the selected value of the corresponding fitting parameter. In State *I*, for example, the calculated *E-T* curve can be moved from Region I to Region II by decreasing the value of s_I, see Fig. 3.12.

The parameters in Eqs. (3.6) to (3.8) corresponding to the *E-T* curve under 0.5˚C/min were calculated and are listed in Table 3.3. According to assumption 2, the initial storage modulus (E_{Ii}), the *E*-moduli at the end of each state (E_{If}, E_{IIf} and E_{IIIf}) and the initial temperature (T_{Ii}) are independent of heating rates. T_{If} in Eq. (3.7), as mentioned above, is the temperature *T* in Eq. (3.6) when $E_I(\beta, T) = E_{If}$ and its value can be calculated when s_I has been determined by the three-state method. The value of T_{IIf} can be obtained by following the same procedure using Eqs. (3.7) and (3.8). The fitting parameters, s_I, s_{II} and s_{III}, vary with heating rates. To avoid a multiparametric optimization problem, a linear relationship between s_i and heating rates was assumed as follows:

$$s_i^\beta = \frac{s_i^{10} - s_i^{0.5}}{9.5} \times (\beta - 0.5) + s_i^{0.5}$$ (3.9)

where s_i^β refers to s at State i, with i=I, II, III, under any desired heating rate, β. The estimation of s_i^β is based on $s_i^{0.5}$ and s_i^{10}. The former is given in Table 3.3 and the latter is determined as described in the following at the maximum heating rate applied during the experiments (10˚C/min).
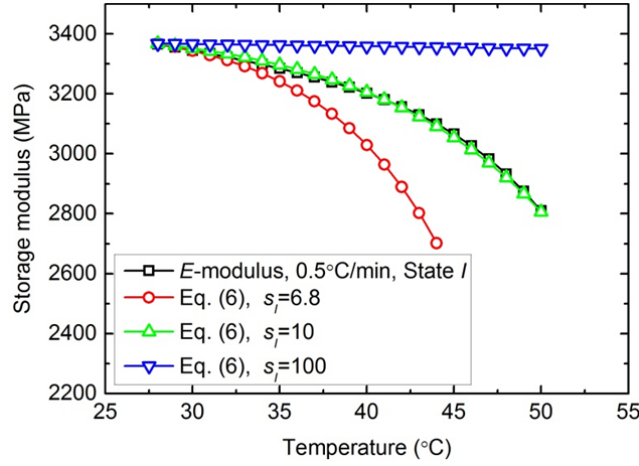

Fig. 3.12: *Numerical fitting of State I using different values of s_I*

Table 3.3: *Parameters for* storage *modulus-temperature curve under 0.5°C/min*

Parameter	$s_I^{0.5}$	$s_{II}^{0.5}$	$s_{III}^{0.5}$	E_{Ii} (MPa)	E_{If} (MPa)	E_{IIf} (MPa)	E_{IIIf} (MPa)	T_{Ii} (°C)
Value	10	25	4.5	3367	2805	432	32	28

Substitution of s_I, s_{II}, s_{III} from Eq. (3.7) and the known values of the other parameters from Table 3.3 into Eqs. (3.6-3.8) gives the following equations that can be used for calculation of the storage modulus across the three states as a function of the heating rate:

$$E_I(\beta,T) = 3367 \times 10^6 - 10^6 \times 70 \times (e^{\frac{T-301}{\frac{s_I^{10}-10}{9.5} \times (\beta-0.5)+10}} - 1) \tag{3.10}$$

$$E_{II}(\beta,T) = 2805 \times 10^6 - 10^6 \times 2250 \times (e^{\frac{T-T_{If}}{\frac{s_{II}^{10}-25}{9.5} \times (\beta-0.5)+25}} - 1) \tag{3.11}$$

$$E_{III}(\beta,T) = 32 \times 10^6 + 400 \times 10^6 \times e^{-\frac{T-T_{IIf}}{\frac{s_{III}^{10}-4.5}{9.5} \times (\beta-0.5)+4.5}} \tag{3.12}$$

43

The values of a displacement ratio, d_{mod}/d_{exp}, at six temperature points ranging from 40˚C to 80˚C were used to estimate the value of s_i^{10} at the different states. d_{mod} is the displacement resulting from Eq. (3.2) and Eqs. (3.10-3.12) and d_{exp} is the experimental displacement. s_I^{10} in Eq. (3.10) was obtained by setting the corresponding d/d_e equal to 1. With s_I^{10} defined, the T_{If} for any heating rate was calculated from Eq. (3.10) by setting $E_I(T) = E_{If} = 2805 \times 10^6$, which is independent of the heating rate. The same process was applied sequentially for the calculation of s_{II}^{10}, T_{IIf} and s_{III}^{10} from Eqs. (3.11) and (3.12).

The physical aging induced to the material during the cooling process, although limited due to the natural cooling of the specimens, is considered by the model, since the model parameters are calibrated by the exhibited E-T curves of the examined material.

3.4.3 Results and discussion

With all parameters estimated, the storage modulus throughout the glass transition temperature range under the examined heating rates was obtained and the results are presented in Fig. 3.13. The values of the fitting parameter are shown in Table 3.4. As shown in Fig. 3.13, all estimated E-T curves for heating rates higher than 0.5˚C/min are located in Region II. The results reveal that the storage modulus of a specimen, excluding the effect of the two measured thermal lags, T_Q-T_2 as well as T_2-T_1, decreases with the increase of heating rates, with a maximum drop of 89% at 66˚C from 0.5˚C/min to 10˚C/min. This result contradicts the measured E-T curves from DMA experiments, as shown in Fig. 3.13 for the experimental E-T curves, which are located in Region I. The difference between T_Q and T_2 leads to a shift of the E-T curves towards Region II since each measured storage modulus corresponds to a lower specimen temperature, and not the temperature measured by the Q800 thermocouple. The storage modulus is further reduced due to the temperature difference between T_2 and T_1.

Table 3.4: *Values of* s_i^{10} *for States I, II and III*

Parameter	s_I^{10}	s_{II}^{10}	s_{III}^{10}
Value	6	25	3

The d_{mod}/d_{exp} ratios derived by the three-state method at six different T_Qs under 3, 5 and 10˚C/min are shown in Fig. 3.14. Values close to 1.0 were obtained for heating rates lower than 10°C/min and temperatures <70°C. The three-state method is therefore able to simulate the effect of thermal lags on

the *E-T* curve under heating rates lower than 10˚C/min only. For heating rates of 10˚C/min and higher, a nonlinear variation of the fitting parameters with heating rates needs to be taken into account, thus complicating the analysis significantly.
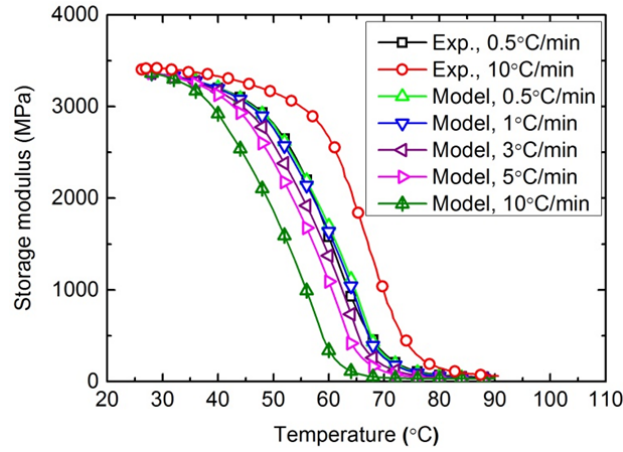

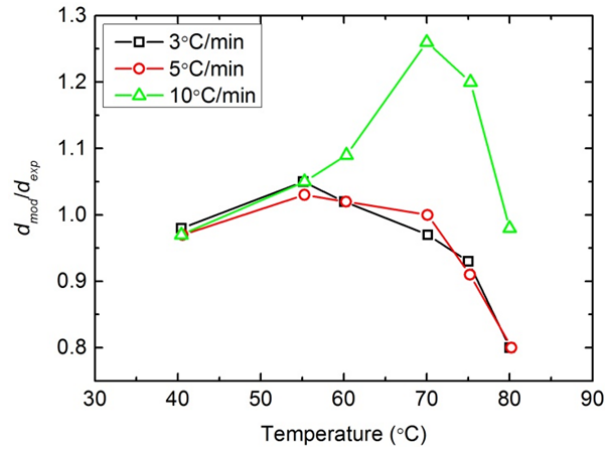***Fig. 3.13:*** *Comparison of experimental and modeled E-T curves for uniformly heated specimens*

Fig. 3.14: *d_{mod}/d_{exp} of three-state method under different heating rates*

The comparison between the T_g calculated by the three-state method (defined as the average value between $T_{g,onset}$ and $T_{g,rubber}$, see Fig. 3.5) and the T_g derived from DMA (defined as the temperature corresponding to the peak of tanδ (T_{ga}) and the average value between $T_{g,onset}$ and $T_{g,rubber}$ (T_{gb})) is shown in Fig. 3.15. The T_g of a uniformly heated polymer decreases with increasing heating rate, and

does not increase as shown in the DMA results. For the epoxy in this work, the T_g decreased by 8.8°C when the heating rate was increased from 0.5˚C/min to 10˚C/min.
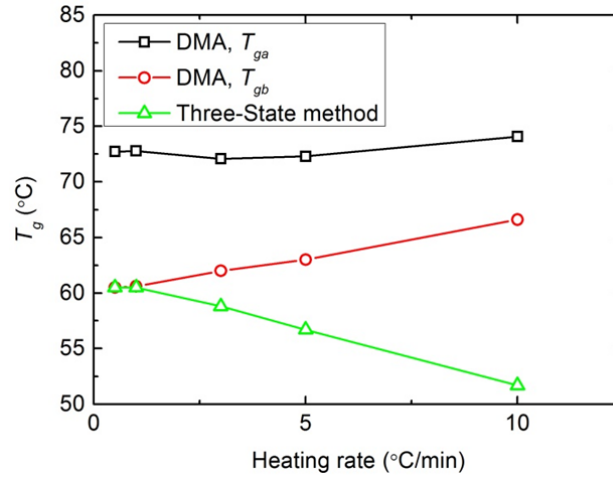

Fig. 3.15: *Comparison of T_g derived by DMA and three-state method*

The three-state method developed in this work can be used to predict the effects of thermal lags measured by DMA on the *E-T* curves of isotropic materials. To extend it to anisotropic materials, such as the examined GFRP, another fitting parameter, similar to s_i^{10} for the storage modulus, needs to be introduced to consider the *G*-modulus-temperature variation due to the different decrease rates of the *E*- and *G*-moduli during temperature elevation.

3.5 Conclusions

The thermomechanical behavior of two kinds of polymers (a commercial structural adhesive (Sikadur-330 epoxy) and a pultruded glass-fiber-reinforced polyester) measured by DMA was investigated in this work. The experimentally observed thermal lags during DMA were simulated by an FVM and their effects on the *E-T* curves of the isotropic epoxy material were modeled by a three-state method. The following conclusions were drawn:

- Two thermal lags were observed during temperature elevation: the first between the specimen and the Q800 DMA thermocouple and the second along the length of the specimen. Both thermal lags changed with time, heating rate and the thermal conductivity of the material.

- A finite volume model was developed to simulate the temperature elevation process inside the furnace as well as the thermal lag inside the epoxy. It was found that thermal radiation energy was an important heat source for the temperature elevation of the specimen and the shielding of the thermal radiation by the driveshaft was the reason for the thermal lag inside the epoxy specimen.

- The effect of thermal lag during DMA experiments on the mechanical properties of the specimen was significant under heating rates higher than 0.5°C/min. A three-state method is proposed to derive the effective E-T curves of isotropic polymers under a specified heating rate as well as the influence of heating rates on their T_g based on the E-T curve experimentally obtained for non-uniformly heated polymers from DMA.

- During DMA, the storage modulus of an isotropic polymer without thermal lag along its length (under a uniform heating rate) decreases with the increase of heating rates, resulting in a lower derived T_g. The T_g of the examined epoxy was 14.5% lower when measured under 10˚C/min compared to the value measured under 0.5˚C/min. Both results contradict reported experimental E-T curves and T_g values obtained by disregarding the influence of the thermal lag.

References

1. Avramov, I., Grantscharova, E., and Gutzow, I., Structural relaxation in two metaphosphate glasses, Journal of non-crystalline solids, Volume 91, 1987, pp. 386-390.

2. Barton, J.M., Dependence of polymer glass transition temperature on heating rates, Polymer, Volume 10, 1969, pp. 151-154.

3. Li, G., Lee-Sullivan, P., and Thring, R.W., Determination of activation energy for glass transition of an epoxy adhesive using dynamic mechanical analysis, Journal of Thermal Analysis and Calorimetry, Volume 60, 2000, pp. 377-390.

4. Saffell, J.R., The effects of heating and cooling rate on the characteristics of the calorimetric glass transition for glassy polymers, Thermlchimica Acta, Volume 36, 1980, pp. 251-264.

5. Bai, Y., Post, N. L., Lesko, J.J. and Keller, T., Experimental investigation on temperature-dependent thermo-physical and mechanical properties of pultruded GFRP composites, *Thermochimical Acta*, Volume 469, 2008, pp. 28-35.

6. Crichton, S.N., and Moynihan, Dependence of the glass transition temperature on heating rates, Journal of non-crystalline solids, Volume 99, 1988, pp. 413-417.

7. Grest, G.S., and Cohen, M.H., Liquid-glass transition: dependence of the glass transition on heating and cooling rates, Physical review B, Volume 21, 1980, pp. 4113-4117.

8. Cohen, M.H., and Grest, G.S., Liquid-glass transition, a free-volume approach, Physical review B, Volume 20, 1979, pp.1077-1098.

9. Ferry, J.D., Mechanical properties of substances of high molecular weight. VI. Dispersion in concentrated polymer solutions and its dependence on temperature and concentration, Journal of the American Chemical Society, Volume 72, 1950, pp. 3746-3752.

10. Williams, M.L., Landel, R.F., and Ferry J.D., The temperature dependence of relaxation mechanisms in amorphous polymers and other glass-forming liquids, Journal of the American Chemical Society, Volume 77, 1955, pp. 3701-3707.

11. Chinnasamy, T. V., and Harimurthi, K., A comparative study of the kinetic and thermodynamic approaches to the glass transition phenomenon in high polymers, Thermochimica Acta, Volume 118, 1987, pp. 159-181.

12. Saffell, J.R., The effects of heating and cooling rate on the characteristics of the calorimetric glass transition for glassy polymers, Thermochimica Acta, Volume 36, 1980, pp. 251-264.

13. Tarifa, S., and Bouazizi, A., Glass transitions in crosslinked epoxy networks: kinetic aspects, Journal of Thermal Analysis, Volume 48, 1997, pp. 297-307.

14. Lacík, I., Krupa, I., Stach, M., Kučma, A., Jurčiová, J., and Chodák, I., Thermal lag and its practical consequence in the dynamic mechanical analysis of polymers, Polymer Testing, Volume 19, 2000, pp.755-771.

15. Sućeska, M., Liu, Z.-Y. , Mušanić, S.M. , and Fiamengo, I., Numerical modelling of sample-furnace thermal lag in dynamic mechanical analyser, Journal of Thermal Analysis and Calorimetry, Volume 100, 2010, pp. 337-345.

16. Roura, P., and Farjas, J., Analysis of the sensitivity and sample-furnace thermal-lag of a different thermal analyzer, Thermochimica Acta, Volume 430, 2005, pp. 115-122.

17. Zhang, Y., Adams, R.D., and da Silva, L.F.M., A rapid method of measuring the glass transition temperature using a novel dynamic mechanical analysis method, The Journal of Adhesion, Volume 89, 2013, pp.785-806.

18. Keller, T., Bai, Y., and Vallée, T., Long-term performance of a glass fiber-reinforced polymer truss bridge, Journal of composite and construction, Volume 11, 2007, pp. 99-108.

19. Keller, T., Rothe, J., de Castro, J., and Osei-Antwi, M., GFRP balsa sandwich bridge deck: Concept, design and experimental validation, Journal of composite and construction, 2013, DOI: 10.1061/(ASCE)CC.1943-5614.0000423.

20. Moussa O., Vassilopoulos, A. P., Keller, T., Experimental DSC-based method to determine glass transition temperature during curing of structural adhesives, Construction and building materials, Volume, 28, 2012, pp.263-268.

21. Fiberline Composite (2003). *Fiberline Desgin Manual*, Kolding, Denmark.

22. Ganguli, S., Roy, A.K. and Anderson D.P., Improved thermal conductivity for chemically functionalized exfoliated graphite/epoxy composites, *Carbon*, Volume 46, 2008, pp.806-817.

23. ASTM, E1640-09, Standard test method for assignment of the glass transition temperature by dynamic mechanical analysis.

24. Bai Y. and Keller, T, Effect of thermal loading history on structural adhesive modulus across glass transition, Construction and Building Material, Volume 25, 2011, pp. 2162-2168.

25. Ciecierska, E., Boczkowska, A., kurzydlowski, K.J., Rosca I.D., and Hoa, S.V., The effect of carbon nanotubes on epoxy matrix nanocomposites, Journal of Thermal Analysis and Calorimetry, Volume 111, 2013, pp. 1019-1024.

26. Sika AG, Product data sheet, Sikadur-330, Edition 2010-10, Zuric, Sikad Schweiz AG.

27. Frank, K., The CRC handbook of thermal engineering, Boca Raton: CRC Press, 2000.

28. Philip A. Schweizer, P.E., Metallic materials, physical, mechanical, and corrosion properties, Marcel Dekker, Inc., New York, 2003.

29. Siegel, R., and Howell J.R., Thermal radiation heat transfer second edition, Hemisphere Publishing Corporation, Washington, New York, London, 1981.

30. ANSYS, Inc. (2012), ANSYS 14.5 Help, Canonsburg, Pennsylvania, United States.

4 Experimental investigation of kink initiation and kink band formation in unidirectional glass fiber-reinforced polymer specimens

Reference Detail

4.1 Introduction

Fiber-reinforced polymer (FRP) components used in civil engineering applications are often subjected to compressive loads. Compared to the tensile strength of FRP materials, the compressive strength is usually lower and shows more scatter due to fiber misalignments and initial imperfections caused during fabrication. Furthermore, the compressive material properties of composites are sensitive to temperature elevations occurring in engineering applications, as for example below the asphalt layer in FRP composite bridge decks [1]. Temperatures in such cases can reach 90°C, approaching the glass transition temperature (T_g) of the resin and softening the composite material.

The compressive failure mode of FRP specimens can be associated with fiber failure, splitting, kinking, or the combination of kinking and splitting. Fiber failure is a common failure mode of fibers that are weak in compression, like aramid fibers, and an unusual failure mode for carbon or glass fibers [2]. Splitting is a typical compressive failure mode of composites with low interfacial shear strength, e.g. carbon fiber-reinforced polymers (CFRP), and is accompanied by

crack propagation, inside the matrix or at the interface, along the loading direction [3]. Kinking is a failure mode in which one part of the material is displaced relatively to another along an inclined path with respect to the loading direction. Kinking failure has been observed in both CFRP and glass fiber-reinforced polymer (GFRP) composites [4]. Compared to the mechanisms dominating fiber failure, splitting, and kinking development, those causing kinking initiation are more complicated and a generally accepted explanation of their initiation based on solid experimental evidence is still lacking.

The first works concerning the experimental investigation of the kinking failure in fiber-reinforced composites can be traced back to 1964. Rosen [5] observed the microbuckling of fibers during the shrinkage of the resin as the GFRP specimen was cooled from its curing temperature to room temperature. It was therefore derived that kinking under compression is caused by microbuckling since shrinkage is followed by an increase of the compressive stress in the matrix. Later studies [6-8] reported the co-existence of microbuckling and kinking in CFRP laminates and assumed that kinking was a result of the microbuckling.

Kinking resulting from compression fatigue loading of notched specimens was also attributed to microbuckling induced by the crack propagation near the notch tip [9], however, no experimental proof was reported to validate this assumption. Compressive experiments on CFRP specimens [10-12] focused on the kinking band propagation and broadening, contributing only limited information to the identification of the factors leading to kinking. Schultheisz and Waas [2], Weaver and Williams [13], and Wronski and Parry [14] doubted the validity of the causality between microbuckling and kinking since they did not observe any significant microbuckling before or after the kinking failure of the examined specimens.

Elevated temperature can also affect the failure mode of composites in compression. A shift from splitting to kinking, under elevated temperatures, was observed in [15-16] and was attributed to the softening of the matrix and increase of the shear interlaminar stresses. Limited experimental evidence was provided by Grape and Gupta [15] regarding the formation of microbuckling due to shear interlaminar stresses. Although Bazhenov and Kozey [16] failed to observe the failure process experimentally, they measured the compressive strength as a function of fiber volume at an elevated temperature. The relationship followed Rosen's microbuckling theory [5] indicating, indirectly, that microbuckling caused the eventual kinking.

The variation of the failure mode can also be affected by material imperfections, e.g. fiber waviness and voids. Typical wavelengths of prepreg CFRP are between 2.1mm and 5.6mm [17]. The compressive failure strength can be significantly decreased, e.g. by 75% reported in [18], while on the contrary, the width of the kink band can be increased by as much as 45% [19]

with the increase of fiber waviness. As shown by Hancox [20], kinking can observed in low void content materials while splitting failure occurs in the case of materials with a high percentage of voids.

The aforementioned works focused on the investigation of kink band propagation and the effect of temperature and material imperfections on the kinking failure of FRP composites. Even though some phenomena, e.g. the co-existence of microbuckling and kinking, were observed, direct experimental evidence of the effect of microbuckling on kinking initiation, either under ambient or elevated temperature, is still lacking in the literature.

This work investigates the compressive behavior of GFRP prismatic specimens, aiming to reveal the mechanisms initiating kinking failure at temperatures up to 90°C, which corresponds to the onset of glass transition (93°C) of the selected material. Furthermore 90°C represents the maximum temperature to which engineering structures such as bridges are exposed [1]. It is experimentally demonstrated, by surface strain and lateral deformation measurements using digital image correlation (DIC), that fiber microbuckling is responsible for kinking initiation.

4.2 Experimental work

4.2.1 Material characterization

E-glass fiber-reinforced polymer (GFRP) composites, a typical material used in civil engineering applications, were examined in this work. The matrix of the GFRP specimens is a thixotropic bi-component polymer from Swiss Composite AG [21]. The base resin is an epoxy type L and the hardener is EPH 161; the resin to hardener mixing ratio is 4:1. This epoxy has a low viscosity and is free of fillers, which is ideal for impregnating glass fibers. The polymer is reinforced by unidirectional E-glass fiber fabrics (EC 9-68) from Swiss Composite AG, having an area density of $425g/m^2$ and layer thickness of 0.45mm [21].

A GFRP laminate with nominal dimensions of 22x240x500 mm^3 was fabricated by hand-layup achieving a fiber volume fraction of 44% as determined by burn-off experiments. The laminate was initially cured at room temperature for 48 hours and then post-cured at 100°C for 72 hours to approach 100% curing. Ten non-slender specimens with nominal dimensions of 12.7x12.7x50 mm^3 according to ASTM D695-10 were cut from the GFRP laminate [22]. The sample designation and exact dimensions of the examined specimens are shown in Table 4.1.

53

An optical scanning microscope was used for the investigation of the microstructure of the specimens. A specimen with dimensions 13x13x13 mm (see Fig. 4.1a) was cut from the same laminate and appropriately prepared. Several consecutive scans were performed on the surface that is perpendicular to the lamina plane; the obtained microstructure is shown in Figs. 4.1b and 4.1c. As shown in Fig. 4.1b, the rovings were not perfectly straight and exhibited initial imperfections. Average measured wavelengths and amplitudes were 3.23±0.17mm and 0.036±0.003mm respectively, see Table 4.2 (data from nine measurements). Voids, created from air trapped during the hand lay-up fabrication, were also observed in the epoxy near the rovings. Their diameters were similar to the thickness of the epoxy layers. Voids can also exist inside the rovings, as shown in Fig. 4.1c, due to insufficient impregnation of individual fibers during fabrication. Both the fiber waviness and the voids inside and in between the rovings can be locations for crack initiation under the applied compressive loads.
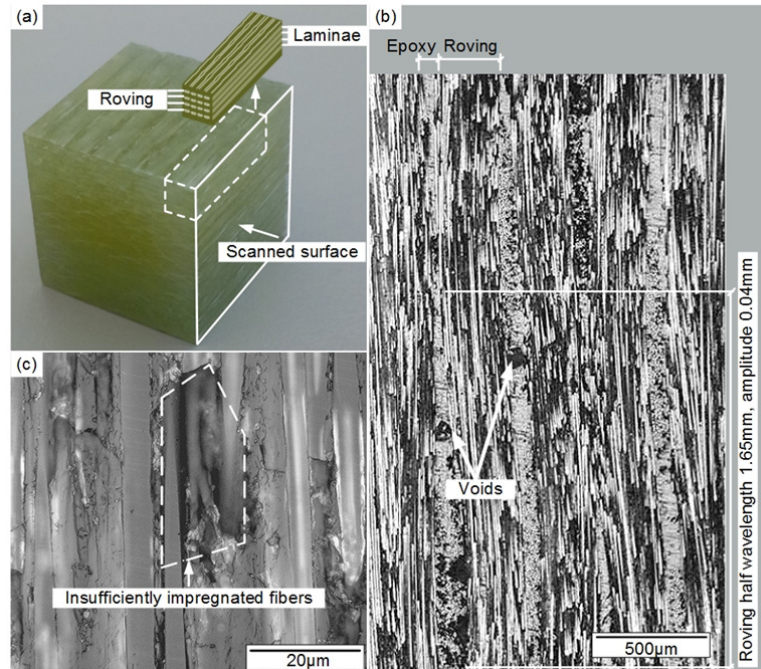

Fig. 4.1: *(a) Specimen for optical microscopy, (b) Fiber waviness and voids in between rovings, (c) Voids inside roving*

In addition to the GFRP specimens used for the compression experiments, epoxy matrix specimens were also investigated. The storage modulus/temperature curve of the epoxy matrix was measured via Dynamic Mechanical Analysis (DMA) since the mechanical response of the GFRP specimens was assumed to be affected by the decrease of the storage modulus of the ma-

trix during temperature elevation. The specimen dimensions were 53x10x3 mm^3, according to ASTM E1640-09 [23]. The epoxy specimens were cured at ambient temperature for 48 hours and then post-cured at 90°C for 72 hours to obtain 100% curing.

4.2.2 Experimental set-up and instrumentation

A tension-compression transfer fixture was designed in order to perform compressive experiments by applying tensile loading. As shown in Fig. 4.2, four steel plates with dimensions of 160×160×40mm^3 were assembled vertically connected by steel bars. During the experiments the part of the fixture connected to the lower grips (plates 2 and 4) was moving down applying compression loads to the specimens that were positioned between plates 2 and 3. The load was applied by an INSTRON 8800 servohydraulic machine with a displacement rate of 0.5mm/min. The specimen displacement was recorded by the machine by monitoring the movement of the loading head.
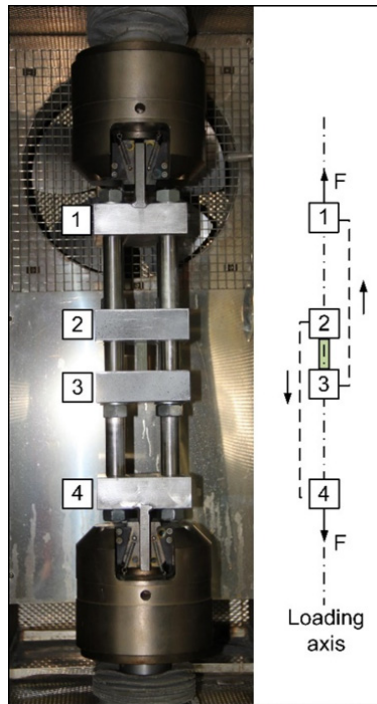

Fig. 4.2: *Tension-compression transfer fixture*

The strain field on one surface of the GFRP specimens was measured by a digital image correlation (DIC) system, as shown in Fig. 4.3. The surface perpendicular to the laminae, in which kinking was expected, was examined and covered prior to the experiment by a speckle pattern consisting of tiny black dots sprayed on top of a white layer. The DIC system comprised two cameras with Pentax lenses of a focal length of 25mm and an aperture of 1.4mm, two lighting panels, a

signal converter and a computer. This system was placed 415mm in front of the specimen, recording surface images with the two cameras at a fixed frequency (1 Hz). The specimen displacements were measured by comparing the position of the speckles at a certain load level to the reference position at 0kN load. The accuracy of the displacement measurement was ±0.0017mm. The strain was estimated by the Lagrange strain tensor based on the measured displacements and the accuracy of the strain obtained was ±0.0015%.
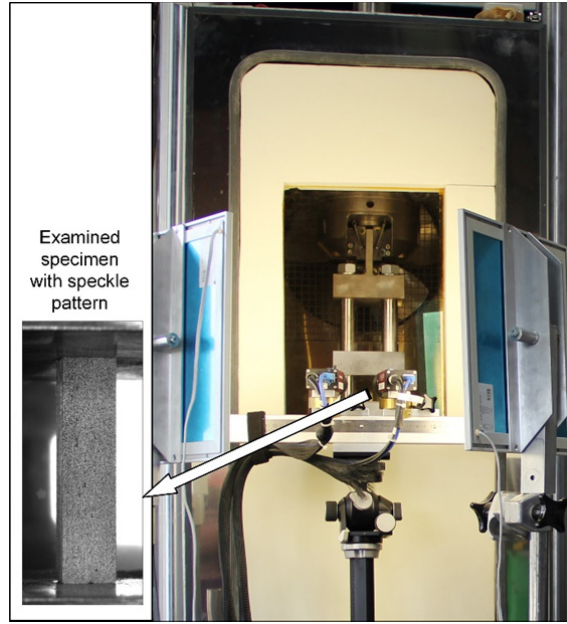

Fig. 4.3: Experimental set-up in climate chamber and zoom on specimen with speckle pattern

A climate chamber was used to apply the target temperature. To validate that an evenly distributed temperature is applied on the examined specimens, a supplementary specimen was used to monitor the through thickness temperature distribution up to 90°C. The temperature was measured at two positions, in the center (T_1) and on the surface (T_2), both at mid-height, by two Pt100 thermo resistances. T_1 was embedded into the specimen by drilling a hole that was subsequently filled with epoxy resin.

The results, shown in Fig. 4.4, reveal that the specimen temperature increased rapidly in the first 700s with a temperature gradient (T_1-T_2) reaching its maximum value of -5.2°C during this period. After 700s, the temperature elevation of the specimen significantly slowed and a homogeneous temperature was reached throughout the specimen volume. The measured temperature

difference was 0.6^{o}C after 2800s. The compressive experiments at 90°C were performed between 2800s and 3045s where the temperature gradient was negligible.

The results, shown in Fig. 4.4, reveal that the specimen temperature increased rapidly in the first 700s with a temperature gradient (T_1-T_2) reaching its maximum value of -5.2°C during this period. After 700s, the temperature elevation of the specimen significantly slowed and a homogeneous temperature was reached throughout the specimen volume. The measured temperature difference was 0.6^{o}C after 2800s. The compressive experiments at 90°C were performed between 2800s and 3045s where the temperature gradient was negligible.
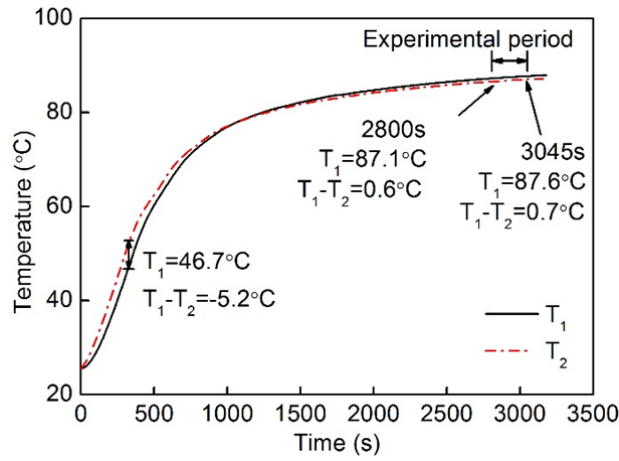

Fig. 4.4: *Temperature gradient through specimen*

4.3 Experimental results

4.3.1 DMA results

The measured storage modulus/temperature curve of the epoxy resin, obtained from DMA, is shown in Fig. 4.5. Three states can be recognized: the glassy state, between ambient temperature and approximately 80°C, the glass transition, between approximately 90 and 110°C with the glass transition onset ($T_{g,onset}$) estimated at 93°C (the tangent line intersection of the glassy state and the glass transition region) and the rubbery state for temperatures above 110°C. The storage modulus decreased by 19% from ambient temperature to 93°C and by 95% at the end of the glass transition, at around 110°C.

4.3.2 Load/displacement curves

The load/displacement curves for the specimens loaded at 25°C are shown in Fig. 4.6. They exhibited an almost trilinear behavior with decreasing stiffness: from approximately 2.1kN (end of the toe region) to 18.1kN, between 18.1 and 36.9kN and from 36.9kN up to the failure load of 66.8kN (all average values); the corresponding stiffness values are given in Table 4.1. The load/displacement curves at 90°C can be approached by a bilinear curve showing a change in stiffness at 19.8kN, see Fig. 4.6 and Table 4.1. The average failure load in this case was 40.9kN, 61% of the average failure load of the specimens loaded at ambient temperature.
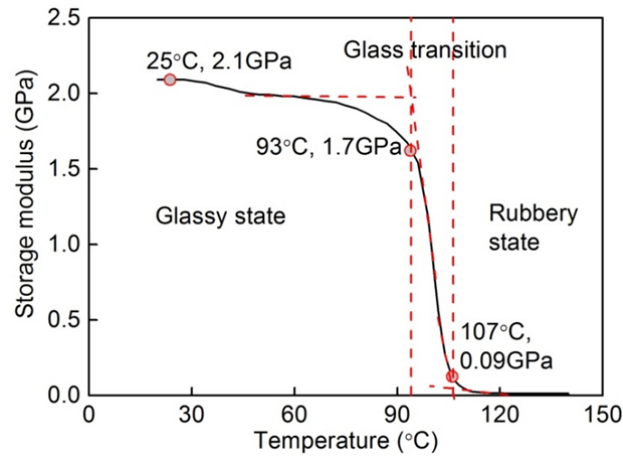

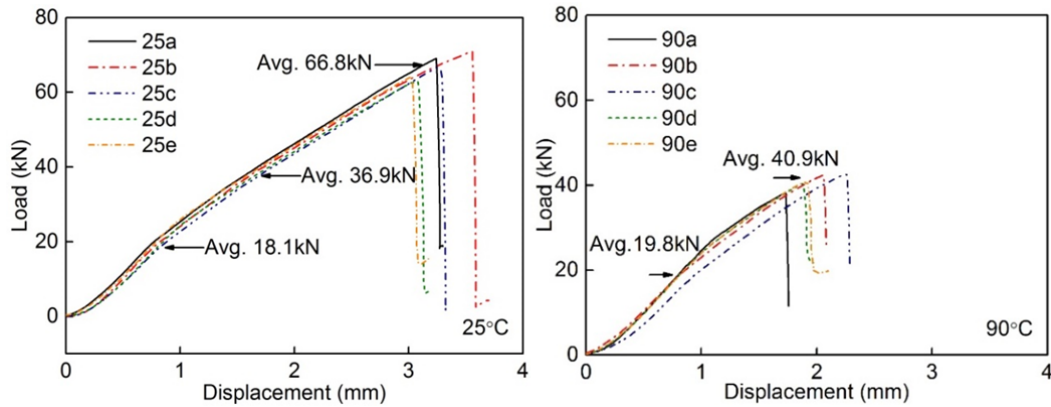**Fig. 4.5:** *Storage modulus/temperature relationship of epoxy resin*

Fig. 4.6: *Load/displacement curves at 25˚C and 90˚C*

58

4.3.3 Failure modes

In all specimens loaded at ambient temperature failure occurred due to splitting between the laminae along the specimen length which was followed by fiber kinking near the boundary, see Fig. 4.7. A different failure mode was exhibited by the specimens loaded at elevated tempera-ture. In this case, the failure mode was kinking occurring in the middle part of the specimen with an average kink band width of 1.8mm±0.1mm and an average kink angle of 31.2°±1.0°, see Table 4.1. The fibers within the kink band buckled and were not broken at the failure load, see Fig. 4.7.

Table 4.1: *Specimen dimensions and compressive results at 25 and 90˚C*

Temperature (°C) & Sample number		Dimensions (mm)	Specimen stiffness (kN/mm)			Failure load (kN)	Kink band		Storage modulus epoxy (GPa)
			1st linear stage	2nd linear stage	3rd linear stage		Width (mm)	Angle (°)	
25	25a	12.9×12.7×54.4	30.5	22.3	18.7	69.0			
	25b	12.7×12.8×49.9	31.1	23.0	17.1	70.9			
	25c	13.0×12.8×54.4	28.1	22.9	18.5	66.7			2.1
	25d	13.1×13.1×55.0	29	23.2	17.9	62.7			
	25e	13.1×13.0×55.0	30.5	22.9	18.2	64.2			
Average			29.8±1.3	22.9±0.3 (24.1%)*	18.1±0.6 (39.0%)*	66.8±3.3			
90	90a	12.7×12.7×50.5	29.2	20.1	--	38.0	2.0	31.2	
	90b	12.9×12.8×54.5	25.9	18.7	--	42.3	2.0	30.3	
	90c	13.0×12.8×54.3	26.5	18.4	--	42.5	1.8	32.2	
	90d	12.9×13.0×55.1	27.9	19.8	--	40.5	1.7	32.2	1.7
	90e	12.9×12.9×55.0	27.6	19.3	--	40.8	1.7	30.2	
Average			27.4±1.3	19.3±0.7 (27.7%)*	--	40.9±1.7	1.8± 0.1	31.2± 1.0	
Decrease (%)			8.1**	15.7**		38.8**			19.0**

*: average decrease compared to stage 1
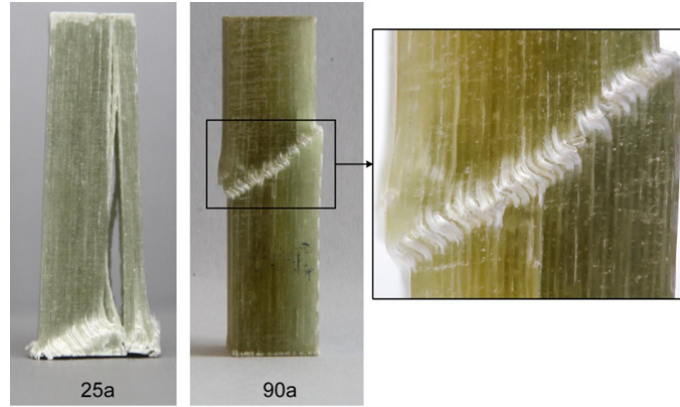
**: average decrease compared to 25°C

Fig. 4.7: *Failure mode of specimens at 25˚C (25a, splitting) and 90˚C (90a, kinking) and zoom on kink band*

4.3.4 Strain field measurements

The strain field on the surface of one specimen at each temperature was monitored by the DIC device. The strain fields along the y-axis (ε_{yy}) under three compressive loads for specimen 25a at 25°C are shown in Fig. 4.8. It can be seen from the strain field under 22.9kN and 69.0kN (failure load) that ε_{yy} was almost evenly distributed across the examined surface up to the failure load, except in the boundary parts. At the failure load, the specimen was split accompanied by a kinking failure near the boundary while the load suddenly dropped from 69.0kN to 18.8kN.
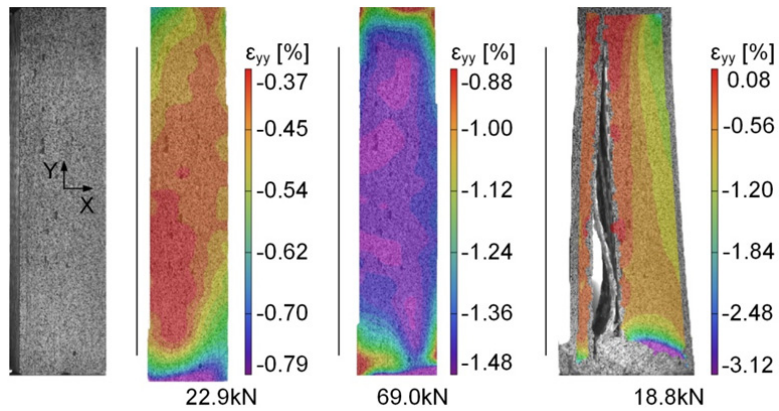

Fig. 4.8: *Axial compression strain fields of specimen 25a at 25˚C at different load levels*
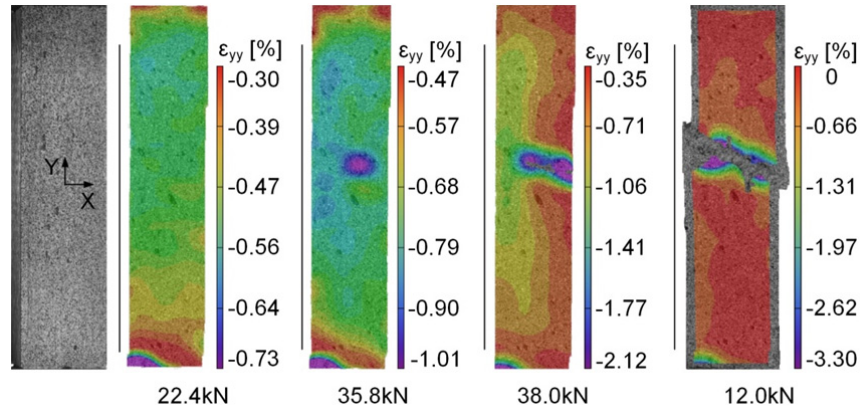
Fig. 4.9: *Axial compression strain fields of specimen 90a at 90˚C at different load levels*

For experiments conducted at 90˚C, the strain fields along the y-axis (ε_{yy}) under four load levels for specimen 90a are shown in Fig. 4.9. The compressive strains were almost evenly distributed across the examined surface up to 35.8kN. At that load, the strain was concentrated in an elliptic area at approximately 30mm from the bottom of the specimen. This strain concentration then propagated along an inclined path of approximately 31˚ to the x-axis up to the failure load of 38.0kN, at which a kink band formed across the whole cross section and the load dropped immediately to 12kN.

4.3.5 Fiber microbuckling

In order to investigate the effect of the fibers' initial waviness on the failure modes of the specimens, the increase of their lateral displacements along four lines, drawn parallel to the specimen axis and spaced at 2mm, was extracted from the DIC measurements, see Figs. 4.10 and 4.11 for 25˚C (specimen 25a) and 90˚C (specimen 90a).

As shown in Fig. 4.10, four load levels were selected to compare the lateral deformation of the four lines: 18.1kN (end of 1st linear stage), 31.4kN (during the 2nd linear stage), 55.0kN (during the 3rd linear stage) and 69.0kN (failure load). A significant curvature of the lines arose between 31.4 and 55.0kN (during the 2nd linear stage) which then increased up to the failure load, the lines however remained parallel. At the same time, fiber microbuckling developed

resulting in an increase of the global curvature. The microbuckling wavelength did not signifi-cantly change during the load increase and ranged from 3.09mm to 3.15mm at the failure load, see Table 4.2. The maximum amplitude at failure varied between 0.001 and 0.002 mm.
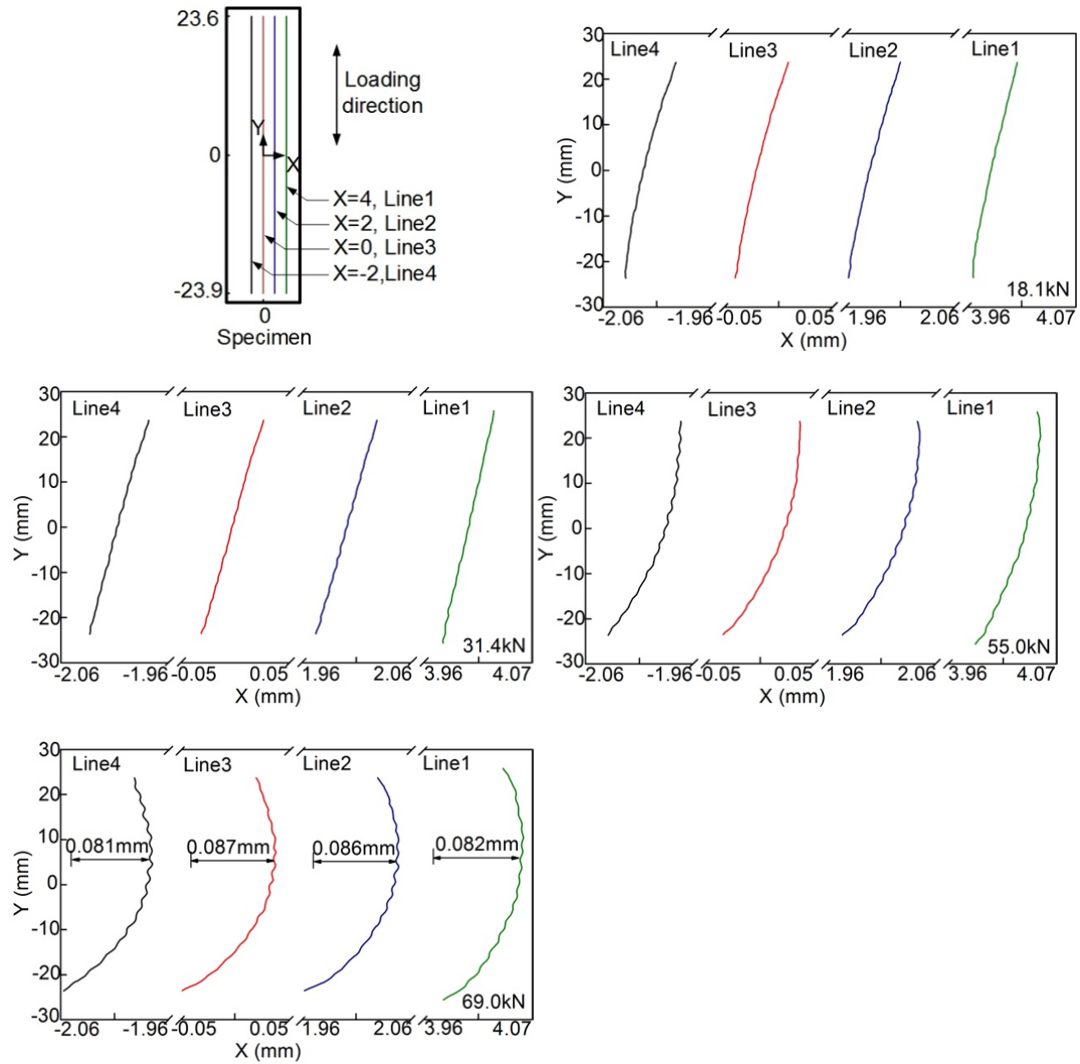

Fig. 4.10: *Displacements of Lines 1 to 4 in x-direction, along y-axis at 25°C, specimen 25a*

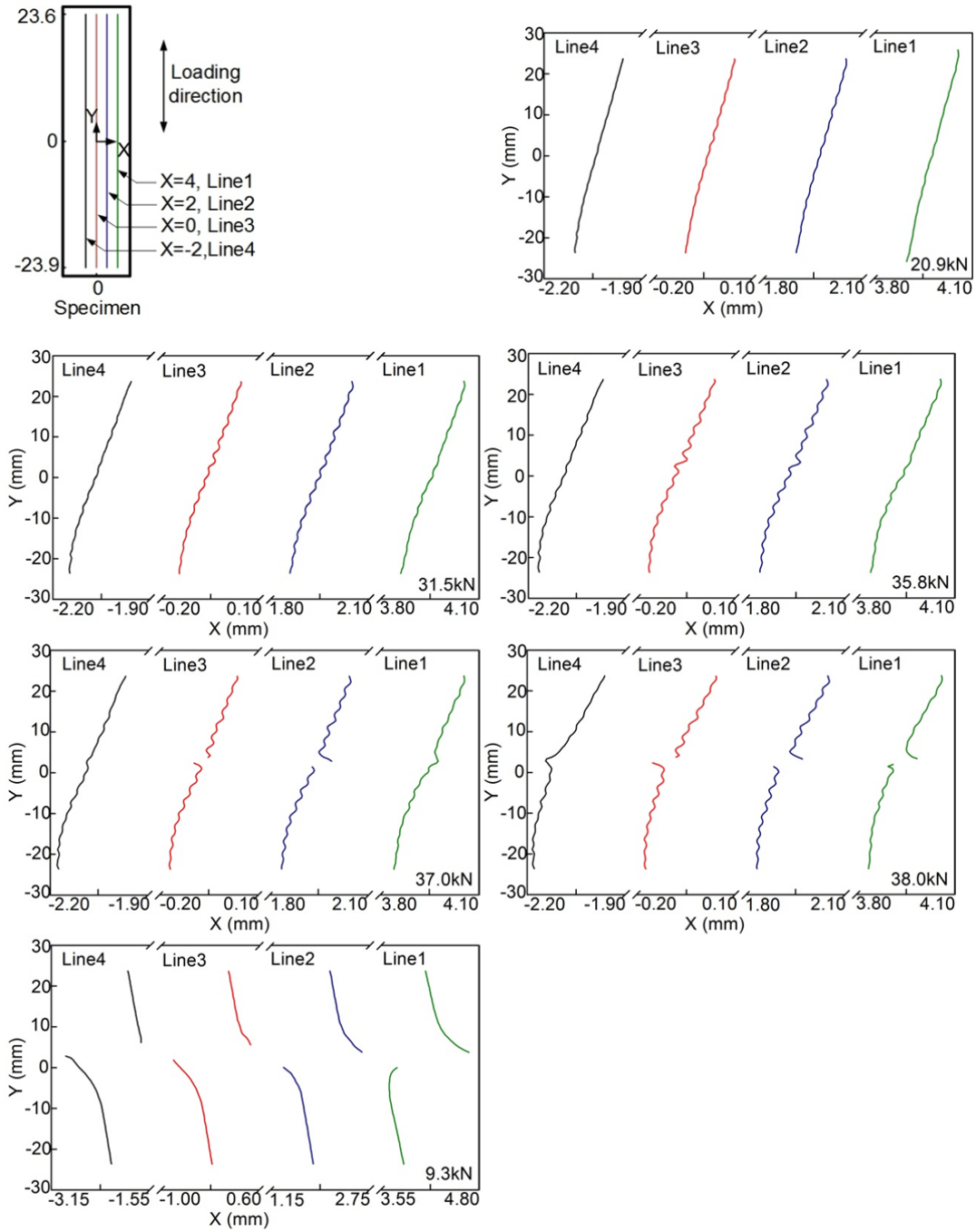*(note: the scales for x- and y-axis are different)*

62

Fig. 4.11: *Displacements of Lines 1 to 4 in x-direction, along y-axis at 90˚C, specimen 90a*

(note: the scales for x- and y-axis are different; the scale for x-axis of the graph referring to 9.3 kN differs from the scale referring to other loads)

63

Table 4.2: *Wavelengths and amplitudes of laminae at failure load (unit: mm)*

		Line 1	Line 2	Line 3	Line 4
Initial imperfection	Wavelength		3.23±0.17		
	Amplitude		0.036±0.003		
Laminae at 69kN and 25°C, specimen 25a	Wavelength	3.09±0.14	3.12±0.18	3.15±0.36	3.08±0.20
	Max. Amplitude	0.001	0.002	0.001	0.002
Laminae at 38kN and 90°C, specimen 90a	Wavelength	3.14±0.28	3.14±0.14	3.16±0.14	3.11±0.19
	Max. Amplitude	--	--	--	0.012

A different behavior was observed for the specimen examined at 90°C, see Fig. 4.11. In this case, six load levels were selected to compare the lateral deformation of the lines: 20.9kN (end of 1st linear stage), 31.5kN (during the 2nd linear stage), 35.8kN (initiation of strain concentration), 37.0kN (just before failure load), 38.0kN (failure load) and 9.3kN (post-failure load). Fiber microbuckling started already at the end of the 1st linear stage (20.9kN) and was more pronounced in the inner Lines 2 and 3 than in the outer lines. The wave amplitudes significantly increased towards the failure load while the wavelengths remained unchanged and were similar to those at 25°C, ranging from 3.11mm to 3.16mm, see Table 4.2. The global line curvatures however were less pronounced. At around 37.0kN, very close to failure, significant wave crests formed in Lines 2 and 3 at y≈3mm, the location of the subsequent kinking failure. The crests at these locations became untraceable by the DIC system at loads larger than 37.0kN due to the rapid and large deformation. Further increasing of the load also produced such a crest in Line 1 and only the deformation along Line 4 could still be measured. The post-failure pattern finally shows the kink band that developed; the fiber microbuckling was fully reversed and no longer visible.

A quantitative comparison of the maximum amplitude development of the wave crests of the four lines is shown in Fig. 4.12. At 35.8kN, the maximum amplitude of Lines 2 and 3 was already 150% higher than that of Lines 1 and 4. At failure, only the maximum amplitude of Line 4 could be measured, with a value of 0.012mm being obtained, which was around 6 times higher than that at 25°C failure.
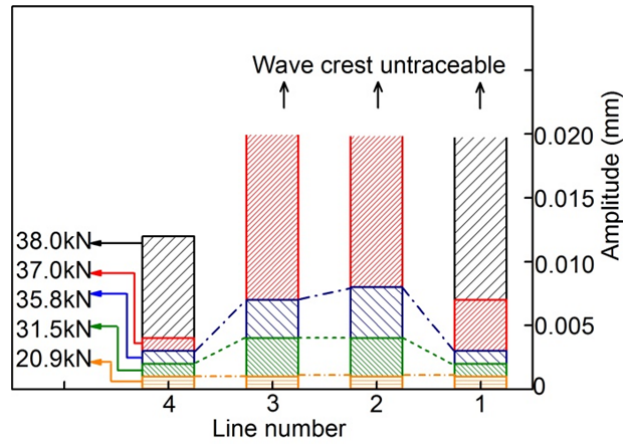
Fig. 4.12: *Maximum amplitude of fiber microbuckling of Lines 1 to 4 (see Fig. 4.11) at 90˚C, specimen 90a*

4.4 Discussion

4.4.1 Kink initiation mechanism

At both temperatures, the development of fiber microbuckling could be observed, causing the measured decrease in specimen stiffness since no further damage to the specimens was apparent. The wavelength thereby remained approximately constant up to specimen failure and corresponded to the initial imperfection - only the amplitude started increasing. At 25°C, the amplitude increased by approximately 5.6% from the average initial imperfection (0.036mm) up to specimen failure, see Table 4.2, which occurred through splitting, without the development of a kink band.

At 90°C, a concentration of compressive strains and an increase of the amplitude could be observed at one specific location just above the specimen's mid-height at around 95% of the failure load. In this area, the fibers started developing non-linear second-order deformations – at constant wavelength – with an amplitude higher than the initial imperfection, and the associated stiffness decrease caused the observed strain concentration. The area surrounding the fibers seemed to exhibit less stiffness against buckling at this location than in other resin regions, which may have been caused by voids or other local defects. Subsequent fiber microbuckling and local matrix failure initiated the kink band development.

4.4.2 Kink band development

The kink band development in specimen 90a at 90°C, above 35.8kN (see Fig. 4.9), was further analyzed. In the DIC measurements, the band was indicated by grey areas where the targets could no longer be followed due to the rapid and large local deformations, see Fig. 4.9 at 38.0kN. The first kinking occurred locally at 36.1kN, as shown in Fig. 4.13. With increasing load, the kink band started developing and propagated from this location stepwise in alternating horizontal and inclined segments. Since the ultimate compression strain of the matrix was exceeded, the presence of horizontal segments can be explained by pure matrix compression failure, and the presence of inclined segments by combined matrix compression-shear failure.
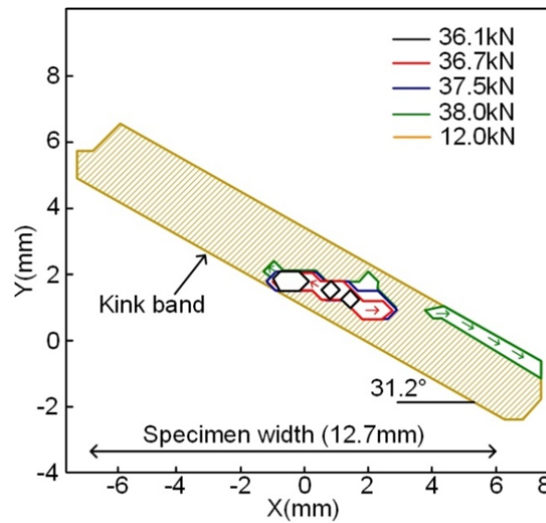

Fig. 4.13: *Paths of compressive kinking propagation at 90°C, specimen 90a*

At failure initiation (38.0kN in Fig. 4.9), the band spread over approximately 60% of the specimen width. During failure, the band extended through the whole specimen width and approximately doubled its width. The band now formed a clear angle of 31.2° and was no longer composed of inclined and horizontal segments. The microbuckling in the remaining parts completely reversed after failure.

4.5 Conclusions

The compressive mechanical behavior of non-slender glass fiber-reinforced epoxy prismatic specimens at temperatures up to 90°C was investigated in this work in order to reveal the mechanisms causing kink failure. The strain field development on a surface perpendicular to the laminae was continuously monitored by a digital image correlation device to observe and derive the failure mechanisms. The following conclusions were drawn:

1) Kinking failure could only be observed at elevated temperatures, when approaching the glass transition temperature of the matrix.

2) The kink initiation mechanism could be clearly mapped. In relation to the initial waviness of the fibers the wave amplitudes started increasing with increasing load at both temperatures; the wavelength did not change. At elevated temperature, the wave amplitude then disproportionally increased at one specific location up to fiber microbuckling and surrounding matrix failure. At ambient temperature, this stage was not reached since splitting failure occurred first.

3) Kink band development could be clearly observed. Starting from the location of kink initiation at elevated temperature, the kink band rapidly propagated through alternating horizontal and inclined segments, leading to an overall inclined kink band of 31° on average. The horizontal and inclined propagations were attributed to alternating matrix compression and compression-shear failures. The kink band width doubled during this propagation from approximately three times to six times the average wavelength of the initial imperfection.

67

References

1. Harvey, A. O. J., Analysis of 30 years of pavement temperatures using the enhanced integrated climate model (EICM), report for the California Department of transportation, 2004.

2. Schultheisz, C.R., and Waas, A.M., Compressive failure of composites, Part I: testing and micromechanical theories, Prog. Aerospace Sci, Volume 32, 1996, pp. 1-42.

3. Gutkin, R., Pinho, S.T., Robinson, P., and Curtis, P.T., A finite fracture mechanics formulation to predict fibre kinking and splitting in CFRP under combined longitudinal compression and in-plane shear, Mechanics of materials, Volume 43, 2011, pp. 730-739.

4. Lee, S.H., and Waas, A.M., Compressive response and failure of fiber reinforced unidirectional composites, International Journal of Fracture, Volume 100, 1999, pp. 275-306.

5. Rosen, B.W., Mechanics of composite strengthening, Fiber composite materials, American society for metals, Ohio, 1964.

6. Evans, A.G., and Adler, W.F., Kinking as a mode of structural degradation in carbon fiber composites, Acta Metallurgica, Volume 26, 1978, pp. 725-738.

7. Lankford, J., Compressive failure of fiber-reinforced composites: buckling, kinking and the role of interphase, Journal of material science, Volume 30, 1995, pp. 4343-4348.

8. Dobb, M.G., Johnson, D.J., and Park, C.R., Compressional behavior of carbon fibers, Journal of materials science, Volume 25, 1990, pp. 829-834.

9. Berg, C.A., and Salama, M., Fatigue of graphite fiber-reinforced epoxy in compression, Fiber Science and Technology, Volume 6, 1973, pp. 79-118.

10. Moran, P.M., Liu X.H., and Shih, C.F., Kink band formation and band broadening in fiber compression under compressive loading, Acta Metallurgica et Materialia, Volume 43, 1995, pp.2943-2958.

11. Volger, T.J., and Kyriakides, S. On the initiation and growth of kink bands in fiber composites: Part I. experiments, International Journal of Solids and Structures, Volume 38, 2001, pp. 2639-2651.

12. Gutkin, R., Pinho, S.T., Robinson, P. and Curtis, P.T., On the transition from shear-driven fibre compressive failure to fibre kinking in notched CFRP laminates under longitudinal compression, Composites Science and Technology, Volume 70, 2010, pp. 1223-1231.

13. Weaver, C.W., and Williams, J.G., Deformation of a carbon-epoxy composite under hydrostatic pressure, Journal of material science, Volume 10, 1975, pp. 1323-1333.

14. Wronski, A.S., and Parry, T.V., Compressive failure and kinking in uniaxially aligned glass-resin composite under superposed hydrostatic pressure, Journal of material science, Volume 17, 1982, pp. 3656-3662.

15. Grape, J.A., and Gupta, V., The effect of temperature on the strength and failure mechanisms of a woven carbon/polyimide laminate under compression, Mechanics of Materials, Volume 30, 1998, pp. 165-180.

16. Bazhenov, S.L., and Kozey, V.V., Compression fracture of unidirectional carbon fibre-reinforced plastics, Journal of materials science, Volume 26, 1991, pp. 6764-6776.

17. Kyriakides, S, Arseculeratne, R. Perry, E.J., and Liechti, K.M., On the compressive failure of fiber reinforced composites, International journal of solids structures, Volume 32, 1995, pp. 689-738.

18. Hsiao, H.M., and Daniel, I.M., Effect of fiber waviness on stiffness and strength reduction of unidirectional composites under compressive loading, Composite science and technology, Volume 56, 1996, pp. 581-593.

19. Feld, N., Allix, O., Baranger, E., and Guimard, J.M., Micro-mechanical prediction of UD laminates behavior under combined compression up to failure: influence of matrix degradation, Journal of composite materials, Volume 45, 2011, pp.2317-2333.

20. Hancox, N.L., The compression strength of unidirectional carbon fibre reinforced plastics, Journal of Materials Science, Volume 10, 1975, pp. 234-242.

21. Suter-kunststoffe AG, Faserverbundwerkstoffe, Edition 2012-08, Schweiz.

22. ASTM D695-10, Standard test method for compressive properties of rigid plastics, 2010.

23. ASTM, E1640-09, Standard test method for assignment of the glass transition temperature by dynamic mechanical analysis, 2009.

5 Effect of temperature on kinking failure mode of non-slender glass fiber-reinforced polymer specimens

Reference Detail

Sun, W., Vassilopoulos, A.P., and Keller T., Effect of temperature on kinking failure mode of non-slender glass fiber-reinforced polymer specimens, submitted in April, 2015.

5.1 Introduction

Compared to the tensile strength of fiber-reinforced polymer (FRP) materials, the compressive strength exhibits more scatter due to fiber misalignments and initial imperfections caused during fabrication. Furthermore, the compressive material properties of FRP composites are sensitive to temperature elevations usually occurring in engineering applications, either in hot environments [1], or when incidents such as fire [2] occur.

Fiber failure, splitting, kinking, buckling, and the combinations of the former are the most commonly observed failure modes associated with the compressive loading of FRP composite materials. Fiber failure is a common failure mode of weak-in-compression fibers, such as aramid fibers, however it is not observed as often when stronger-in-compression carbon or glass fibers are used [3]. Delamination and splitting are typical compressive failure modes of composites with low interlaminar or interfacial shear strength, e.g. carbon fiber-reinforced polymers (CFRPs), and are accompanied by crack propagation, inside the matrix or at the interface, along the loading direction [4]. Kinking is a failure mode in which one part of the material is displaced relatively to another along an inclined path with respect to the loading direction. Kinking failure has been observed in both CFRP and glass fiber-reinforced polymer (GFRP) composites [5]. Buckling resembles bending or lateral deflection under

axial compressive loads [6] and is a common failure mode for slender CFRP and GFRP specimens under axial compressive loads.

Kinking failure was first experimentally investigated by Rosen [7]. The microbuckling of fibers was observed during the cooling of GFRP specimens from curing temperature to room temperature. Microbuckling was initiated by the shrinkage of the resin, which induced compressive stresses in the fibers. In later studies [8-10], kinking was assumed to be a result of fiber microbuckling, based on the reported coexistence of microbuckling and kinking in CFRP laminates. Other studies, e.g. compressive experiments on CFRP specimens [11-13], focused on the kinking band propagation and broadening, providing only limited information about the factors leading to kink initiation. Contradictory conclusions were presented by Weaver and Williams [14], and Wronski and Parry [15] as neither observed any significant microbuckling before or after the kinking failure of examined GFRP specimens, and they therefore concluded that there is no relationship between microbuckling and kinking.

Temperature and specimen slenderness may affect the compressive failure mode and strength of composites. A shift from splitting to kinking failure at elevated temperatures was observed in [16-17] and was attributed to the softening of the matrix and increase of the shear interlaminar stresses. However, limited experimental evidence was provided in [16] regarding the formation of microbuckling due to shear interlaminar stresses. The failure mode of GFRP specimens with a slenderness ratio of 60 during temperature elevation was studied in [18]. It was found that the failure mode changed from buckling at ambient temperatures to kinking at 220°C, at which the rubbery state of the examined matrix was reached. A temperature-dependent non-dimensional slenderness ratio was proposed to describe the effects of both geometry and matrix softening during temperature elevation on the failure mode. Compressive experiments on short circular GFRP specimens (maximum length-to-diameter ratio of 2.0) were performed in [19]. It was found that the compressive strength of the specimens decreased sharply during the glass transition of the matrix, while the failure mode was fiber failure independent of the temperature range and material states.

The failure mode may further be affected by material imperfections, e.g. fiber waviness and voids. Typical wavelengths of CFRP prepregs were found to be between 2.1mm and 5.6mm [20]. With the increase of fiber waviness the width of the kink band increased by as much as 45% [21], while on the contrary the compressive strength decreased by up to 75%, as reported in [22]. As shown in [23], the failure mode of low-void-content materials was kinking while that of materials with a higher percentage of voids was splitting. Furthermore, the fiber volume fraction may influence the failure mode. Both kinking and splitting were observed in GFRP specimens with fiber volume fractions above 30% and splitting was the prevailing failure mode with lower fiber volume fractions [5].

The aforementioned works mainly focused on the investigation of kink band propagation and the effect of temperature and material imperfections on the failure modes of FRP composites. Even though certain phenomena, e.g. the coexistence of microbuckling and kinking, were observed, direct experimental evidence of the effect of microbuckling on kink initiation is still not provided in literature. Moreover, the failure modes of non-slender GFRP specimens under compression at elevated temperatures were not thoroughly investigated.

In a previous work of the authors [24], the failure mode of non-slender GFRP prismatic specimens was investigated at 23°C and 90°C (the onset of glass transition of the resin). Kinking failure was observed at 90°C and it was experimentally demonstrated that fiber microbuckling was responsible for kink initiation at that temperature and degree of slenderness. The current work investigates the kink behavior of the same type of GFRP prismatic specimens with different lengths (slenderness) and fiber volume fractions at elevated temperatures up to 125°C, at which the resin is in the rubbery state. The experimental results, including surface strain and lateral displacement measurements obtained by digital image correlation (DIC), confirmed the results obtained in [24] and showed, more generally, that fiber microbuckling led to kink initiation and kink band formation, either before kinking failure at the onset of glass transition or during the post-failure stage after buckling at higher temperatures.

5.2 Experimental work

5.2.1 Material characterization

Glass fiber-reinforced polymer (GFRP) composites, a material typically used in civil engineering applications, were selected in this work. The matrix is a thixotropic bi-component polymer from Swiss Composite AG [25], composed of type-L epoxy base resin and EPH 161 hardener; the resin to hardener mixing ratio is 4:1. This epoxy has a low viscosity and is free of fillers, which is ideal for impregnating glass fibers. The polymer is reinforced by unidirectional E-glass fiber fabrics (EC 9-68) from Swiss Composite AG, having an area density of 425g/m^2 and layer thickness of 0.45mm [25].

Two GFRP plates were fabricated by hand-layup achieving a fiber volume fraction of 44% and 31% respectively as determined by burn-off experiments. The two plates were left at ambient temperature for 48 hours and were then post-cured at 100°C for 72 hours to complete the curing. Three groups of 18 specimens each with nominal dimensions of 12.7x12.7x35 mm^3, 12.7x12.7x50 mm^3, and 12.7x12.7x75 mm^3, according to ASTM D695-10 [26], were cut from the high fiber volume fraction

73

plate. Two groups of six specimens each with nominal dimensions of 12.7x12.7x35 mm^3 and 12.7x12.7x50 mm^3 were cut from the low fiber volume fraction plate. Each group of the high fiber volume fraction specimens was examined at temperatures of 25, 90, 100, 105, 115, and 125°C with three specimens at each temperature. Specimens with low fiber volume fraction were only examined at 25°C and 90°C. The specimen series were labeled accordingly by using a six-digit encoding system. The first two digits denote the specimen length (35, 50 or 75 mm), the third the fiber volume

Table 5.1: *Compressive results at temperatures from 25 to 125°C*

Specimen				Specimen initial stiffness (kN/mm)	Peak load (kN)	Kink band	
Fiber volume fraction	Length (mm)	Series number	Temperature (°C)			Width (mm)	Angle (°)
High	35	35H025	25	35.9±2.0	64.1±2.8		
		35H090	90	35.6±1.5	46.2±4.3	1.9±0.2	28.8±2.2
		35H100	100	32.9±1.0	33.2±6.5	1.9±0.2	29.5±2.5
		35H115	105	26.8±2.2	10.6±1.8	6±0.9	39.7±0.6
		35H115	115	22.5±1.2	5.1±1.2	6.5±0.5	42.2±0.3
		35H125	125	16.4±1.1	4±0.5	6.1±0.1	42.5±0.9
	55	55H025	25	30.0±1.6	66.9±4.0		
		55H090	90	27.2±1.7	41.0±2.4	1.9±0.1	31.2±1.0
		55H100	100	26.0±1.1	23.1±3.5	2.3±0.6	33.3±1.5
		55H105	105	23.1±1.2	6.8±0.8	5.9±0.5	40.4±1.7
		55H115	115	18.0±1.8	4.7±0.6	6.2±0.3	40.4±1.7
		55H125	125	15.0±1.2	4.2±0.2	5.8±0.3	41.8±0.4
	75	75H025	25	26.9±0.9	61.6±1.6		
		75H090	90	23.8±0.9	40.9±0.4	2.4±0.3	29.5±2.5
		75H100	100	22.9±0.9	25.1±2.5	1.9±0.4	33.7±1.2
		75H105	105	18.2±1.2	5.5±0.9	7.7±0.6	41.7±0.6
		75H115	115	15.4±1.2	4.1±0.2	7.8±0.6	43.0±1.0
		75H125	125	11.8±1.3	3.9±0.2	7.2±0.3	43.3±2.3
Low	35	35L025	25	30.5±1.9	54.6±3.1		
		35L090	90	28.5±2.0	32.2±1.1	2.0±0.1	26.6±0.5
	55	55L025	25	26.3±1.0	46.6±6.0		
		55L090	90	24.2±0.6	34.5±0.5	1.7±0.3	29.0±0.7

fraction (H for high and L for low fiber volume fraction), while the last three digits represent the temperature (between 25 and 125°C), see Table 5.1. An additional digit was added to this encoding system referring to the specimen number within the same series (a, b, or c) examined at the same temperature.

To investigate the material's microstructure, a specimen with dimensions 13x13x13 mm, cut from the high fiber volume fraction plate, was scanned using an optical microscope. The scanned surface was perpendicular to the lamina plane, see Fig. 5.1a. As shown in Fig. 5.1b and 5.1c, the rovings were not perfectly straight and exhibited initial imperfections, i.e. initial waviness and voids. Measured average wavelengths and amplitudes of the initial waviness were 3.23±0.17mm and 0.036±0.003mm respectively, see Table 5.2 (data from nine measurements). Voids were observed between and inside the rovings, as shown in Fig. 5.1b and 5.1c. The former were created by air trapped in the epoxy and the latter caused by insufficient impregnation of individual fibers during the hand lay-up fabrication.

Table 5.2: *Wavelengths and amplitudes before loading and at peak load*

		Line 1	Line 2	Line 3	Line 4	Line 5
Initial imperfection H-plate	Wavelength [1]	3.23±0.17				
(mm)	Amplitude [1]	0.036±0.003				
Specimen 55H100a at 100°C and peak load (25.6 kN) (mm)	Wavelength [2]	3.12±0.09	3.07±0.06	3.07±0.07	3.10±0.13	3.08±0.06
	Increase of amplitude [2]	0.038	--	--	--	0.021

[1] from microscopy, values independent of Line number

[2] from DIC, values for Lines 1-5, see Fig. 5.16

The mechanical response of the GFRP specimens was assumed to be affected by the decrease of the modulus of the matrix during temperature elevation. The storage modulus-temperature relationship of the epoxy matrix was thus first measured via Dynamic Mechanical Analysis (DMA). Specimens with dimensions 53x10x3 mm^3 were prepared according to ASTM E1640-09 [27] and cured at ambient temperature for 48 hours and then post-cured at 90°C for 72 hours to obtain full curing. The typical three states can be recognized from the obtained storage modulus-temperature curve, see Fig. 5.2: the glassy state until the glass transition onset ($T_{g,onset}$) estimated at 93°C (the tangent line inter-

section of the glassy state and the glass transition region), the glass transition from the $T_{g,onset}$ tempe-rature to 107°C and the rubbery state for temperatures above 107°C. The storage modulus decreased by 19% from ambient temperature to $T_{g,onset}$ temperature and by 95% at the end of glass transition, at around 107°C.
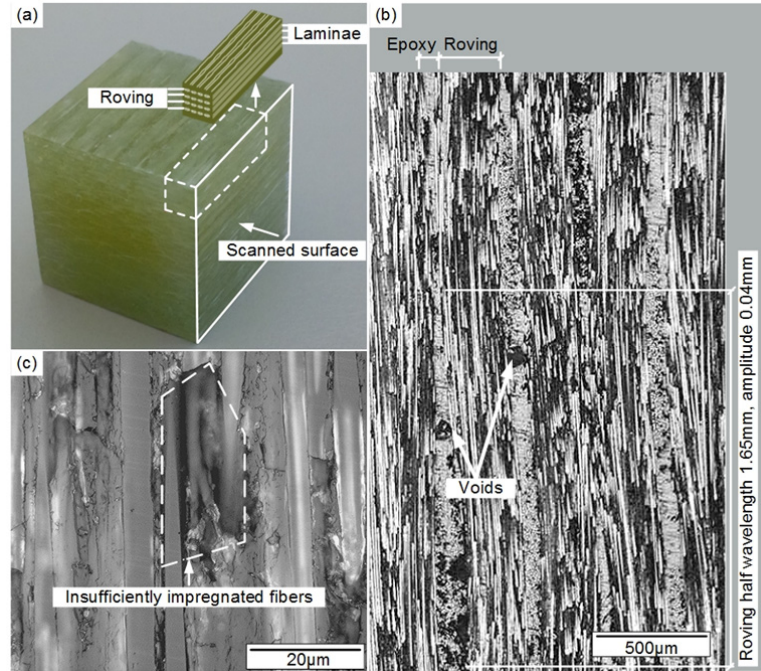

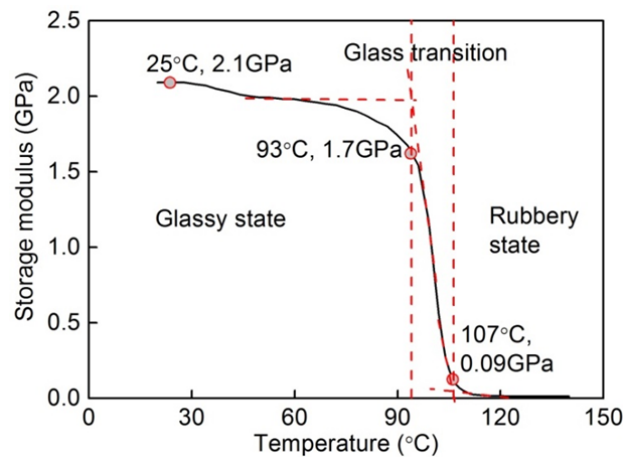**Fig. 5.1:** *(a) Specimen for optical microscopy, (b) fiber waviness and voids between rovings, (c) voids inside roving*

Fig.5.2: *Storage modulus-temperature relationship of epoxy matrix*

5.2.2 Experimental set-up and instrumentation

The compressive experiments were performed using an INSTRON 8800 servohydraulic machine with a displacement rate of 0.5mm/min. The movement of the loading head was recorded by the machine and represented the axial specimen displacement (shortening). The specimens were compressed by applying tensile loading through a tension-compression transfer fixture. As shown in Fig. 5.3, four steel plates with dimensions of $160 \times 160 \times 40 mm^3$ were assembled vertically and connected by steel bars. Plates 1 and 3 connected to the upper grips were moving up and thus applying compression to the specimens, which were placed between plates 2 and 3.
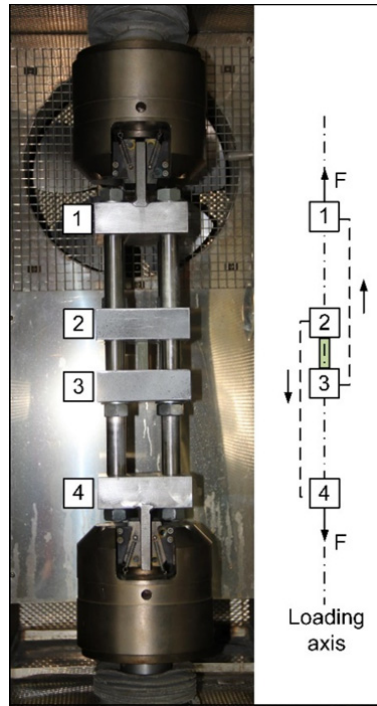
Fig. 5.3: *Tension-compression transfer fixture (specimen between plates 2 and 3)*

The strain field on the specimen surface perpendicular to the laminae, in which kinking was expected, was measured by a digital image correlation (DIC) system (VIC-3D from Correlated Solutions), as shown in Fig. 5.4. The DIC system consisted of two camera lenses (Pentax lenses with a focal length of 25mm and an aperture of 1.4) with a distance of 415mm to the specimen, a signal converter, two lighting panels and a computer. A speckle pattern consisting of tiny black dots was

sprayed on top of a white layer painted on the specimen surface. The speckle pattern displacements were measured by comparing the reference position at 0 kN-load to the position of the speckles at a certain load level; the measurement frequency was 1 Hz. The accuracy of the displacement measurements was ±0.0017mm. Strains were derived from the displacements by the Lagrange strain tensor. The accuracy of the strain estimations was ±0.0015%.
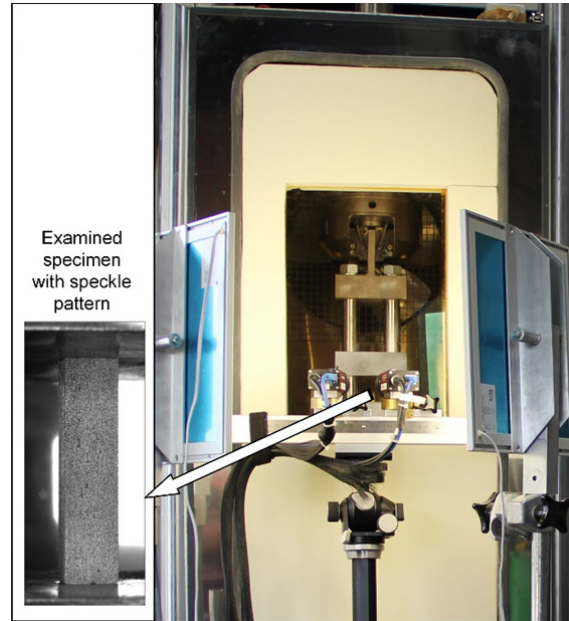

Fig. 5.4: Experimental set-up and specimen with speckle pattern

The fixture and specimens were placed inside a climatic chamber in order to reach the target experimental temperature before the compression loading was applied. To assure a uniform temperature distribution in the specimens, a supplementary specimen was used to monitor the through-thickness temperature distribution by two Pt100 thermoresistances at two positions up to the target temperature, in the center (T_1) and on the surface (T_2), both at mid-height. The thermoresistance at position T_1 was enclosed in the specimen by drilling a hole that was subsequently sealed using the same epoxy resin. The results, shown in Fig. 5.5, reveal that the temperature elevation of the specimen significantly leveled off after a rapid increase and a homogeneous temperature was reached throughout the specimen volume. The maximum measured temperature difference (T_1-T_2) at the target temperatures ranging from 90°C to 125°C was 0.7°C after 2800s. The compressive experiments were therefore carried out between 2800s and 3045s where the temperature gradient was negligible.
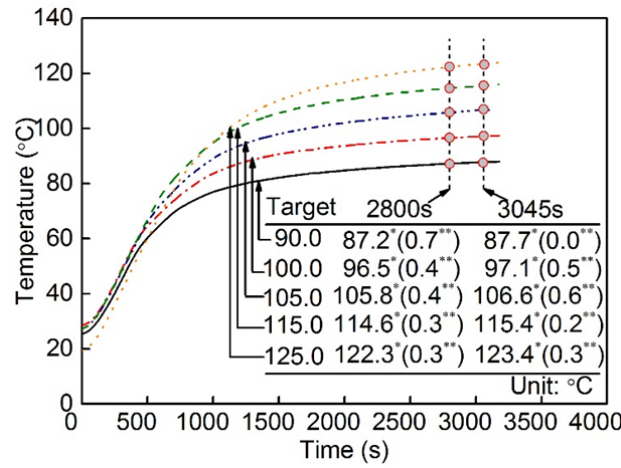
Fig. 5.5: *Temperature gradient development through specimen (*=T_1, **=T_1-T_2)*

5.3 Experimental results

5.3.1 Load-axial displacement responses

The load-axial displacement responses for the 55H series specimens loaded at temperatures ranging from 25°C to 125°C are shown in Fig. 5.6. All the curves exhibited approximately linear behaviors up to their peak loads. After the peak load, a much more steady decrease of the load with the further increase of the axial displacement was observed at temperatures above 100oC than that at lower temperatures where the decrease was much more abrupt. Specimens from the other four series (35H, 75H, 35L and 55L) showed similar load-axial displacement responses to those of the 55H series.

The comparison of the stiffness at the initial linear stage and the peak loads of the five specimen series at temperatures up to 125°C are shown in Fig. 5.7a and 5.7b respectively (standard deviations obtained from three specimen measurements are also shown). Independent of temperature and state, the stiffness was lower at longer lengths and lower fiber volume fractions. The stiffness of all series decreased moderately with increasing temperature until 90°C and then dropped sharply for higher temperatures. The effect of specimen length on peak load was significantly lower than the effect on stiffness and disappeared at the rubbery state. The effect of fiber volume fraction on peak load, however, was more pronounced, similar to that on stiffness. The peak loads decreased much more until 90°C compared to stiffness and then also dropped sharply at the glass transition to almost zero

79

at the rubbery state. Both curves, for stiffness and peak load, followed a similar trend as that obtained from DMA material characterization, see Fig. 5.5.
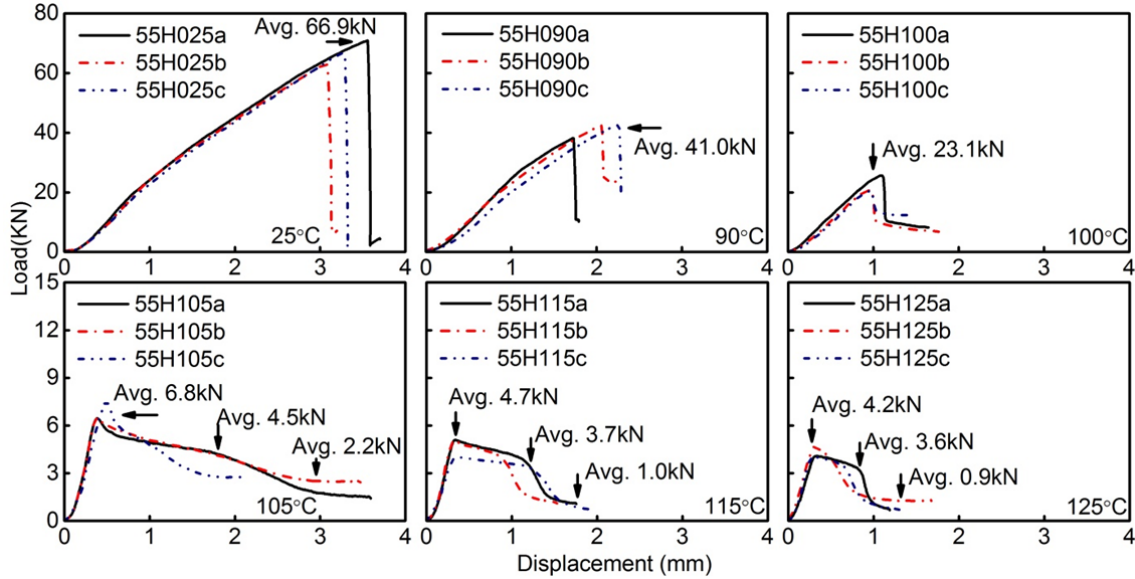

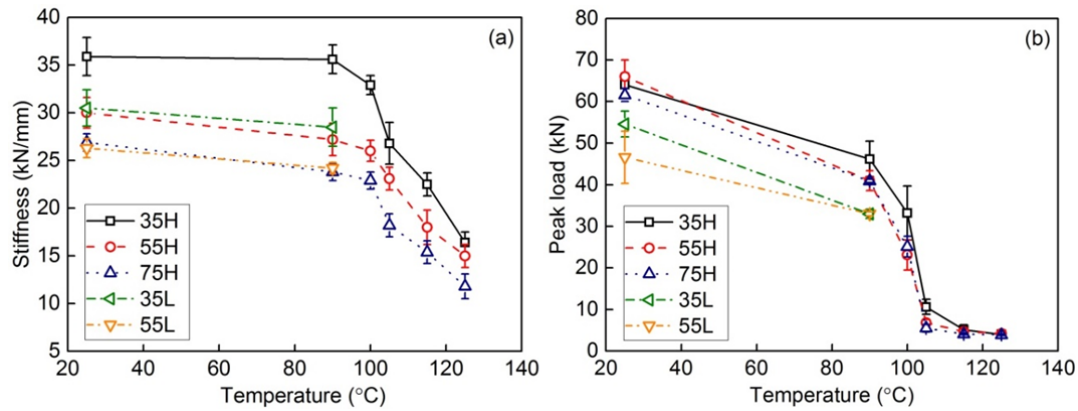**Fig. 5.6:** *Load-axial displacement curves of 55H series specimens with increasing temperature*

Fig. 5.7: *Decrease of initial stiffness and peak load of 35H, 55H, 75H, 35L and 55L series with increasing temperature*

5.3.2 Failure modes

The failure modes were independent of specimen length and fiber volume fraction. Three different failure modes could be observed and attributed to different temperature ranges and corresponding material states. Specimens at 25°C, at the glassy state, failed due to splitting between the laminae

along the specimen length, followed by fiber kinking near the boundary, as shown in Fig. 5.8. A different failure mode was exhibited by specimens loaded at 90°C and 100°C, at the glass transition. In this case, a kinking failure mode was observed in the middle part or near one edge of the specimens at the peak load. Specimens at higher temperatures, up to 125°C at the rubbery state, buckled before or at the peak load and kinking was observed during the post-buckling stage with decreasing load.
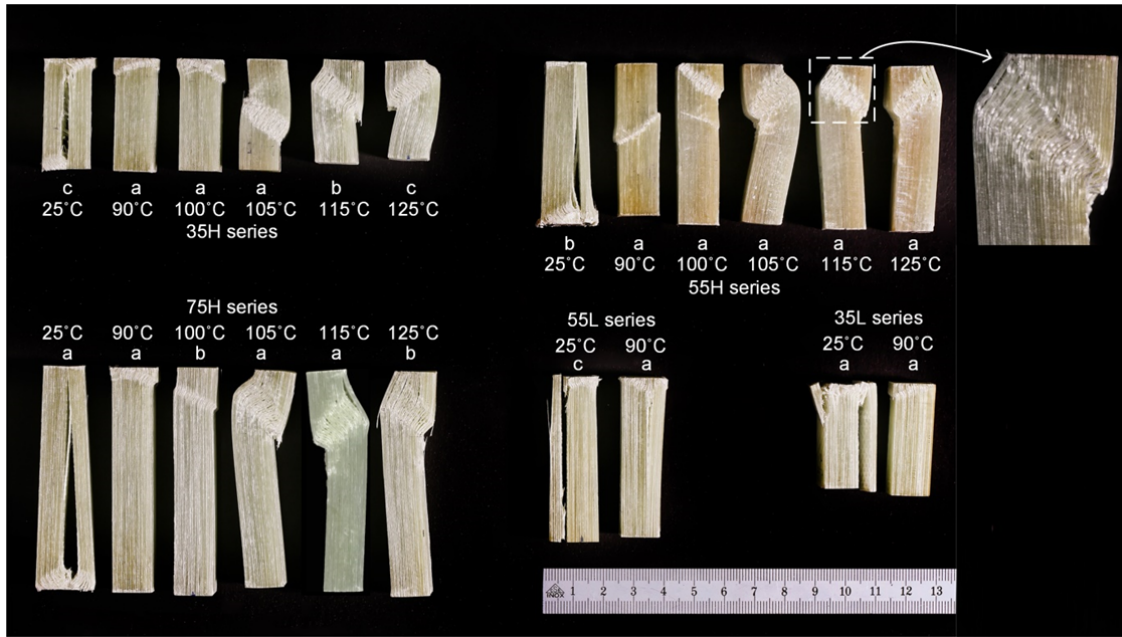

Fig. 5.8: *Failure modes of 35H, 55H, 75H, 35L and 55L series at temperatures up to 125°C*

The measured kink band widths and kink band angles of all series as a function of temperature are shown in Fig. 5.9a and 5.9b respectively. The kink band was narrow and almost constant (around 2 mm) up to 100°C and was thus in the range of the initial waviness of the fibers. The width then sharply increased and approximately tripled at the glass transition state up to 105°C. The width then again remained almost constant at the rubbery state and was around twice the wavelength of the initial imperfections. The specimen length had a clear effect only at the rubbery state where the highest length produced a significantly wider band. Independent of temperature, delamination between the laminae occurred through the band thickness, see Fig. 5.8; the fibers, however, did not break.

81

The dependency of the kink band angle on temperature followed a similar trend as for the band width. A moderate increase was observed up to 100°C at around 30°, followed by a sharp rise at glass transition up to a plateau at around 42° at the rubbery state. A clear and consistent effect of specimen length on kink band angle could not be derived from the results.
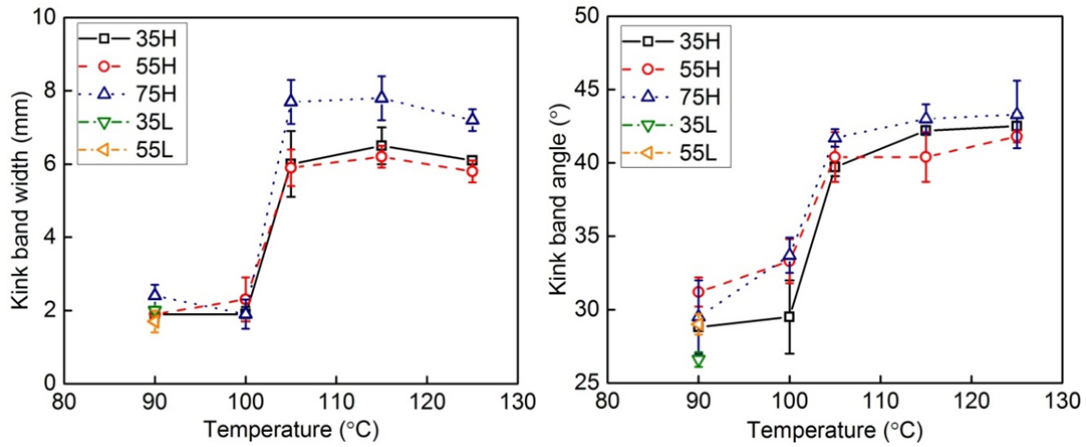

Fig. 5.9: *Increase of kink band width and kink band angle of 35H, 55H, 75H, 35L and 55L series with increasing temperature*

5.3.3 Strain field measurements

The axial compressive and shear strain fields obtained from DIC on 55H series specimens at the different temperatures are shown in Figs. 5.10-5.11 (kinking at peak load) and Figs. 5.12-5.14 (kinking at post-peak load) and are addressed first. The effects of specimen length and fiber volume fraction are then discussed.

The compressive strain (ε_{yy}) and shear strain (ε_{xy}) fields during the loading of specimens 55H090a and 55H100a at 90°C and 100°C respectively are shown in Figs. 5.10 and 5.11. In these two cases, the compressive strains were almost evenly distributed across the examined surface up to a certain load, 35.8kN at 90°C and 25.1kN at 100°C (except at the upper and lower edges). At those loads, compressive strain concentrations were observed in an elliptic area just above the specimens' midheights at 90°C and at two locations at 100°C as indicated by arrows in Fig. 5.11. At 90°C, the compressive strain concentration propagated along an inclined path from 35.8kN to the peak load of 38.0kN and was followed by a kink band formation along this path at the peak load. The kink band could be clearly captured after the sharp drop of the load to 12.0 kN and is indicated by the grey

areas where the DIC targets could no longer be followed by the cameras due to the rapid and large local displacements. At 100°C, the compressive strain concentration propagated from location 1; the kink band developed at the peak load and could again be clearly seen after the sudden load drop to 13.1kN. The coincidence of the locations of maximum compressive strain concentrations and the subsequent kink bands is not so evident for the locations of the shear strain concentrations and kink bands. At 90°C, the maximum shear strains were more or less evenly distributed along the upper three quarters of the specimens and did not change significantly up to the peak load. Only at the peak load was a shear stress concentration observable at the right edge of the subsequent kink band. At 100°C, the maximum shear strains were observed at specimen mid-height up to the peak load. However, higher shear strains were also present at the location of the subsequent kink band.
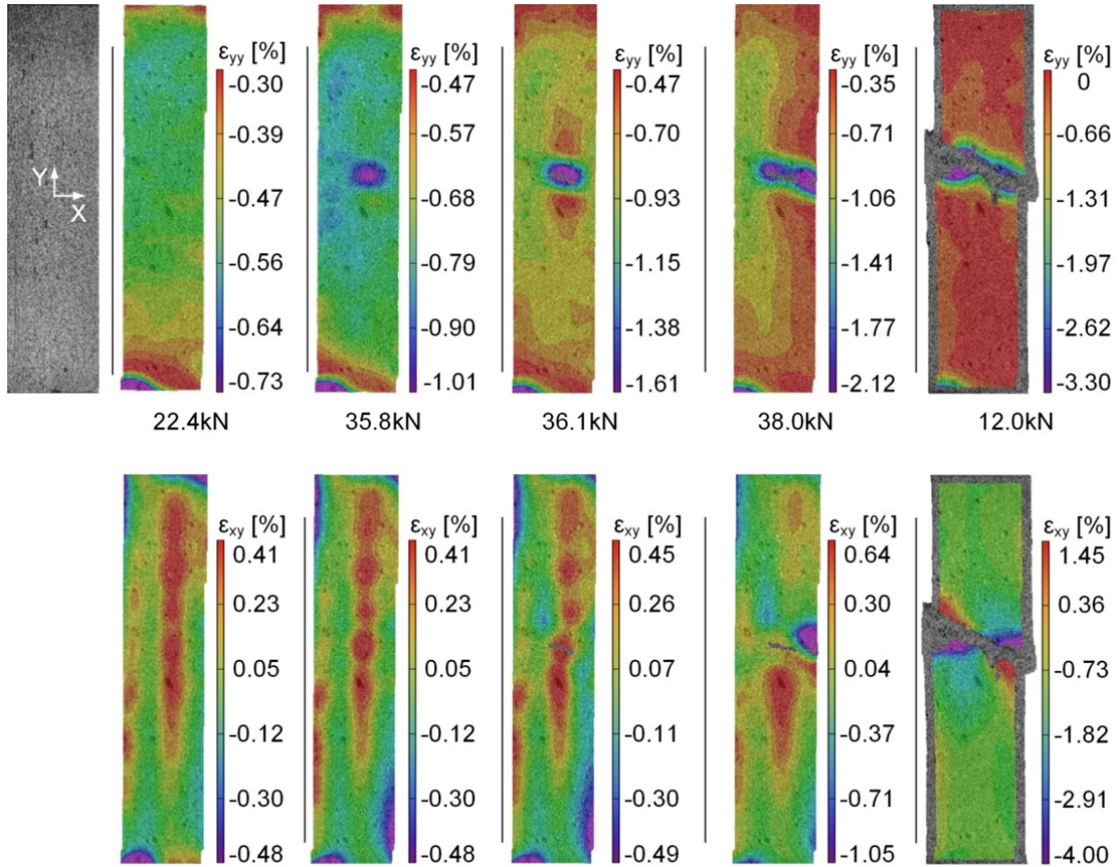

Fig. 5.10: *Axial compressive and shear strain fields on specimen 55H090a at 90°C and different load levels*
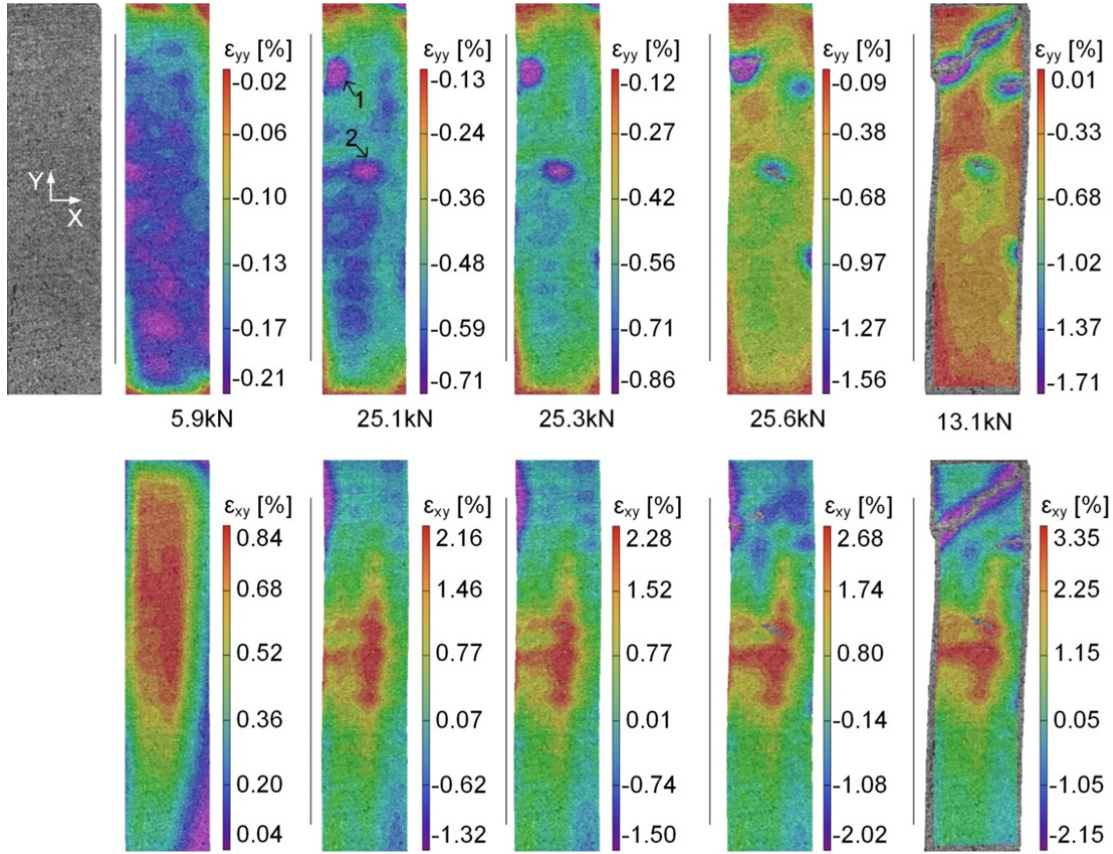
Fig. 5.11: *Axial compressive and shear strain fields on specimen 55H100a at 100˚C and different load levels*

At higher temperatures, where kinking occurred in the post-peak phase at much lower compressive loads, the coincidence of locations of maximum shear strain concentrations and subsequent kink bands was much better than at lower temperatures and also much better than between locations of maximum compressive strains and kink bands. In fact, the specimens at 105, 115 and 125°C buckled at peak load, see Figs. 5.12-5.14. Two shear strain concentration bands then formed at the two inflection points of the buckling shapes. These bands were located almost perpendicular to the curved specimen axis. In the post-peak phase, some of the DIC targets could no longer be traced and (grey) strips appeared at these locations, running parallel to the specimen axis within these bands. At 105°C, first three strips appeared at around 4.0kN, at 115°C five strips at 2.6kN and at 125°C four strips at 3.1kN. The number of parallel strips then increased and the loads significantly dropped further (see Fig. 5.6) until kink band formation occurred. The kink band widths almost corresponded to the widths of the shear concentration bands. The compressive strain fields did not show similar clear concentrations across the widths at the locations of the subsequent kink bands. A concentration

occurred at the location of the maximum bending moment on the compression side, which coincided with the lower edge of the subsequent kink band, see Fig. 5.12.
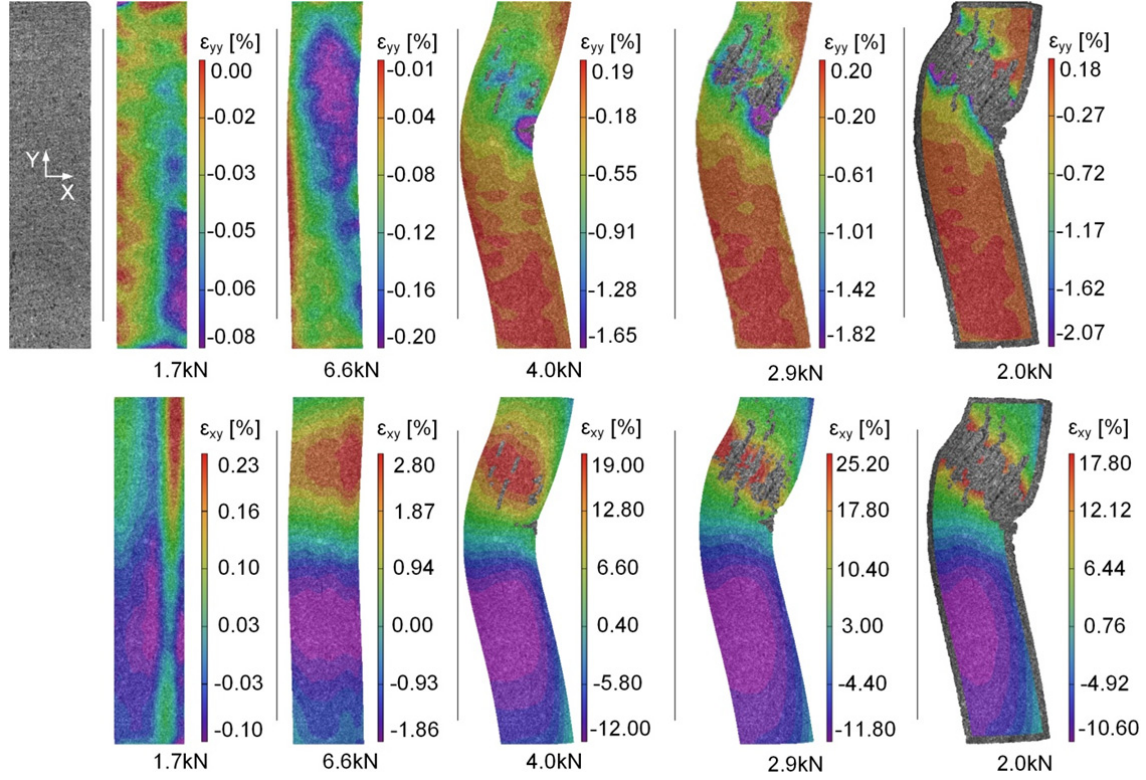

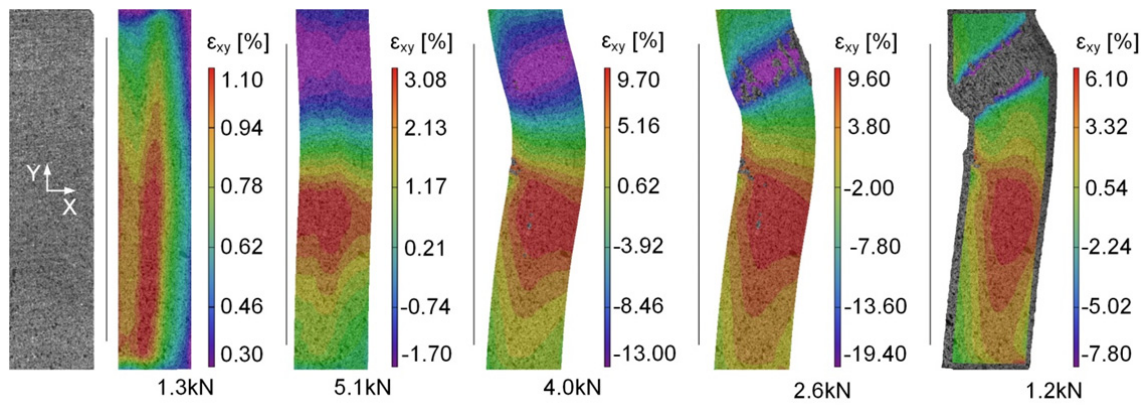**Fig. 5.12:** *Axial compressive and shear strain fields on specimen 55H105a at 105°C and different load levels*

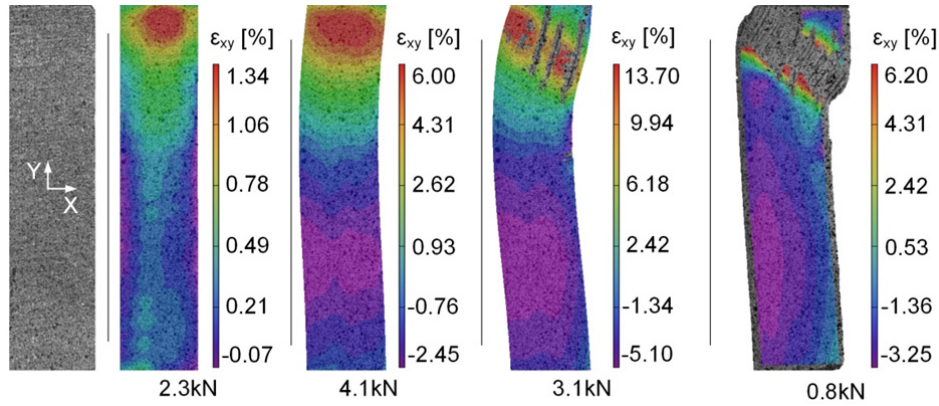**Fig. 5.13:** *Shear strain fields on specimen 55H115a at 115°C and different load levels*

85

Fig. 5.14: *Shear strain fields on specimen 55H125a at 125˚C and different load levels*

The specimen length did not influence the above-described behavior, as shown in Fig. 5.15 for the three lengths at 100°C (kinking at peak load) and 115°C (kinking at post-peak load). The compressive strain fields at the peak loads are shown at 100°C. In all cases, compressive stress concentrations appeared at the locations of the subsequent kink bands. At 115°C, the formation of the parallel grey strips in the bands of shear strain concentration occurred in all cases. Similarly, the lower fiber volume fraction did not alter the above-described behavior.
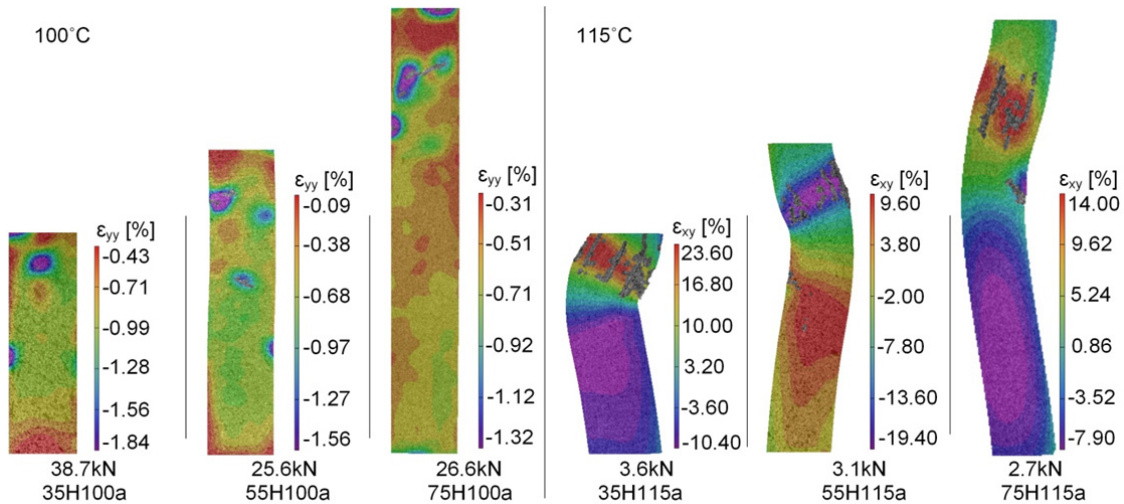

Fig. 5.15: *Compressive and shear strain field comparison of 35H, 55H and 75H series, at 100˚C and peak load and at 115˚C and load during kink band formation*

5.3.4 Lateral displacement and fiber microbuckling

In order to investigate the effect of fiber microbuckling on the failure modes, the lateral displacements (in x-direction) of five lines, drawn parallel to the specimen axis and spaced at 2mm, were extracted from the DIC measurements on 55H series specimens at 100 and 115°C, see Figs. 5.16 and 5.17.

The lateral displacements at 100 °C were extracted at five load levels: 12.3kN and 18.9kN (in the initial linear stage of the load-axial displacement curve shown in Fig. 5.6), 25.5kN (near peak load), 25.6kN (at peak load) and 7.1kN (at post-peak load), see Fig. 5.16. A slight s-shaped and parallel curvature of the five lines occurred as the load increased. Starting from 18.9kN, short waves of lateral displacements were superimposed on the basic s-shapes. The short wavelengths were between 3.07mm and 3.12mm, which were in the range of the average length of the initial fiber waviness, see Table 5.2. It was thus concluded that the appearance of the short waves at 18.9kN indicated the initiation of fiber microbuckling. The amplitudes of the short waves increased with increasing load while the wavelengths did not noticeably change. At the peak load, the wave crests at three locations, on Lines 2 and 3 at y=3mm and on Line 4 at y=18mm, became untraceable by the DIC system due to the rapid and large displacements, while the amplitudes on Lines 1 and 5 increased further. The locations of the untraceable targets corresponded well to the locations of compressive strain concentrations in Fig. 5.12. The post-peak pattern (at 7.1 kN) showed an offset of all lines at the same location at which the kink band developed. Furthermore, the fiber microbuckling was reversed at this low post-peak load.

A different behavior was observed at 115°C, see Fig. 5.17. Again five load levels were selected: 1.3kN (initial linear stage), 5.1kN (peak load), 4.0kN (end of 1st linear stage after peak load, see Fig. 5.6), 2.6kN (in 2nd linear stage after peak load) and 1.2kN (in 3rd linear stage after peak load). No lateral displacements were visible at the initial stage. At the peak load, specimen buckling was clearly visible with a maximum lateral displacement of 0.65mm. The lateral displacement then significantly increased in the first linear post-peak stage and the first targets were lost on Lines 1 and 5. However, fiber microbuckling was not visible due to the much larger scale of the x-axis compared to that of Fig. 5.17. In the second linear stage after the peak load, where the load significantly dropped, the targets on all lines became untraceable at the location of the subsequent kink band. At the third linear stage the offset of the lines coincided with the location of the kink band, see Fig. 5.13.

A quantitative comparison of the amplitude development of the wave crests of the five lines on the two specimens at 100 and 115°C is shown in Fig. 5.18. At 100°C and just before the peak load (25.5 kN), the amplitudes increased by 0.02-0-03 mm on all lines. At the peak load, the wave crests of

Lines 2-4 became untraceable while the maximum increase on Line 1 was 0.04 mm. The total amplitudes thus approximately doubled at the peak load if the initial imperfections which were of the same order as the amplitude increases, were taken into account (see Table 5.2). At 115°C, the amplitudes started increasing at 4.1 kN, the post-peak load at which the stiffness started decreasing from the first to the second linear post-peak stage. During the second linear stage the wave crests became untraceable. The amplitude development until kink band formation was comparable to that at 100°C; however, it occurred at a much lower load.
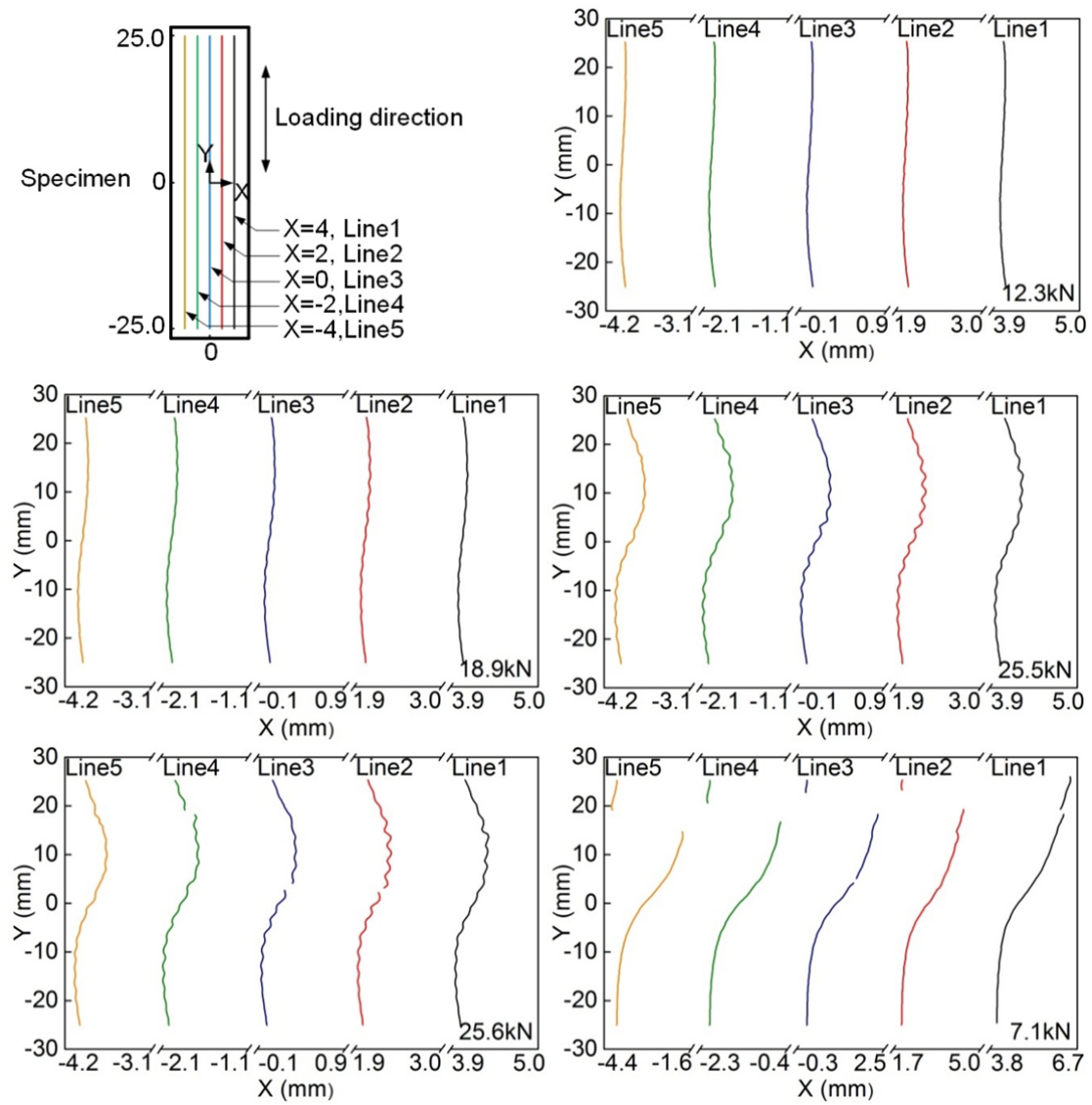

Fig. 5.16: *Displacements of Lines 1 to 5 in x-direction, along y-axis at 100°C, specimen 55H100a (note: scales for x- and y-axes are different)*
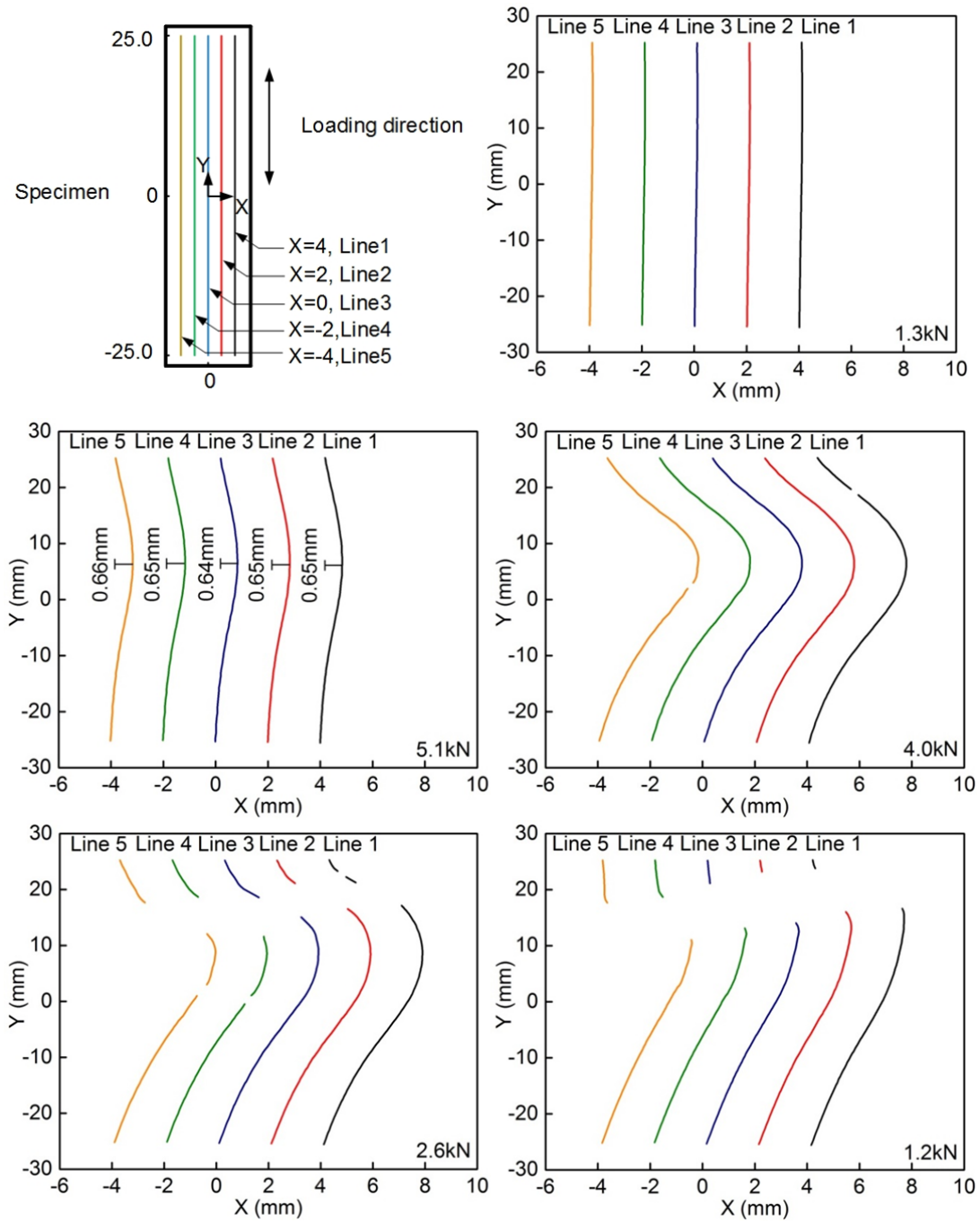
Fig. 5.17: *Displacements of Lines 1 to 5 in x-direction, along y-axis at 115°C, specimen 55H115a*
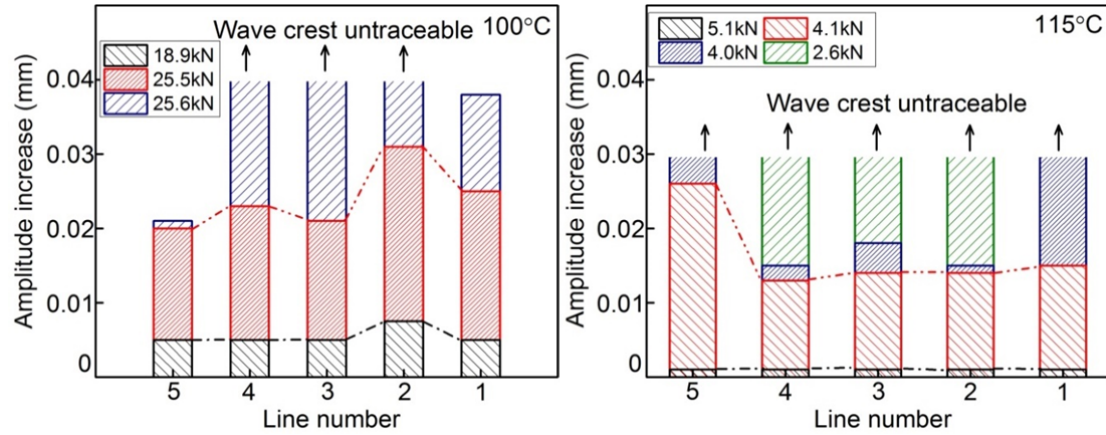
(note: scales for x- and y-axes are different)

89

Fig. 5.18: *Amplitude increases of fiber microbuckling of Lines 1 to 5 (see Figs. 5.16 and 5.17), specimens 55H100a and 55H115a at 100˚C and 115˚C*

5.4 Kink initiation mechanisms and kink band development

5.4.1 Kink initiation mechanisms

The locations where the first DIC targets were lost due to an untraceable increase of the microbuckling wave amplitudes were associated with kink initiation. At these locations, the compressive and shear strains were extracted for the 55H series specimens and compared, see Fig. 5.19. At 90 and 100°C, where kinking occurred at the peak load, the compressive strains were larger than the shear strains, almost independent of specimen length. At the higher temperatures, where the resin was in the rubbery state and kinking occurred in the post-peak phase after specimen buckling, the shear strains were predominant and much larger than the almost negligible compressive strains.

The reason for these results can be derived from Fig. 5.20. Due to the preceding buckling at the higher temperatures, lateral deformations and associated specimen bending occurred and caused maximum shear strains at the inflexion points of the buckling shapes, see Fig. 5.12, where subsequently the kink band formed. The shear strains were thus high and the compressive strains were low due to the decreasing post-peak load – in contrast to the lower temperatures where no buckling occurred (low shear strains) and kinking formed at the peak load (high compressive strains).

At lower temperatures, kinking was thus initiated locally through microbuckling under combined compressive and shear strains. At higher temperatures, shear strains were predominant and were

maximum along the grey strips, which formed parallel to the specimen axis, across the subsequent kink band width, see Fig. 5.12. These strips could be associated with an initiation of shear failures that always run parallel to the fiber direction in unidirectional laminates [28] and thus explain the subsequent debonding between the laminae.
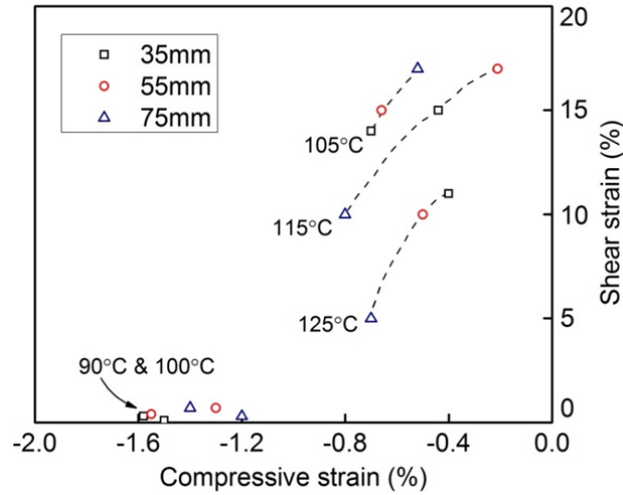

Fig. 5.19: *. Compressive and shear strains at location of kink initiation at temperatures from 90°C to 125°C*
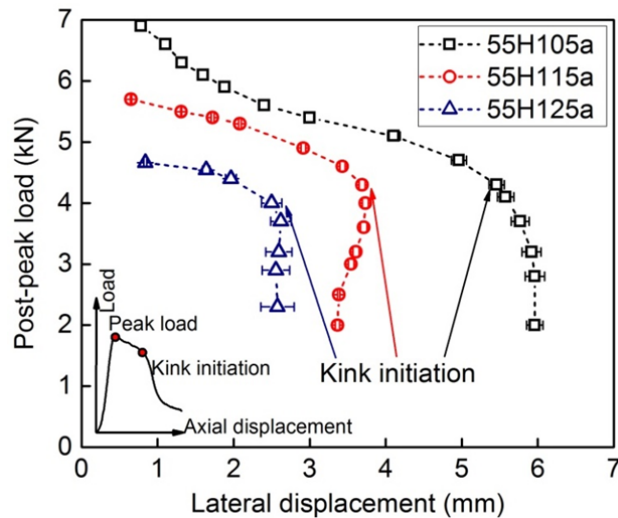

Fig. 5.20: *Increase of lateral displacements of specimens 55H105a, 55H115a, 55H125a during decrease of loads in post-peak phase (note: displacement values are averages of maximum displacements of Lines 1-5)*

The shear strains at higher temperatures depended on the temperature and specimen length, see Fig. 5.19. They were higher at 105°C but decreased up to 125°C because the lateral deformations at kink initiation were higher at 105°C than at 125°C, see Fig. 5.20. They should also have been higher for longer specimens than for shorter ones because the former were assumed to exhibit larger lateral deformations than the latter. This trend was only confirmed at 105°C however.

The increases of the amplitudes of fiber microbuckling at kink initiation as a function of temperature are shown in Fig. 5.21. The smallest amplitude increases were noted at 90°C. They increased at the glass transition state and then stabilized at the rubbery state with values which were in the range of the amplitudes of the initial waviness, as already shown above in Fig. 5.18.
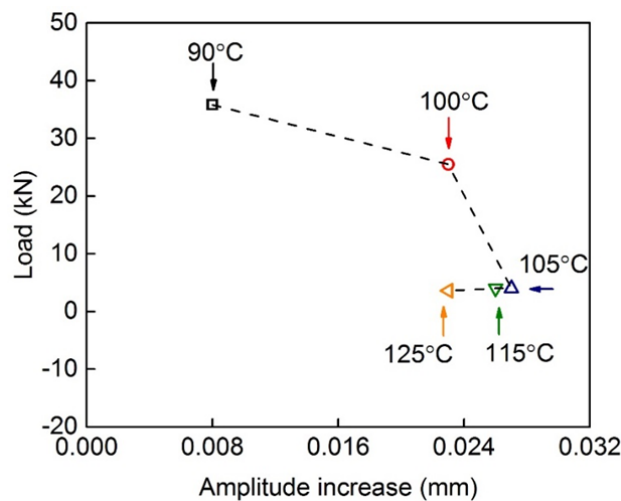

Fig. 5.21: *Amplitude increases of fiber microbuckling at kink initiation of 55H specimens at temperatures from 90°C to 125°C*

5.4.2 Kink band development

The kink band development at lower and higher temperatures was extracted stepwise from the grey areas where the DIC targets became untraceable and which were associated with the kink band, see Fig. 5.22. At lower temperatures, where kinking occurred at the peak load, the first targets became untraceable at two locations close to the peak load (at 100°C and 25.4kN, see Fig. 5.22). These spots then started extending alternately by horizontal and inclined increments up to the peak load, at which the whole band formed suddenly (visible after the sudden drop of load to 13.1 kN). The kink band width, due to the significant compressive load, remained approximately as narrow as the wavelength

of the initial imperfections. The DIC results showed that this length did not change during the increase of the amplitude. The kink band angle coincided with the angle of the inclined propagation steps mentioned above and thus mainly depended on the ratio of compressive to shear strains.

At higher temperatures, in the post-peak phase, the propagation of the small initiation spots did not occur in alternating horizontal and inclined steps, but parallel to the specimen axis. With increasing load the parallel strips propagated up to the limit of the band of maximum shear strains and their number increased with increasing lateral deformation. The thin laminae were then separated from each other by delamination and thus lost lateral stability and the kink band formed across the width of the former maximum shear strain band.

The kink band angles increased from approximately 30° to 42° as the temperature increased, as shown in Fig. 5.8. The angles in those curves, however, were related to an initially horizontal plane perpendicular to the vertical specimen axis. At higher temperatures, the specimen axis was curved due to buckling. The kink bands formed approximately perpendicularly to the curved specimen axis due to the predominant shear strains, see Figs. 5.12-5.14. Depending on the selected reference plane, it could also be argued that the kink band angle approached zero at higher temperatures.
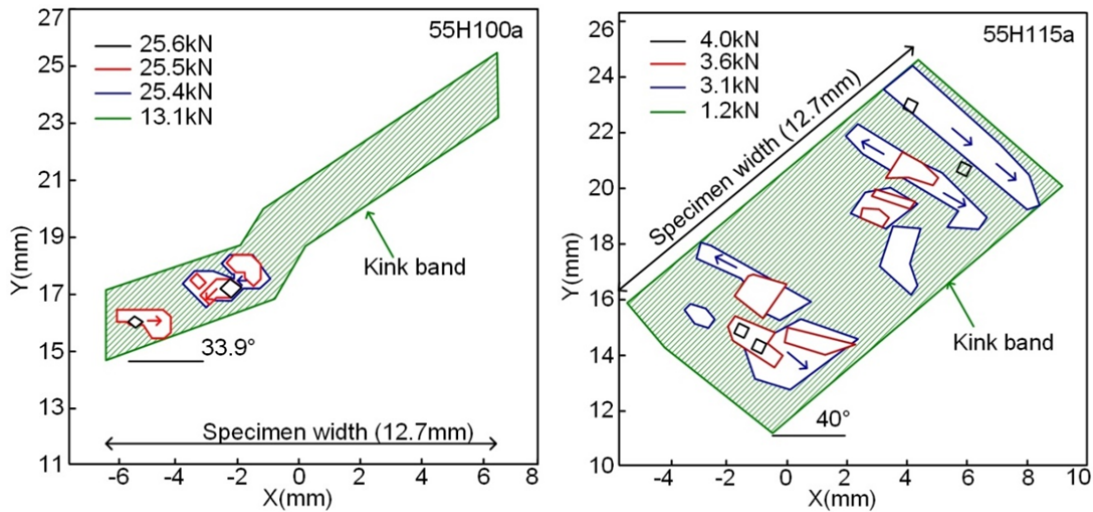

Fig. 5.22: *Kink band formation paths in specimens 55H100a and 55H115a at 100°C and 115°C*

5.5 Conclusions

The kink behavior of non-slender glass fiber-reinforced epoxy prismatic specimens of variable length and fiber volume fraction at temperatures ranging from 25°C to 125°C was investigated. The strain field development on the specimen's surface was continuously monitored by a digital image correlation device to observe the failure process and identify the failure mechanisms. The following conclusions were drawn:

1) The failure mode depended on the material state of the resin: splitting failure occurred at the glassy state, kinking failure at the glass transition and buckling with subsequent post-peak kinking at the rubbery state.

2) Kink initiation was caused by the initial imperfections, i.e. the waviness of the unidirectional fibers. Initiation at the glass transition occurred at the peak load through fiber microbuckling caused by combined compressive and shear stresses. At the rubbery state, buckling at the peak load caused high shear stresses at the locations of the inflection points of the buckling shapes. Kinking initiated in the post-peak phase at these locations again through microbuckling, but in this case caused by predominant shear and almost negligible compressive stresses.

3) Kink band formation occurred at the glass transition state through the extension of the kink initiation areas by alternating horizontal and inclined increments up to the fully developed kink band. The kink band was narrow due to the significant compressive stresses and corresponded approximately to the wavelength of the initial fiber waviness. The kink band angle depended on the ratio of compressive to shear stresses.

4) Kink band formation at the rubbery state was caused by progressive delamination between the laminae due to exceeding of the shear strength and subsequent lateral instability. The kink band was much wider than at the glass transition state and corresponded to the band width of maximum shear stresses at the inflexion points of the buckling shapes. The kink band formed almost perpendicular to the curved axis of the buckled specimens.

5) The different specimen lengths (or slendernesses) and fiber volume fractions did not influence the above-described kink initiation and kink band formation mechanisms.

References

1. Harvey, A. O. J., Analysis of 30 years of pavement temperatures using the enhanced integrated climate model (EICM), Report for the California Department of Transportation, 2004.

2. Feih, S. Mathys, Z., Gibson, A.G., and Mouritz, A.P., Modelling the tension and compression strengths of polymers laminates in fire, Composite Science and Technology, Volume 67, 2007, pp. 551-564.

3. Schultheisz, C.R., and Waas, A.M., Compressive failure of composites, Part I: testing and micromechanical theories, Progress In Aerospace Sciences, Volume 32, 1996, pp. 1-42.

4. Gutkin, R., Pinho, S.T., Robinson, P., and Curtis, P.T., A finite fracture mechanics formulation to predict fibre kinking and splitting in CFRP under combined longitudinal compression and in-plane shear, Mechanics of Materials, Volume 43, 2011, pp. 730-739.

5. Lee, S.H., and Waas, A.M., Compressive response and failure of fiber reinforced unidirectional composites, International Journal of Fracture, Volume 100, 1999, pp. 275-306.

6. Gere, J.M., and Timoshenko, S.P., Mechanics of materials, 4th edition, PWS Publishing Company, Boston, USA, 1997.

7. Rosen, B.W., Mechanics of composite strengthening, Fiber composite materials, American Society for Metals, Ohio, 1964.

8. Evans, A.G., and Adler, W.F., Kinking as a mode of structural degradation in carbon fiber composites, Acta Metallurgica, Volume 26, 1978, pp. 725-738.

9. Lankford, J., Compressive failure of fiber-reinforced composites: buckling, kinking and the role of interphase, Journal of Material Science, Volume 30, 1995, pp. 4343-4348.

10. Dobb, M.G., Johnson, D.J., and Park, C.R., Compressional behavior of carbon fibres, Journal of Materials Science, Volume 25, 1990, pp. 829-834.

11. Moran, P.M., Liu X.H., and Shih, C.F., Kink band formation and band broadening in fiber composites under compressive loading, Acta Metallurgica et Materialia, Volume 43, 1995, pp.2943-2958.

12. Volger, T.J., and Kyriakides, S. On the initiation and growth of kink bands in fiber composites: Part I. experiments, International Journal of Solids and Structures, Volume 38, 2001, pp. 2639-2651.

13. Gutkin, R., Pinho, S.T., Robinson, P. and Curtis, P.T., On the transition from shear-driven fibre compressive failure to fibre kinking in notched CFRP laminates under longitudinal compression, Composites Science and Technology, Volume 70, 2010, pp. 1223-1231.

14. Weaver, C.W., and Williams, J.G., Deformation of a carbon-epoxy composite under hydrostatic pressure, Journal of Material Science, Volume 10, 1975, pp. 1323-1333.

15. Wronski, A.S., and Parry, T.V., Compressive failure and kinking in uniaxially aligned glass-resin composite under superposed hydrostatic pressure, Journal of Material Science, Volume 17, 1982, pp. 3656-3662.

16. Grape, J.A., and Gupta, V., The effect of temperature on the strength and failure mechanisms of a woven carbon/polyimide laminate under compression, Mechanics of Materials, Volume 30, 1998, pp. 165-180.

17. Bazhenov, S.L., and Kozey, V.V., Compression fracture of unidirectional carbon fibre-reinforced plastics, Journal of Materials Science, Volume 26, 1991, pp. 6764-6776.

18. Yu, B., and Keller, T., Delamination and kink-band failure of pultruded GFRP laminates under elevated temperatures and compression, Composite Structures, Volume 93, 2011, pp. 843-849.

19. Padmanabhan, K., Time-temperature failure analysis of epoxies and unidirectional glass/epoxy composites in compression, Composites, Part A, Volume 27A, 1996, pp. 585-596.

20. Kyriakides, S, Arseculeratne, R. Perry, E.J., and Liechti, K.M., On the compressive failure of fiber reinforced composites, International Journal of Solids Structures, Volume 32, 1995, pp. 689-738.

21. Feld, N., Allix, O., Baranger, E., and Guimard, J.M., Micro-mechanical prediction of UD laminates behavior under combined compression up to failure: influence of matrix degradation, Journal of Composite Materials, Volume 45, 2011, pp.2317-2333

22. Hsiao, H.M., and Daniel, I.M., Effect of fiber waviness on stiffness and strength reduction of unidirectional composites under compressive loading, Composite Science and Technology, Volume 56, 1996, pp. 581-593.

23. Hancox, N.L., The compression strength of unidirectional carbon fibre reinforced plastics, Journal of Materials Science, Volume 10, 1975, pp. 234-242.

24. Sun, W., Vassilopoulos, A.P., Keller, T. Kink initiation and kink band formation in unidirectional glass fiber-reinforced polymers, submitted to Composites Structures on 6th. Mar. 2015.

25. Suter-Kunststoffe AG, Faserverbundwerkstoffe, Edition 2012-08, Fraubrunnen, Schweiz.

26. ASTM D695-10, Standard test method for compressive properties of rigid plastics, 2010.

27. ASTM, E1640-09, Standard test method for assignment of the glass transition temperature by dynamic mechanical analysis, 2009.

28. Bai, Y. and Keller, T., Shear failure of pultruded fiber-reinforced polymer composites under axial compression, Journal of Composites for Construction, Volume 13, 2009, pp.234-242.

6 Conclusions and future research

6.1 Conclusions

The effect of temperature on the material properties and structural response of polymer matrix composites was studied in this thesis. Analytical modeling of the molecular structure of thermosets led to the derivation of a modified G''-T equation, while the variation of storage modulus and glass transition temperature with heating rates was experimentally investigated. The compressive response of glass fiber- reinforced polymers was experimentally investigated and the kinking failure mechanisms under elevated temperatures were identified and described. A summary of the most significant results of the thesis is given below.

A new physically-based model for the simulation of the G''-T curve for thermosets is introduced in this thesis. The model is based on the modification of the G''-T equation used for thermoplastic polymers via the introduction of two new formulations regarding the calculation of the configuration probability and velocity matrix of the examined thermosets. The formulations for the calculation of the probability of configuration and velocity matrix of the polymer chain were modified according to the cross-linking structure of thermosets. In addition, an arctangent function was found to be appropriate for considering the effect of temperature on the mean square separation of the ends of the submolecules. The G''-T curve obtained from the model corresponded well with the G''-T curve experimentally derived by dynamic mechanical analysis (DMA), especially for temperatures above the glass transition. The newly introduced model is based on a sound physical background, and can be used for investigation of the effect of the molecular structure of thermosets on their G'' and T_g.

The influence of thermal lag on the glass transition temperature of polymers measured under different heating rates during dynamic mechanical analysis has been investigated. Two thermal lags were observed at heating rates higher than 0.5°C/min during the DMA scans, the first between the specimen and the Q800 DMA thermocouple, and the second along the length of the specimen. The simulation of the thermal environment inside the DMA chamber by a finite volume model demonstrated that the thermal radiation energy was an important heat source for specimen temperature elevation. The shielding of the thermal radiation by the driveshaft was the origin of the thermal lag inside the specimen. A numerical procedure was adopted to calculate the influence of the thermal gradient

97

along the length of the specimen on the storage modulus-temperature curve. It was found that when the thermal lag effects are excluded, the storage modulus of a specimen and the glass transition temperature decrease with increasing heating rates. These two results contradict the reported experimental storage modulus-temperature curves and the glass transition values obtained by disregarding the thermal lag effects

The kink behavior of non-slender glass fiber-reinforced epoxy prismatic specimens of variable length and fiber volume fraction at different temperatures was investigated. Splitting failure occurred at the glassy state while kinking failure was observed at the glass transition state and buckling with subsequent post-peak kinking at the rubbery state. Kink initiation was caused by the initial imperfections, i.e. the waviness of the unidirectional fibers.

At the glass transition, the disproportional increase of the fiber wave amplitude under combined compressive and shear stresses led to fiber microbuckling at the location of the subsequent kink initiation. The kink initiation in this case occurred before or at the peak load. At the rubbery state, kinking initiated in the post-peak phase at the locations of the inflection points of the buckling shapes through microbuckling, but in this case caused by predominant shear at these locations and almost negligible compressive stresses.

Kink band formation occurred at the glass transition state via the extension of the kink initiation areas by alternating horizontal and inclined increments up to the fully developed kink band. The kink band was narrow due to the significant compressive stresses and approximately corresponded to the wave length of the initial fiber waviness. The kink band angle depended on the ratio of compressive to shear stresses. At the rubbery state, kink band formation was caused by progressive delamination between the laminae due to the exceeding of the shear strength and subsequent lateral instability. The kink band was much wider than at the glass transition state and corresponded to the band width of maximum shear stresses at the inflexion points of the buckling shape. The kink band formed almost perpendicular to the curved axis of the buckled specimens. The different specimen slendernesses and fiber volume fractions did not influence the kink initiation and kink band formation mechanisms.

6.2 Original contribution

The original contribution of this thesis to the scientific community with regards to the experimental and analytical investigations can be summarized as follows,

Experimental investigation:

- o Experimental identification and quantification of the thermal lags observed during dynamic mechanical analysis at high heating rates for both polymers and fiber-reinforced polymers.
- o Identification of the failure modes of unidirectional glass fiber reinforced-polymers with different specimen lengths and fiber volumes at elevated temperatures.
- o Determination of the kink initiation mechanism caused by fiber microbuckling.
- o Demonstration of the variation of the kink band formation process, kink angle and kink band width with temperature.
- o Demonstration of the compressive-shear strain field at the location of kink initiation at elevated temperatures.

Analytical/numerical investigations:

- o Derivation of a physically-based G''-T equation for thermosets.
- o Introduction of a methodology for the derivation of the storage modulus-temperature curve of polymers uniformly heated at different heating rates.
- o Derivation of a finite volume model for the simulation of the thermal environment inside a DMA chamber.

6.3 Future research

Several recommendations for future investigations to further enhance understanding of the effect of temperature on polymer and FRP material properties and the structural response of FRP composites under compression are presented in the following.

6.3.1 Analytical equations for the *σ-T* relationship and the influence of entanglement

In the modified G''-T method, an arctangent function was assumed to consider the effect of temperature on the mean-square separation of the ends of sub-molecules (σ). An analytical equation between σ and temperature could be developed based on the experimental measurements of σ at elevated temperatures on materials with different cross-linking densities.

The effect of entanglement on the mechanical response was significant for polymers with long molecular chains and compact molecular structure. Although simple types of entanglement configurations have been preliminarily studied in the literature, there are not yet any models to predict the entan-

glement effect on the mechanical response of thermosets. The development of appropriate expressions for the entanglement configuration of thermosets would allow the proposed G''-T equation to model the G''-T behavior of the examined thermosets at the glassy state, where a divergence between the G''-T curve derived from the model and experiments was observed.

6.3.2 Failure envelope of kink initiation

Additional data should be collected for the development of a failure strain envelope in order to describe the kink initiation under compression at certain temperatures. For the given slenderness and temperature ranges examined in the thesis, certain combined shear and compressive strain data are available. Data concerning pure shear strain- or shear strain-dominated kink initiation in the glass transition region and pure compressive strain- or compressive strain-dominated kink initiation at the rubbery state are thus necessary to develop a complete failure strain envelope. By performing compressive experiments on slender specimens in the glass transition range, buckling will occur followed by shear strain-dominated kinking at the post-buckling stage. Similarly, to obtain compressive strain-dominated kink initiation data at the rubbery state, experiments on non-slender specimens that will fail due to kinking at peak load should be performed. With these additional data, the failure envelopes at temperatures up to the rubbery state of the examined material can be derived and appropriate models to describe the kinking failure can be developed.

6.3.3 Failure load prediction of unidirectional GFRP specimens

As described in Chapter 5, at the glass transition, the load at which kink initiation occurred can be considered as the failure load. Therefore the fibers of the FRP specimens can be modeled as Timoshenko beams with lengths equal to the wavelength of the initial fiber waviness. Equations of equilibrium including parameters representing the internal stresses and external loadings can be derived by using the principle of minimum total potential energy to obtain analytical solutions for the failure load. At the rubbery state, the same method can be applied, with the Timoshenko beam in this case representing the entire fiber along the length of the specimen and the derived load corresponding to the peak load at which buckling occurs.

In parallel to the analytical modeling, finite element models can also be developed for simulation of the deformation of FRP specimens under compression at different temperatures and the prediction of their failure.

The achievement of the objectives referred to above could lead to a failure theory for the compressive analysis of unidirectional GFRP materials and design recommendations for the use of GFRP materials exposed to elevated temperatures in civil engineering structures.

Notation

Abbreviations

FRP   fiber-reinforced polymer

CFRP   carbon fiber-reinforced polymer

GFRP   glass fiber-reinforced polymer

DMA   dynamic mechanical analysis

DIC   digital image correlation

DSC   differential scanning calorimetry

WLF   Williams-Landel-Ferry

FVM   finite volume model

Roman capital letters

A_0 coefficient matrix of V of the modified G"-T method

B mobility of the end of a sub-molecule

E'' loss modulus

$E(\beta, T)$ storage modulus at β and T

E_0 storage modulus at the initial temperature T_0

$E(T_c)$	storage modulus at T_c
$E_I(\beta,T)$	storage moduli of States *I*
$E_{II}(\beta,T)$	storage moduli of States *II*
$E_{III}(\beta,T)$	storage moduli of States *III*
E_{If}	storage modulus at the end of States *I*
E_{IIf}	storage modulus at the end of States *II*
E_{IIIf}	storage modulus at the end of States *III*
E_{Ii}	storage modulus at temperature T_{Ii}
F	measured force at the mid-span loading point
G''	imaginary parts of the complex shear modulus
I	moment of inertia
L	specimen length
M	molecular weight of the molecule of the polymer
$M_{hardener}$	molecular weight of the hardener
M_{resin}	molecular weight of the resin
N_0	number of half of the sub-molecules along the length direction of the molecular chain of thermosets
N	number of representative points of each molecule
N_A	Avogadro constant (6.02×10^{23} mol^{-1})
P	probability that the end-to-end distance of a molecule on the polymer chain is *d*
P_i	probability that the representative point (referring to the second end of the molecule) of the ith sub-molecule lies within the volume element $dx_i dy_i dz_i$ at the location x_i, y_i, z_i relative to the first end
P_N	probability of the configuration where the representative points of the *N* sub-molecules lie within the volume element $dx_1 dy_1 dz_1 \ldots dx_N dy_N dz_N$ at the relative

location $(x_i, y_i, z_i)\ldots (x_N, y_N, z_N)$

S	entropy of the molecule
S_E	energy source
T	temperature
T_0	reference temperature at the rubbery state of the thermoset
T_g	glass transition temperature
T_1	specimen temperature at Position 1
T_2	specimen temperature at Position 2
T_3	temperature measured by the Pt100 that was fastened at the same height as the Q800 thermocouple
T_c	constant temperature of sample
T_Q	temperature measured by the Q800 thermocouple
T_{Ii}	initial temperature of State I
T_{If}	temperatures at the end of States I
T_{IIf}	temperatures at the end of States II
T_{Ii}	initial temperature of State I
$T_{g,onset}$	onset temperature of the glass transition
$T_{g,rubber}$	rubbery temperature
T_{ga}	temperature corresponding to the peak of $\tan\delta$
T_{gb}	average value between $T_{g,onset}$ and $T_{g,rubber}$
T_{g1}	temperatures monitored by the Pt100 thermoresistance at Position 1 when T_g was reached
T_{g2}	temperatures monitored by the Pt100 thermoresistance at Position 2 when T_g was reached

T_{g3}	temperatures monitored by the Pt100 thermoresistance at Position 3 when T_g was reached
T_1	temperature in the center of the specimen at mid-height
T_2	temperature on the surface of the specimen at mid-height
U	velocity
V	vector velocity of the representative points of polymer molecules

Roman lowercase letters

a_1	heating rate-dependent fitting parameter
a_2	heating rate-dependent fitting parameter
a_3	heating rate-dependent fitting parameter
a_4	heating rate-dependent fitting parameter
a_5	heating rate-dependent fitting parameter
a_6	heating rate-dependent fitting parameter
b	molecular structure constant
d	end-to-end distance of a molecule
d_{mod}	displacement resulting from Eq. (3.2) and Eqs. (3.10-3.12)
d_{exp}	experimental displacement
h	enthalpy
i	i^{th} representative point
I	moment of inertia
k	Boltzmann constant (1.38×10^{-23} m$^2 \cdot$kg$\cdot$s$^{-2} \cdot$K^{-1})
n	number of molecules per volume of thermosets

p	p^{th} eigenvalue
q	a constant
s_I	fitting parameter for States I
s_{II}	fitting parameter for States II
s_{III}	fitting parameter for States III
s_i^{β}	s at State i, with $i=I, II, III$, under any desired heating rate, β
t	time
x_i	displacement of the ith representative point

Greek lowercase letters

ρ	density
τ	stress during the air-flow
β	heating rate
ε_{yy}	compressive strain fields along the y-axis obtained from DIC
ε_{xy}	shear strain field in the x-y plane obtained from DIC
η_T	steady-flow viscosity of thermosets
θ	angle between the end-to-end direction of adjunct polymer sub-molecules
λ_{1p}, λ_{2p}	eigenvalues of the coefficient matrix of the velocity of the modified G''-T method
v	Poisson's ratio
ρ_0	density of the material
σ	root of the mean square separation of the ends of sub-molecules

τ_p relaxation time of the molecule

ω load frequency

Appendix

Compression results for 35mm, 55mm and 75mm GFRP specimens

35H series
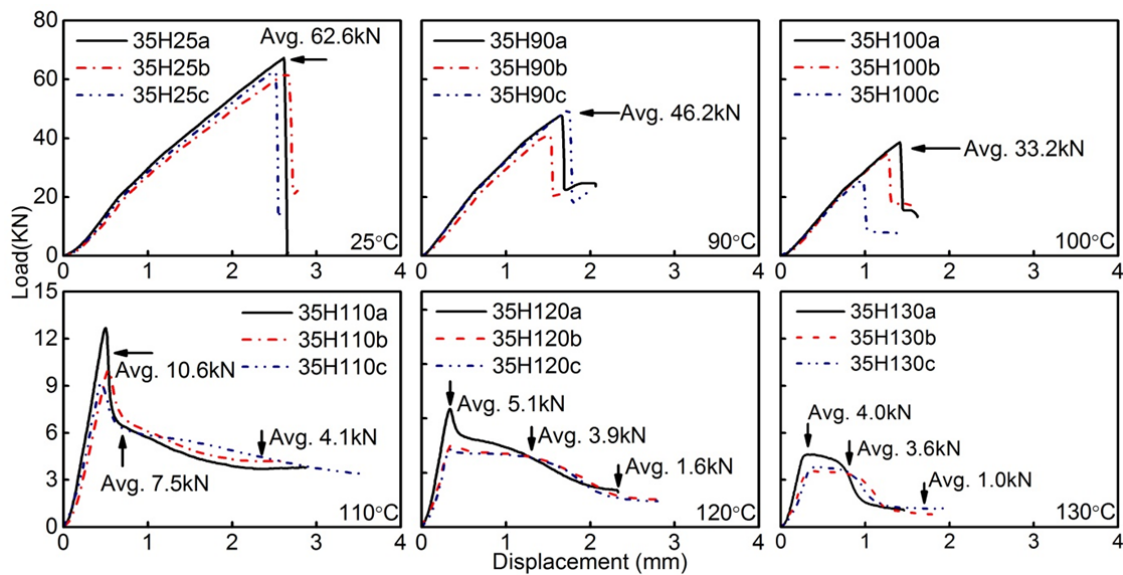
Fig. A.1: *Load-axial displacement curves of 35H series specimens with increasing temperature*
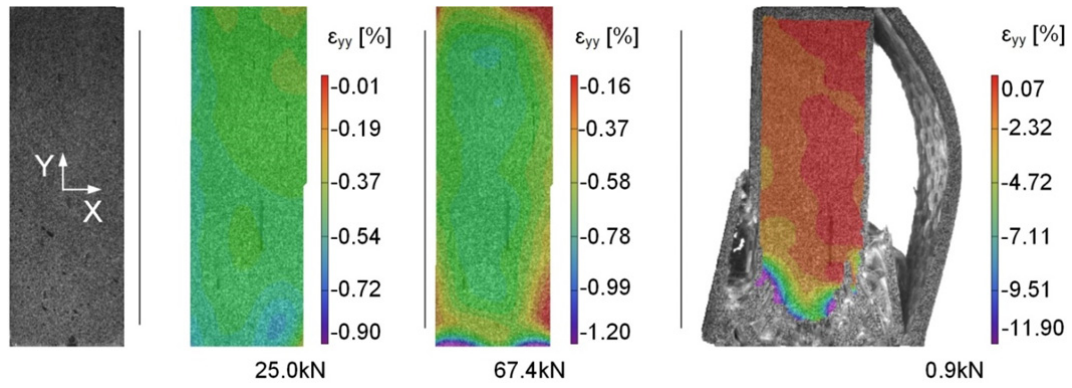
Fig. A.2: *Axial compressive strain fields on specimen 35H025a at 25˚C and different load level*
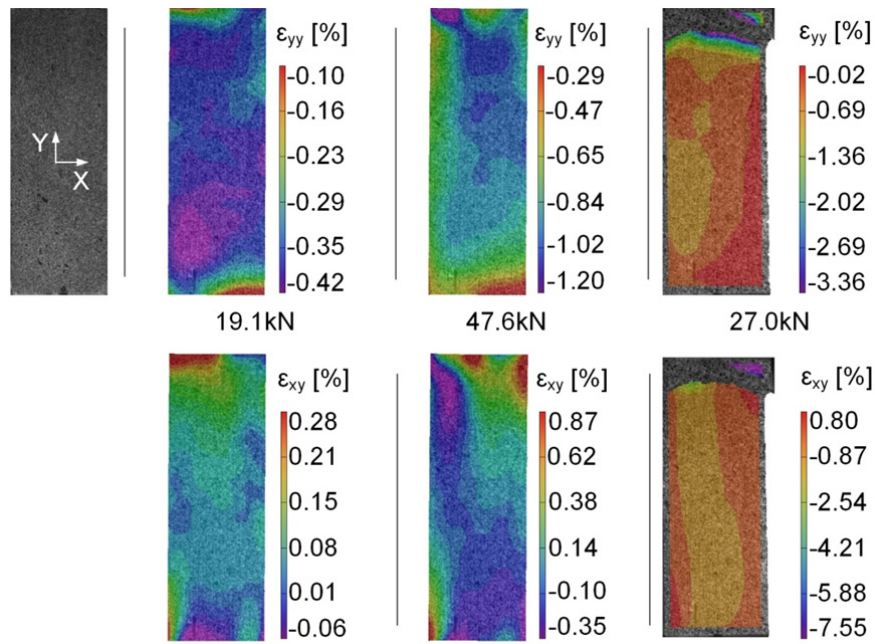
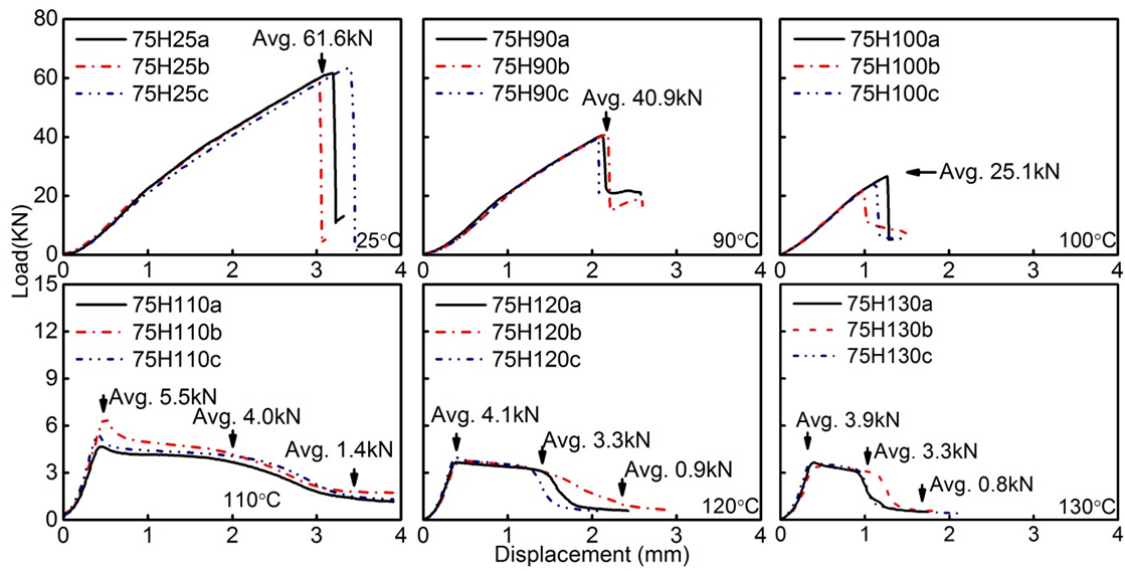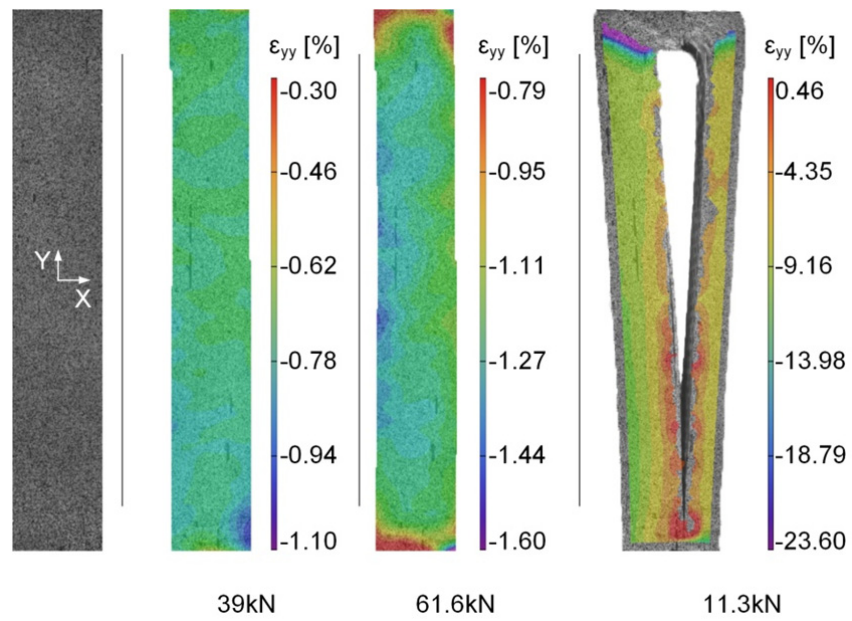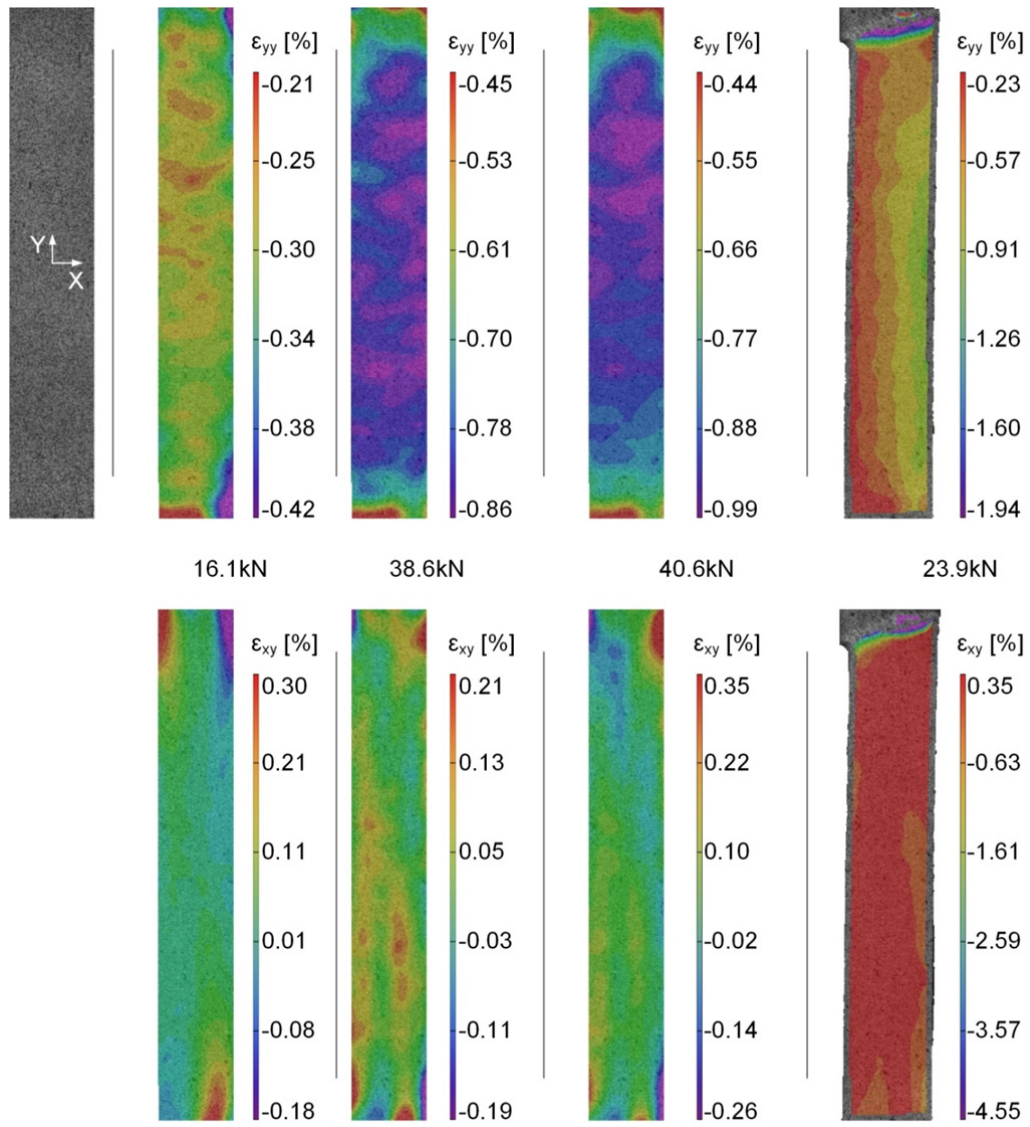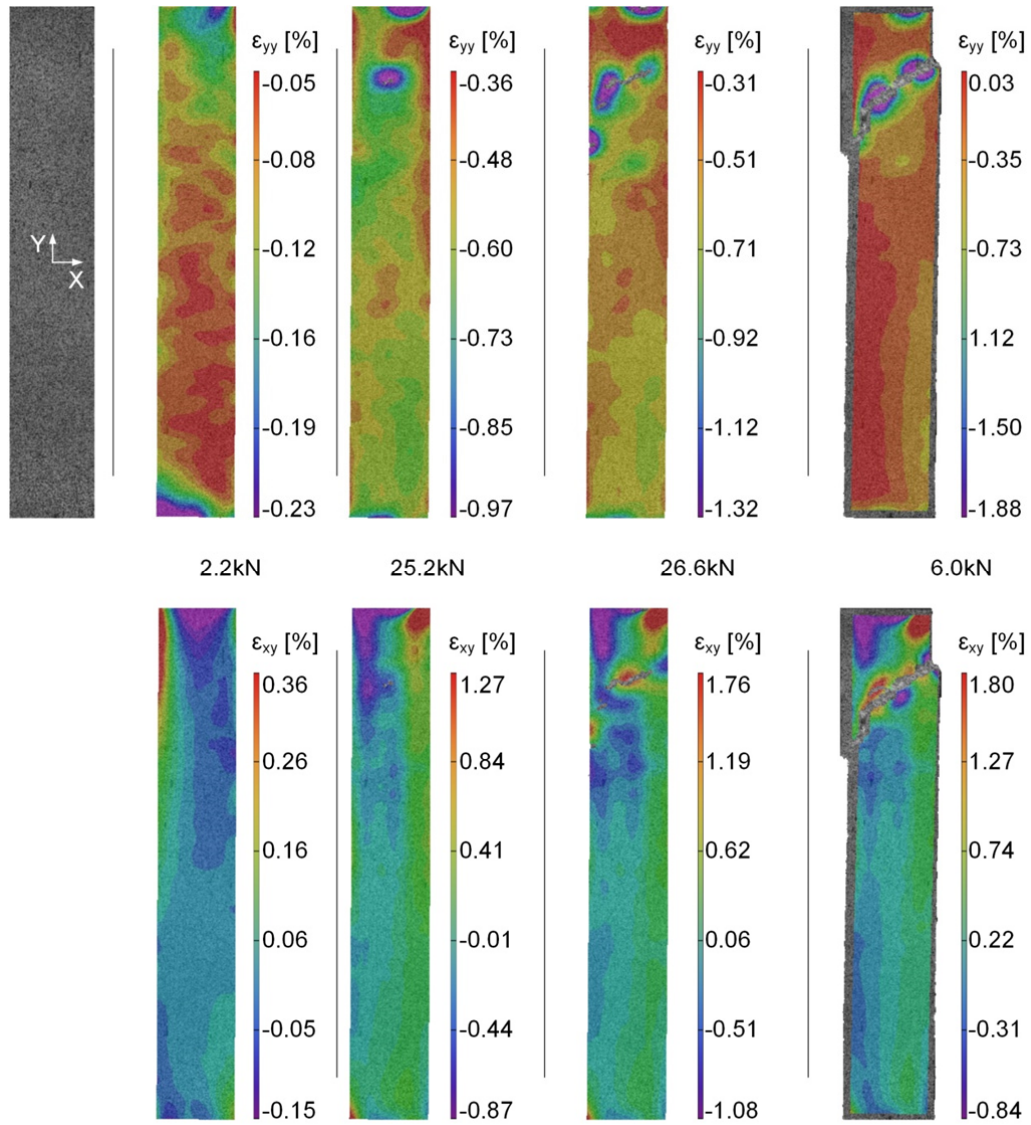*Fig. A.3:* *Axial compressive and shear strain fields on specimen 35H090a at 90˚C and different load levels*
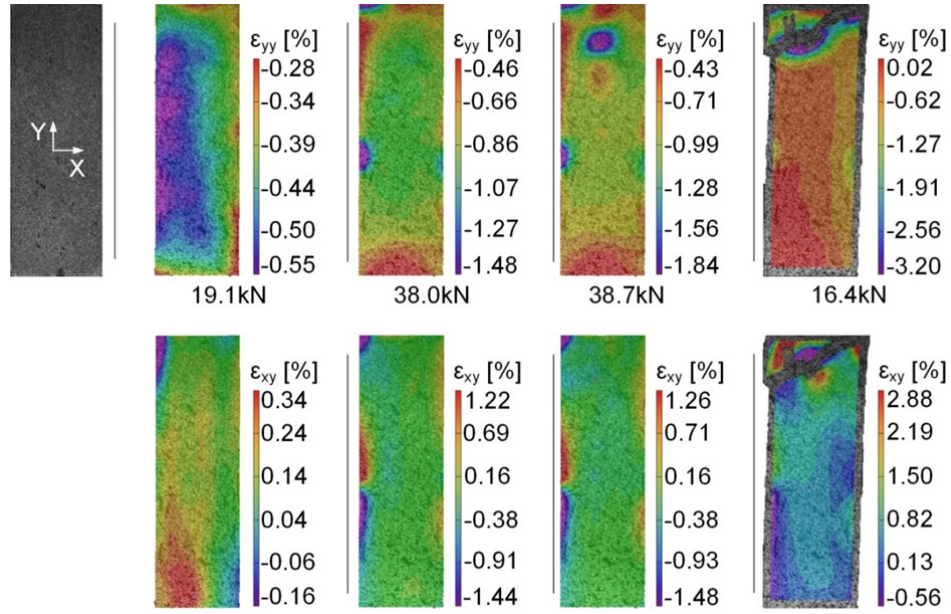
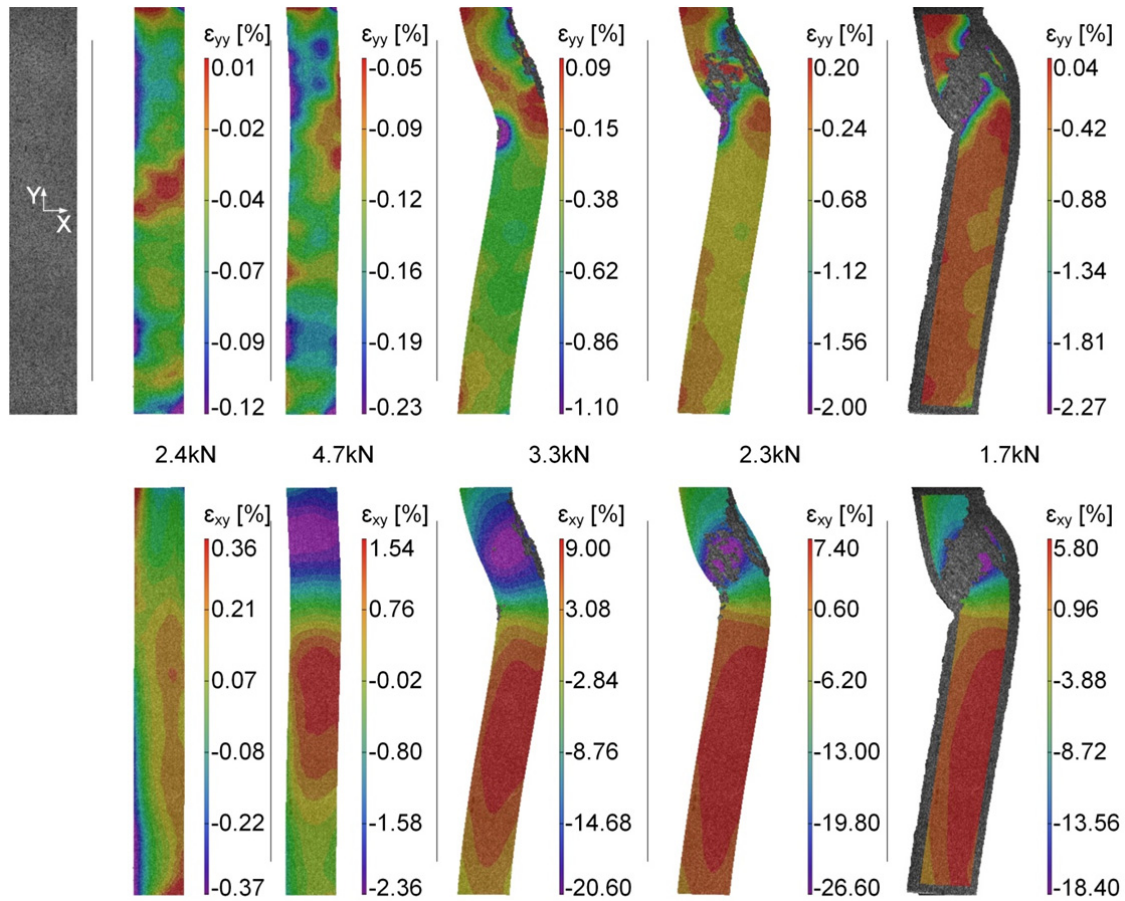***Fig. A.4:*** *Axial compressive and shear strain fields on specimen 35H100a at 100˚C and different load levels*
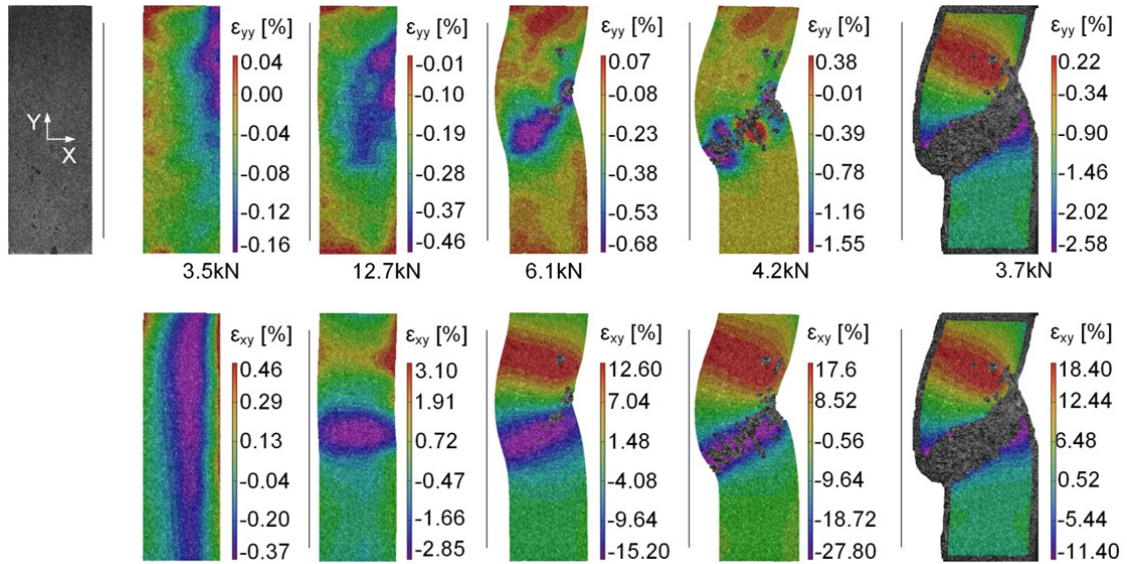
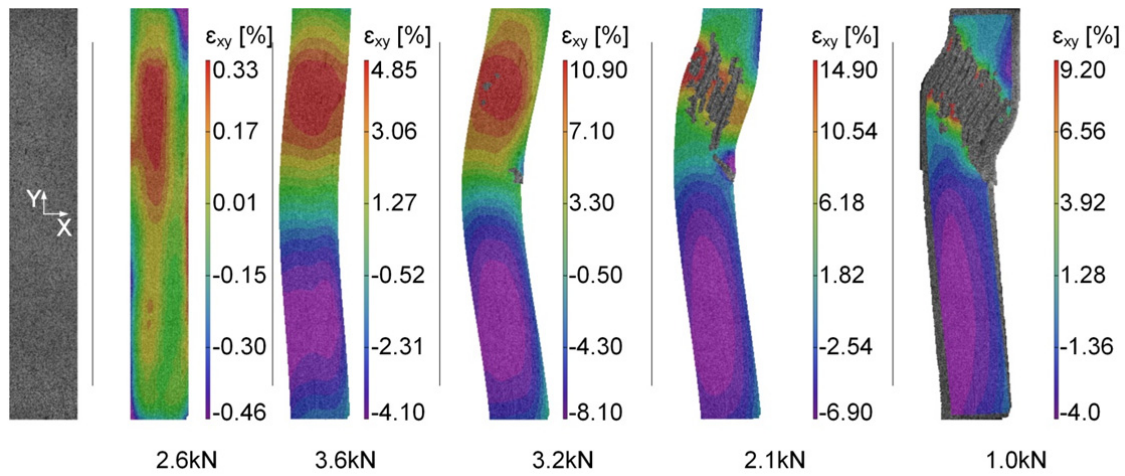***Fig. A.5:*** *Axial compressive and shear strain fields on specimen 35H105a at 105˚C and different load levels*

111
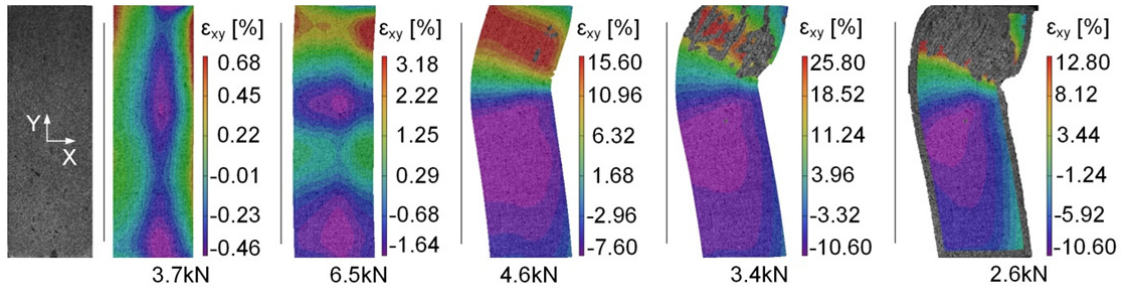
Fig. A.6: *Shear strain fields on specimen 35H115a at 115˚C and different load levels*
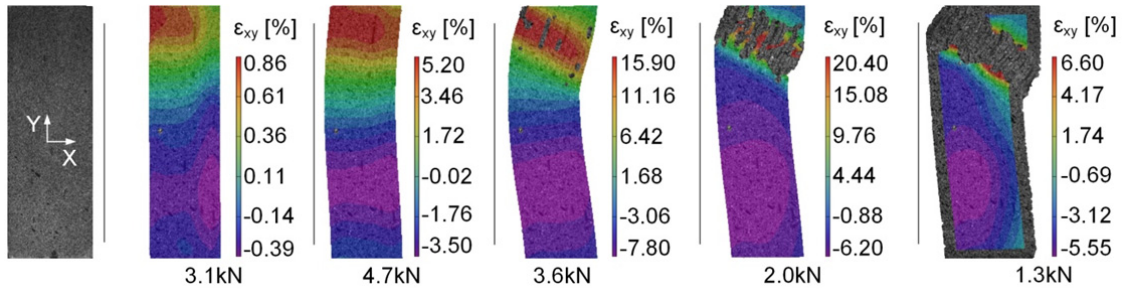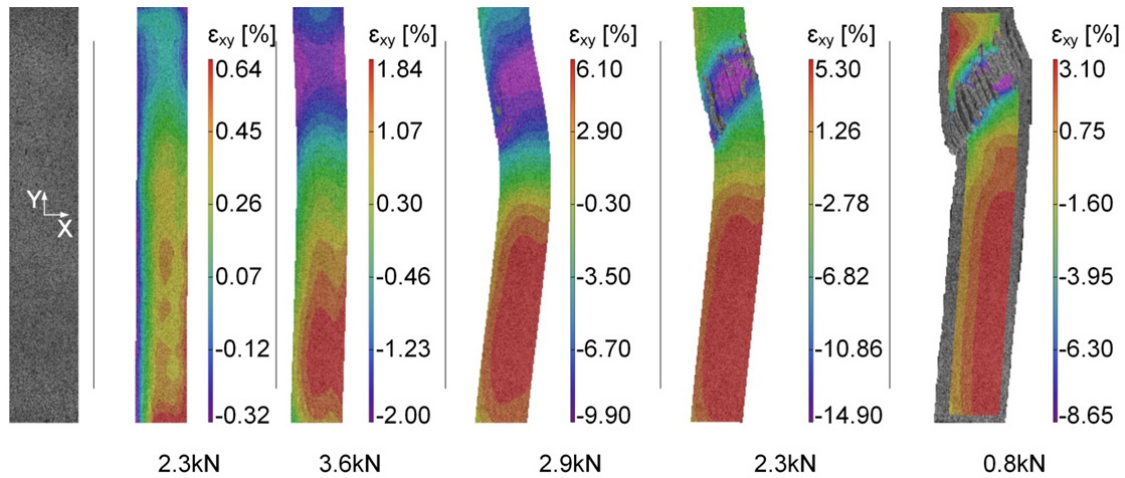

Fig. A.7: *Shear strain fields on specimen 35H125a at 125˚C and different load levels*

Fig. A.8: _Failure modes of 35H series at temperatures up to 125˚C_

55H series

Fig. A.9: *Failure modes of 55H series at temperatures up to 125˚C*
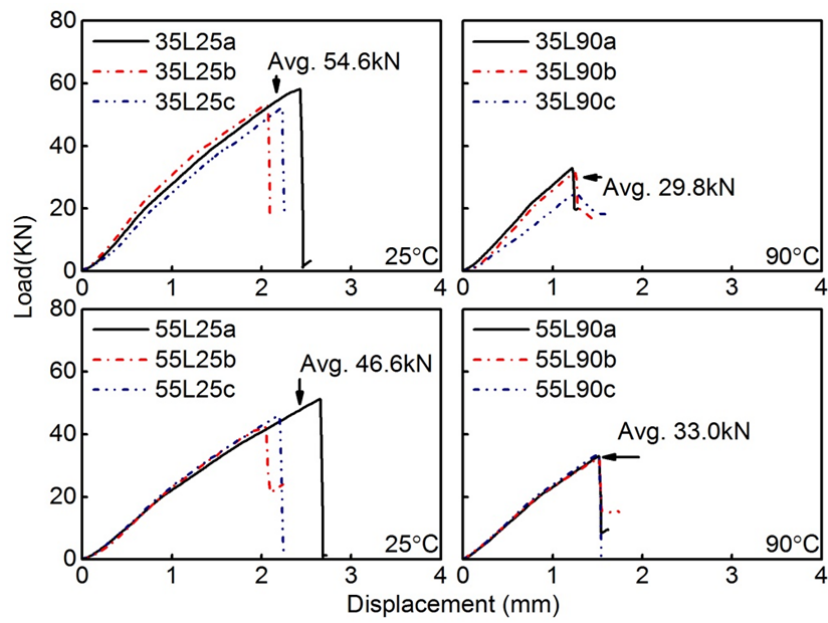
75H series

Fig. A.10: *Load-axial displacement curves of 75H series specimens with increasing temperature*

Fig. A.11: *Axial compressive strain fields on specimen 75H025a at 25˚C and different load levels*

Fig. A.12: *Axial compressive and shear strain fields on specimen 75H090a at 90˚C and different load levels*

Fig. A.13: Axial compressive and shear strain fields on specimen 75H100a at 100˚C and different load levels

Fig. A.14: *Axial compressive and shear strain fields on specimen 75H105a at 105˚C and different load levels*

Fig. A.15: *Shear strain fields on specimen 75H115a at 115°C and different load levels*

Fig. A.16: *Shear strain fields on specimen 75H125a at 125°C and different load levels*

Fig. A.17: *Failure modes of 75H series at temperatures up to 125˚C*

35L and 55L series

Fig. A.18: *Load-axial displacement curves of 35L and 55L series specimens with increasing temperature*
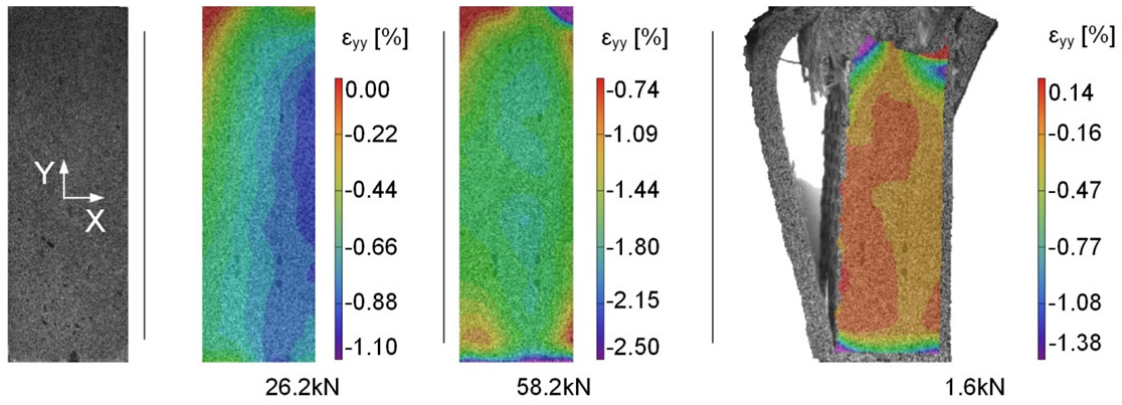
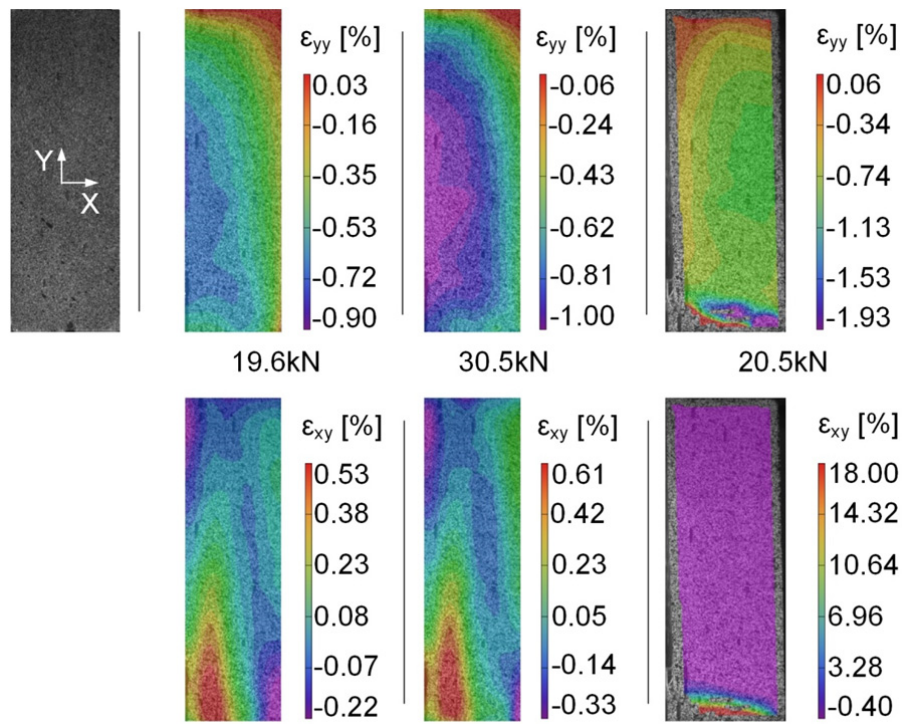**Fig. A.19:** *Axial compressive strain fields on specimen 35L025a at 25°C and different load levels*

Fig. A.20: *Axial compressive and shear strain fields on specimen 35L090a at 90°C and different*
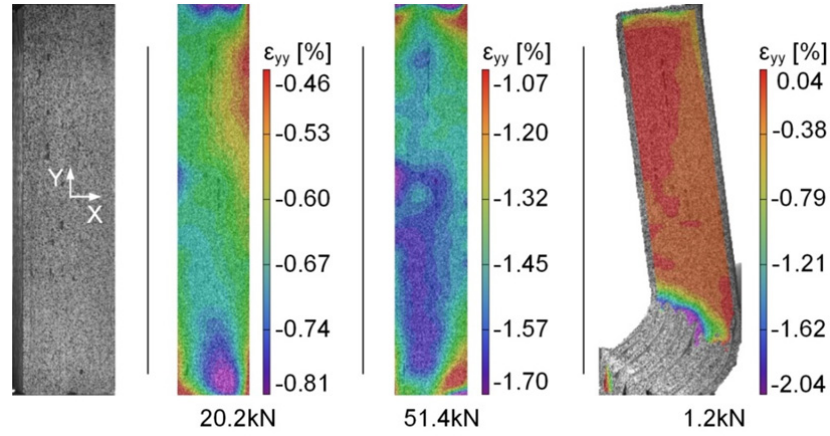*load levels*

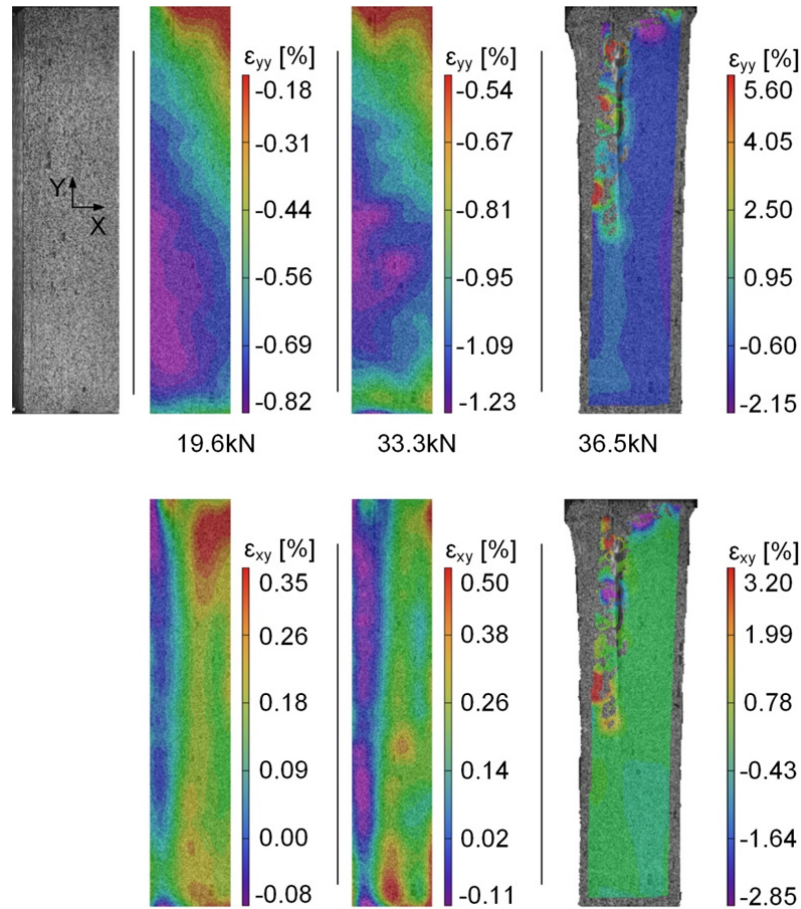**Fig. A.21:** *Axial compressive strain fields on specimen 55L025a at 25°C and different load levels*

Fig. A.22: *Axial compressive and shear strain fields on specimen 55L090a at 90°C and different load levels*
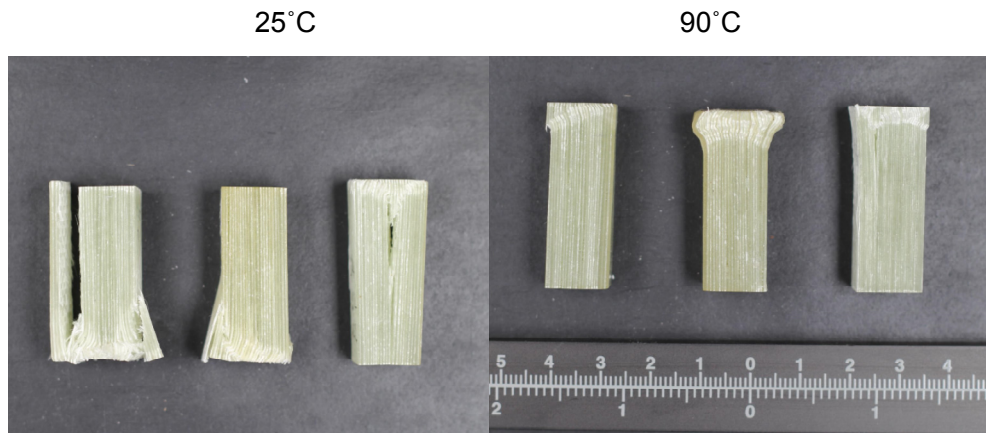
25°C   90°C

Fig. A.23: *Failure modes of 35L series at temperatures up to 90°C*

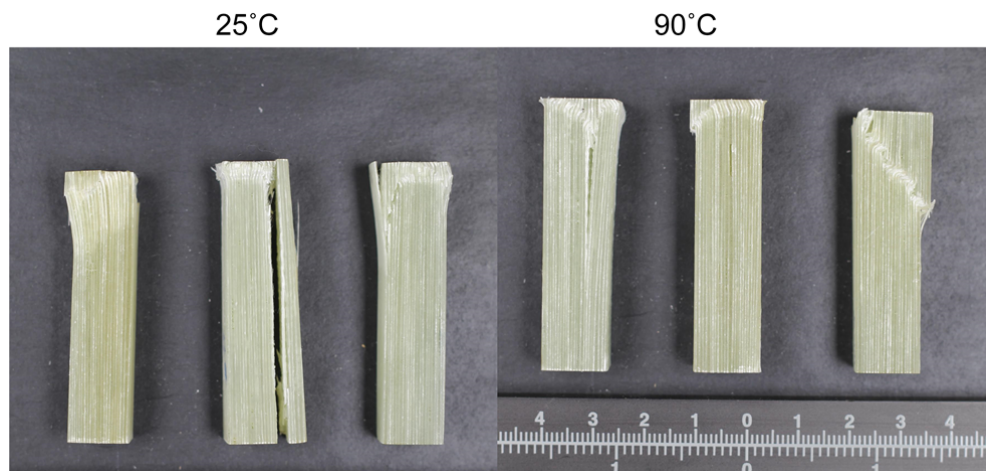25°C   90°C

Fig. A.24: *Failure modes of 55L series at temperatures up to 90°C*

WEI SUN

---Civil & Composite Engineering---

✉ wei.sun@epfl.ch   ☎ 0041789125825   ♏ 20/11/1986   🏠 Chemin de la Cocarde, 13, 1024,

EDUCATION

EPFL / Ph.D

2010-present   **Advisor: Prof. Thomas Keller**

Composite construction Laboratory
École Polytechnique Fédérale de Lausanne
(Lausanne, Switzerland)

Tsinghua Univ. / Master

2007-2010   **Advisor: Prof. Yongjiu Shi**

Department of Civil Engineering, Tsinghua
University   (Beijing, P.R. China)

Fuzhou Univ. / Bachelor

2003-2007   Department of Civil Engineering, Fuzhou
University (Fuzhou, P.R. China)

RESEARCH EXPERIENCES

Thermal mechanical property

2010-present   of GFRP under elevated and high temperatures
Research and teaching assistant

Theoretical analysis of glass transition temperature (T_g)
Effect of heating rates on T_g
Failures modes of GFRP under elevated and high temperatures
FE simulation of failure modes of GFRP

Mechanical analysis on glass curtain wall

2007-2010   **Research and design assistant**

Structural design of an industrial factory in Sichuan, China
and the shear walls of an residential building in Beijing, China

Patent: An insulation fixture for thermal experiments on
large glass plates.

SRTP research activities

2006   energy-saving buildings in Fujian, China

COMPETENCE

COMPUTER SKILL

Ansys workbench / CFX / Fluent   ● ● ● ● ◐

Mathematica / Matlab / Auto CAD ● ● ● ● ◐

Visio / Photoshop / Illustrator   ● ● ● ◐ ◐

LANGUAGE

Chinese / English   ● ● ● ● ●

French   ● ◐ ◐ ◐ ◐

German   ● ● ◐ ◐ ◐

PAPERS

Sun W, Vassilopoulos, A.P., Keller T. Effect of thermal lag on glass transition temperature of polymers measured by DMA, International Journal of Adhesion and Adhesives, Volume 52, 2014, pp. 31-39.

Sun W, Vassilopoulos A.P., Keller T. Kink initiation and kink band formation in unidirectional glass fiber-reinforced polymers, Composite Structures, 2015, DOI:10.1016/j.compstruct.2015.04.028.

Sun W, Vassilopoulos A.P., Keller T. Physically-based modelling of G''-T relationship for thermosets, (submitted in March, 2015).

Sun, W., Vassilopoulos, A.P., and Keller T., Effect of temperature on kinking failure mode of non-slender glass fiber-reinforced polymer specimens, (submitted in April, 2015).

W. Sun, A. P. Vassilopoulos, and T. Keller. Effect of thermal lag on glass transition temperature of polymers during DMA, ACUN6-Composites and nanocomposites in civil, offshore and mining infrastructure, Melbourne, Australia, November 14-16, 2012.

Sun Wei, Shi Yongjiu, Wang Yuanqing, Luo Yi, Xu Yue. The structure capability of Energy-saving glass curtain wall. Steel Construction. 2008. Vol. 23 No.115.

SHI Yongjiu, Sun Wei, WANG Yuanqing, LUO Yi,XU Yue. Analysis on the temperature fields and thermal stresses of laminated glass unit of point-supported glass curtain wall. Building Science, Volume 26. No. 7.